

Ultrasonic Investigation of Hepatic Mechanical Properties:
Quantifying Tissue Stiffness and Deformation With
Increasing Portal Venous Pressure

by

Veronica Rotemberg

Department of Biomedical Engineering
Duke University

Date: _____

Approved:

Kathryn Nightingale, Supervisor

Lori Setton

Mark Palmeri

Thomas Witelksi

Christopher Kontos

Dissertation submitted in partial fulfillment of the requirements for the degree of
Doctor of Philosophy in the Department of Biomedical Engineering
in the Graduate School of Duke University

2013

ABSTRACT

Ultrasonic Investigation of Hepatic Mechanical Properties:
Quantifying Tissue Stiffness and Deformation With
Increasing Portal Venous Pressure

by

Veronica Rotemberg

Department of Biomedical Engineering
Duke University

Date: _____

Approved:

Kathryn Nightingale, Supervisor

Lori Setton

Mark Palmeri

Thomas Witelski

Christopher Kontos

An abstract of a dissertation submitted in partial fulfillment of the requirements for
the degree of Doctor of Philosophy in the Department of Biomedical Engineering
in the Graduate School of Duke University

2013

Copyright © 2013 by Veronica Rotemberg
All rights reserved

Abstract

In this work, I investigate the mechanical response of the liver to increasing pressure in the portal vein using ultrasonic approaches. In advancing liver disease, portal venous pressure increases lead to severe clinical problems and death. Monitoring these pressure increases can predict patient outcomes and guide treatment. Current methods for measurement of portal venous pressure are invasive, expensive, and therefore are rarely repeated. Ultrasonic methods show promise because they are noninvasive, but traditional ultrasound images and doppler measurements do not yield accurate repeatable measures of hepatic pressure. However, increases in portal venous pressure have been associated with higher estimates of liver stiffness using ultrasound-based shear wave speed estimation algorithms. These quantitative estimates of shear wave speed may provide a mechanism for noninvasive hepatic pressure characterization, but they cannot currently be distinguished from the increases in shear wave speed estimates that are also observed in patients with normal portal venous pressures with advancing liver diseases. Thus, a better understanding of the mechanisms by which hepatic pressure modulates estimates of liver stiffness could provide information needed to distinguish increasing hepatic pressure from advancing fibrosis stage. This work is devoted to identifying and characterizing the underlying mechanism behind the observed increases in hepatic shear wave speed with pressurization.

Two experiments were designed in order to define the mechanical properties of liver tissue that underlie the observed increase in shear wave speeds with increasing

portal venous pressure. First, the behavior of the liver was shown to be nonlinear (or strain-dependent) by comparing stiffness estimates in livers that were free to expand and constrained from expansion at increasing hepatic pressures. Shear wave speeds were observed to increase only in the unconstrained case in which the liver was observed to qualitatively deform. Second, the deformation of the liver was quantified using a clinical scanner and 3-D transducer to generate estimates of axial strain during pressurization. Axial strain was found to increase with elevation in portal venous pressure. This axial expansion of the liver also corresponded to increases in shear wave speed estimates with portal venous pressure.

The techniques developed herein were used to elucidate mechanical properties of the pressurized liver by concurrent ultrasound-based quantification of hepatic deformation and stiffness. This work shows that increasing shear wave speed estimates with hepatic pressurization are associated with increases in hepatic axial strain measurements. These results provide the basis for quantifying the relationship between pressurization and hepatic strain, laying the foundation for hyperelastic material modeling of the liver. Such nonlinear mechanical models can provide the basis for noninvasive characterization of hepatic pressure using stiffness metrics in the future.

I would like to dedicate this dissertation to my family.

Contents

Abstract	iv
List of Tables	x
List of Figures	xii
List of Abbreviations and Symbols	xxi
Acknowledgements	xxiv
1 Introduction	1
1.1 Clinical importance of portal venous pressure	1
1.2 Current methods for the measurement of portal venous pressure	2
1.3 Use of stiffness metrics to evaluate hepatic venous pressure	4
1.4 Theoretical factors that influence shear wave speed metrics	6
1.5 Investigation of hepatic nonlinearity	7
2 Background	8
2.1 Ultrasound Imaging	8
2.2 Acoustic Radiation Force	10
2.3 Ultrasonic Displacement Tracking	11
2.4 Acoustic Radiation Force Impulse (ARFI)-based imaging	13
3 The Impact of Hepatic Pressurization on Liver Shear Wave Speed Estimates in Constrained vs. Unconstrained Conditions	20
3.1 Abstract	20

3.2	Introduction	21
3.3	Background	23
3.4	Methods	25
3.4.1	Experimental Setup	25
3.4.2	SWS Estimation Methods	26
3.4.3	Statistical Analysis	29
3.5	Results	29
3.5.1	Constrained and Unconstrained Comparison	29
3.6	Discussion	31
3.7	Conclusions	35
4	Developing and Validating Methods for Tracking Liver Deformation	37
4.1	Motivation and Background	37
4.2	Methods	39
4.3	Results and Discussion	42
4.4	Conclusions	47
5	Establishing methods used to calculate hepatic strain	48
5.1	Motivation and Background	48
5.2	Methods	51
5.3	Results and Discussion	54
5.4	Conclusions	67
6	Ultrasonic characterization of the nonlinear properties of canine livers by measuring shear wave speed and axial strain with increasing portal venous pressure	70
6.1	Abstract	70
6.2	Introduction	71

6.3	Background	72
6.4	Methods	73
6.5	Results	76
6.6	Discussion	81
6.7	Conclusions	84
7	Conclusions	86
7.1	Future work	87
A	Nonlinear Material Modeling Example	90
	Bibliography	99
	Biography	118

List of Tables

3.1	Radiation Force Sequence Parameters	28
3.2	Linear regression comparing SWS and pressure for constrained and unconstrained conditions across six experiments. The non-zero slope, high R^2 value, and low p – value of the SWS compared with pressure in the unconstrained case indicate a significant correlation between SWS and pressure when the pressurized liver is free to deform. In the constrained case, the high p – value and low R^2 value indicate that there was no correlation between SWS and pressure increase observed when the liver is not free to deform while pressurized.	33
4.1	Parameters Used for Displacement Tracking	39
4.2	Comparison between axial displacement estimation jitter in hepatic volume comparisons without motion and those with a constant inter-volume displacement.	46
4.3	Three dimensional displacement estimation jitter calculated for constant velocity translation stage motion.	47
5.1	LS-DYNA TM parameters for simulation of tissue compression.	51
5.2	Comparison of Simulation and Experimental Parameters	53
5.3	Axial strain estimates (quoted in %) based on averaging finite element strain estimates, linear regression to the assigned scatterer positions, and linear regression to the axial displacements using 3-D cross correlation methods on simulated tracked data. Average and standard deviation of 8 speckle realizations are given for the scatterer and displacement estimate results. For the simulated LS-DYNA TM output, the average and standard deviation of the region of interest is shown.	63

5.4	Lateral strain estimates (quoted in %) based on averaging finite element strain estimates, linear regression to the scatterer displacements, and linear regression to the ultrasound-based displacement estimates generated with 3-D cross correlation methods on simulated tracked data. Average and standard deviation of 8 speckle realizations are given for the scatterer and displacement estimate results. The LS-DYNA TM errors quoted are based on average and standard deviation in the region interrogated with the simulated ultrasound beams. . . .	64
5.5	Elevational strain estimates (quoted in %) based on averaging finite element strain estimates, linear regression to the assigned scatterer positions, and linear regression to the elevational displacements using 3-D cross correlation methods on simulated tracked data. Average and standard deviation of 8 speckle realizations are given for the scatterer and displacement estimate results. The LS-DYNA TM errors quoted are based on average and standard deviation in the region interrogated with the simulated ultrasound beams.	66
6.1	Parameters used for 3-D Displacement Estimation	75

List of Figures

2.1	Flowchart of an ultrasound imaging system. The grey shaded regions on the flowchart are those modified in generating and tracking displacements caused by Acoustic Radiation Force Impulse (ARFI) excitations.	9
2.2	Diagram of a typical dimension nomenclature and distribution of an ultrasound image.	11
2.3	Examples of simulated axial displacements (as represented by the colorbars in units of μm) at 0.2 msec (left column) and 0.4 msec (right column) after the ARFI push beam in a soft ($E_y = 5$ kPa, top row) and stiff ($E_y = 80$ kPa, bottom row) elastic solid [130]. Simulations were performed for a SIEMENS TM 14L-5 transducer focused at 5.5 mm in depth and using 7.27 MHz for push beams. Both the higher amplitude displacement in the softer material as compared with the stiffer material, and the slower propagation of the axial displacement laterally (in a transverse or shear wave) in the softer material demonstrate the potential for ARFI-based imaging to analyze tissue mechanical properties.	14

2.4	<p>Qualitative stiffness images of a 4 mm diameter stiff lesion in a tissue-mimicking phantom (Computerized Imaging Reference Systems, Norfolk Virginia) acquired by tracking along the axis of the ARFI excitation. The phantom has an acoustic attenuation of 0.7 dB/cm/MHz. Experiments were performed with a SIEMENSTM14L-5 transducer focused at 5.5 mm in depth and using 7.27 MHz for push and track beams. Displacements in subfigures a,b, and c are shown on a scale from zero to 8 microns at 0.2 msec after the ARFI excitation. The brighter areas represent greater displacements which correspond to softer materials. Subfigure a shows the results from an excitation focused at 3.5 mm axially, subfigure b shows the results from an excitation focused 5.5 mm axially, and subfigure c shows the results from an excitation focused at 7.5 mm axially. Subfigure d shows the average of the three focal zone images acquired with focal gain correction and a 0.4×0.6 mm median filter applied. Because displacement magnitude depends on a variety of factors including the ultrasound power supply, tissue attenuation, and geometric lesion effects, the displacement ratio cannot be used as a quantitative measure of stiffness. It can, however, be used as a qualitative depiction of areas that are stiffer or softer than others in the same field of view.</p>	15
2.5	<p>Diagram of shear wave propagation as generated by an acoustic radiation force impulse.</p>	17
2.6	<p>Sample experimental dataset showing displacements at various lateral positions at one axial depth, the focal depth of 5.5 mm. The tissue-mimicking phantom has a calibrated Young's Modulus of 4.5 kPa. The ARFI push occurs at lateral position = 0 mm and the displacement through time profiles as tracked ultrasonically and calculated by the Loupas estimation algorithm at various lateral locations are shown. Each colored line represents a different lateral position, and the shear wave speed can be calculated by observing the arrival time shift as the wave propagates laterally. A 1000 Hz low-pass filter has been applied to the displacements in the time dimension.</p>	18
2.7	<p>Relative RMS error for Ransac-based SWS estimation over 12 locations in each of 5 calibrated tissue-mimicking elasticity phantoms.</p>	18
3.1	<p>Diagram of the experimental setup for comparison between excised canine livers that were or were not constrained from deformation throughout pressurization. The increase in hepatic pressure was accomplished by raising the saline reservoir from the level of the portal vein as shown above.</p>	26

3.2	Two sample unconstrained experimental datasets. Average axial displacements over 4.4-5.1 cm in depth are shown at various lateral positions. The ARFI push occurs at lateral position = 0 mm and the displacement through time profiles as tracked ultrasonically and calculated by the Loupas estimation algorithm [100] are shown. A 1000 Hz low-pass filter has been applied to the displacements in the time dimension. At increased pressure, the displacement amplitudes are observed to be smaller and the displacement peaks occur earlier in time, both of which correspond to faster shear wave speed propagation and increased material stiffness.	27
3.3	The RANSAC-based iterative removal of outliers as implemented for SWS estimation [192] is shown for the two datasets examined in figure 3.2. A steeper time to peak displacement versus lateral position corresponds to a slower shear wave speed as shown for the figure on the left at 1 mmHg hepatic pressure as compared with the figure on the right at 44 mmHg pressure. Both datasets were collected in the unconstrained case for which the liver was allowed to expand with increased pressure.	29
3.4	Comparison within one ex-vivo canine liver between a pressurized case limited in volume (constrained, shown with circles) to one allowed to expand (unconstrained, shown with boxes).	30
3.5	Comparison between pressurization and SWS for constrained (shown with circles) and unconstrained (shown with boxes) cases from independent measures taken in six ex-vivo canine livers. Standard deviation between the experiments in pressure and SWS are shown as horizontal and vertical errorbars respectively. The * represent groups for which the p -value was less than 0.01.	31
3.6	Multiple linear regression results for the unconstrained (subfigure a) and constrained (subfigure b) SWS estimates across all six experimental animals. The p – values for the hypothesis that SWS does not change with pressure are 0 and .96 for the unconstrained and constrained cases respectively. More quantitative results for the linear fit are shown in table 3.2.	32

3.7	Screen images from the ultrasound scanner comparing constrained and unconstrained canine livers at 45 mmHg. The green boxes shown above represent the region of interest interrogated using shear wave speed metrics for each case. As shown, the depth of the radiation force excitation varied from 3.5 cm to 5.1 cm in depth from the transducer face. Regions of interest were selected for distance from edges of the liver and relative homogeneity based on B-mode examination. Six shear wave speed datasets were acquired for each pressure at one location of radiation force excitation.	33
4.1	Three-dimensional normalized autocorrelation of speckle for the imaging parameters used.	40
4.2	Displacement estimates from 0.02-0.12 mm as a function of 7 different axial kernel sizes (different colors, shown in mm). Errorbars show the spatial standard deviation of the displacement estimate over a 2x1.1x1.1 cm volume from 5-7 cm in depth. Lateral and elevational kernel sizes were kept constant at 0.40 and 0.45 mm respectively for the data shown.	43
4.3	Two different lateral and elevational kernel sizes were tested on pure axial motion using the translation stage. A 0.9 correlation coefficient cutoff was used for the displacement estimation. A line with unity slope is shown in black. The R^2 of the displacement estimates to this unity line is 0.99 for the smaller kernel (left) and 0.99 for the larger kernel (right).	43
4.4	Two different lateral and elevational kernel sizes were tested on pure lateral motion using the translation stage. A 0.9 correlation coefficient cutoff was used for the displacement estimation. A line with unity slope is shown in black. The R^2 of the displacement estimates to this unity line is 0.88 for the smaller kernel (left) and 0.93 for the larger kernel (right).	44
4.5	Two different lateral and elevational kernel sizes were tested on pure elevational motion using the translation stage. A 0.9 correlation coefficient cutoff was used for the displacement estimation. A line with unity slope is shown in black. The R^2 of the displacement estimates to this unity line is 0.48 for the smaller kernel (left) and 0.50 for the larger kernel (right).	44

4.6	Effect of kernel size on bulk displacement estimate bias. The axes are changed between the axial plot and the lateral and elevation plots to provide information about the slight differences observed in the kernel sizes tested. Three kernel sizes were tested on pure axial, elevational, and lateral motion using the translation stage. A 0.9 correlation coefficient cutoff was used for the displacement estimation. The average bias for each displacement estimation volume across different kernel sizes is shown above. The bias for each displacement magnitude does appear to increase in magnitude in the lateral and elevational dimensions with kernel size, but the results are not statistically distinguishable from each other.	45
4.7	Effect of kernel size on displacement estimate spatial variability for bulk motion. Three kernel sizes were tested on pure axial, elevational, and lateral motion using the translation stage. A 0.9 correlation coefficient cutoff was used for the displacement estimation. The spatial variation of each displacement estimate for the corresponding translation stage motion direction is shown above and appears to decrease with increasing elevation and lateral kernel size.	46
5.1	Axial displacement calculation from finite element simulations using LS-DYNA™. The region of interest interrogated by the simulated transducer is shown in black. The gradient of displacement can clearly be seen in the top row of each image (the color limits of the images vary with different strains).	55
5.2	Axial strain calculated using LS-DYNA™ finite element simulations. The region of interest interrogated by the simulated transducer is shown in black.	56
5.3	Examples of the line fit used to generate axial strain estimates for the four deformation cases using the scatterer positions generated from LS-DYNA™ simulation output. The scatterer displacements are shown in black and the line fit is shown in red. In this case, the 95% confidence interval is given rather than a standard deviation because there is only one measurement.	57
5.4	Axial strain estimate based on linear regression of scatterer displacement versus position as compared with the average of the finite element simulation strain estimate in the region of interest. Errorbars shown which appear to be generally smaller than the marker size are the standard deviation of eight scatterer realizations (for the scatterers) or the strain estimate in the region of interest (for the simulations).	58

5.5	Example simulated and tracked axial displacement versus position using 3-D tracking for the four simulated strain cases. The calculated strain for each of the datasets are shown with intervals quoted as the 95% confidence interval of the line fit and the mean displacement is subtracted so all the displacements are centered around zero. The axes for the top row are smaller than for the bottom row in order to show all displacement estimates in the four cases. The bottom right plot shows the erroneous positive fit achieved for the largest strain case (strain expected -0.88% strain as compared to the estimate of 1.17%).	59
5.6	One axial A-line acquired from simulated deformed scatterers with imposed 0.84% compressive strain. From 0.05 to 0.052 m in depth there is no signal, which is an artifact of the simulation approach in which scatterers were populated starting at 0.05 m. This artifact may lead to bias in the strain and displacement estimates but is not expected in vivo. The addition of many scatterers closer to the transducer could reduce the effect of this error in the region of interest, but at the expense of much larger datasets and longer run times for the simulation.	60
5.7	Example axial displacement versus position using 3-D tracking as compared with the input scatterer displacement for all strains simulated. In the lower plots (that correspond to larger displacement amplitudes), there are differences observed between the displacement estimates and the change in scatterer position simulated.	61
5.8	Displacement estimate plotted with the correct scatterer displacement and the scatterer displacement shifted by $\lambda/2$ and λ . The relationship between the underlying simulated displacement (as represented by the scatterer red line) and the displacement estimate is clearly either a factor of $\lambda/2$ or of λ , a pattern which strongly suggests peak hopping behavior.	62
5.9	Lateral strain estimate based on linear regression of scatterer displacement versus position as compared with the average of the finite element simulation strain estimate in the region of interest. Errorbars shown which appear to be generally smaller than the marker size are the standard deviation of eight scatterer realizations (for the scatterers) or the strain estimate in the region of interest (for the simulations).	65

5.10	Elevational strain estimate based on linear regression of scatterer displacement versus position as compared with the average of the finite element simulation strain estimate in the region of interest. Error-bars shown which appear to be generally smaller than the marker size are the standard deviation of eight scatterer realizations (for the scatterers) or the strain estimate in the region of interest (for the simulations).	66
5.11	Example simulated and tracked lateral displacement versus position using 3-D tracking for the four simulated strain cases. The calculated strain for each of the datasets are shown with intervals quoted as the 95% confidence interval of the line fit and the mean displacement is subtracted so all the displacements are centered around zero. While the two largest strain cases (bottom row) are close to the expected result, the smallest strain estimates are the incorrect sign. Lateral displacement estimate variability increases with increasing lateral strain.	67
6.1	Diagram of the hepatic pressurization and monitoring setup	74
6.2	Example of data acquired in a pressurization increment between 17 and 18 mmHg portal venous pressure in one excised canine liver. One axial A-line through the center of the volume interrogated is shown through time after pressure increase. Expansion is observed in the growth of the brighter region, which represents the liver. The red lines represent the axial extent of the 3-D region of interest over which strain was computed.	75
6.3	Axial strain calculation was performed using linear regression between axial displacement and axial position throughout the imaging volume for each time step (14080 kernels/volume). Subplots a) and b) provide example results from similar strain states in two different livers but with very different 95% confidence intervals on the strain estimate. In the left of each subfigure, all the displacement estimates used to perform the linear regression are shown while on the right the distribution of displacement estimates at each axial position is shown. The red lines on the right side of each subfigure show the bounds of the 95% confidence interval of the linear regression. In subfigure a), the strain was 0.37% with the confidence interval of 0.03% while in subfigure b), the strain was 0.45% and the confidence interval was 0.1%.	77

6.4	Sample dataset showing displacements at various lateral positions averaged over the depth of field around the focal depth in a sample hepatic experimental dataset. The ARFI push occurs at lateral position = 0mm and the displacement through time profiles at various locations are shown. Each colored line represents a different lateral position, and the shear wave speed can be calculated by observing the arrival time shift as the wave propagates laterally. A 1000 Hz low-pass filter has been applied to the displacements in the temporal dimension.	78
6.5	Axial strain during a pressurization increment between 17 and 18 mmHg as estimated using accumulation of individual volume-to-volume strain calculations. The errorbars shown are the accumulated 95% confidence intervals on the strain estimates (calculated as described in Figure 6.3).	78
6.6	Example change in position and extent of the hepatic region interrogated for part of a pressurization step between 17 and 18 mmHg. Displacements were accumulated to demonstrate the change in the 3-D position and extent of the volume for an estimated 1.83% increase in axial strain.	79
6.7	Shear wave speed increases observed with increasing portal venous pressure across 6 excised canine livers (differentiated by color). Errorbars shown represent the standard deviation of 6 shear wave speed datasets acquired in the same location at each pressure.	79
6.8	Percent axial strain increases observed as a function of increasing portal venous pressure for 6 excised canine livers (differentiated by color). Errorbars shown represent the accumulated 95% confidence interval on the strain estimate.	80
6.9	Comparison between shear wave speed, percent axial strain, and pressure in the two livers that were not observed to expand. For clarity, axes and errorbars shown correspond to those shown for the 6 cases in which expansion was seen.	80
6.10	Shear wave speed compared with percent axial strain across 6 excised canine livers (differentiated by color) Because the six SWS estimates were in the same region of interest, the errorbars (which represent the standard deviation of the six SWS estimates) do not show potential tissue heterogeneity but rather the limits of system precision on SWS estimates.	81

A.1 Comparison between the theoretically predicted linear elastic behavior of SWS under material compression with those shear wave speeds predicted for two sets of Mooney-Rivlin material parameters. 98

List of Abbreviations and Symbols

Abbreviations

HVPG hepatic venous pressure gradient.

PVP portal venous pressure.

dDUS duplex doppler ultrasound.

cDUS color doppler ultrasound.

ARFI acoustic radiation force impulse.

ROE region of excitation.

DOF depth of field.

SWS shear wave speed.

SWEI shear wave elasticity imaging.

TOF time-of-flight.

MR Mooney-Rivlin.

NH Neo-Hookean.

PBS phosphate buffered saline.

IQ in-phase and quadrature.

ROI region of interest.

I_{sppa} spatial peak-pulse average intensity of an ultrasound pulse.

MI mechanical index of ultrasound pulse.

ANOVA analysis of variance.

Symbols

c_o speed of sound.

ρ_o material density.

Z acoustic impedance.

\mathbf{F} radiation force.

I temporal average acoustic intensity.

α acoustic amplitude attenuation coefficient.

λ_u ultrasound wavelength.

f_c center frequency of ultrasound pulse.

T kernel size.

BW fractional bandwidth of ultrasound transducer.

ρ correlation between reference and tracked RF-data.

F F/# of focal configuration ($F = \frac{z}{D}$).

z focal depth.

D aperture size.

c acoustic or compressional wave speed.

c_T shear (or transverse) wave speed.

σ_S strain estimate variance.

σ_{ij} cauchy stress.

W strain energy function.

ϵ_{ij} finite strain tensor.

C_1 fundamental material constant for MR and NH hyperelastic material models.

C_2 fundamental material constant for MR hyperelastic material models.

\mathbf{C} right Cauchy-Green deformation tensor.

I_1 first invariant of \mathbf{C} , $I_1 = Tr[\mathbf{C}]$.

I_2 second invariant of \mathbf{C} , $I_2 = \frac{1}{2}(Tr[\mathbf{C}]^2 + Tr[\mathbf{C}^2])$.

u_1 particle displacement due to acoustic radiation force.

X_i reference configuration.

x_i deformed configuration.

F deformation gradient.

μ material constant corresponding to shear modulus under assumptions of linear elastic isotropic elasticity.

λ stretch, corresponds to $\lambda_i = 1 + \epsilon_{ii}$.

Acknowledgements

I have many so people to thank for their support during graduate school. I am especially grateful to Kathy and Mark for their enthusiastic recruitment and encouragement while here. My years at Duke have been all that I had hoped due to their influence and I've learned an incredible amount from them. I would also like to thank my other committee members, Lori Setton, Thomas Witelski, and Christopher Kontos. I've relied on all of their expertise in working toward this dissertation and I am honored that they agreed to play such an important role in this work and in my career.

I am very appreciative of the role that Drs. Anna Mae Diehl, Manal Abdelmalek, and Andrew Berchuck have played in my training. As I look forward to my return to medical school, I feel very lucky that these physician scientists have been so free with their time and am so looking forward to working with them more as I continue in the Medical Scientist Training Program here at Duke.

Studying ultrasound at Duke is a wonderful experience because there are so many mentors and students to rely on for advice, new information, technical expertise, and other help. I especially want to thank Dr. Patrick Wolf and Ellen Dixon-Tulloch for their patience and assistance with the animal studies in this work. My officemates David Bradway, Stephen Rosenzweig, and Seung Lee have displayed admirable patience with my interruptions and have been invaluable in answering my questions and providing helpful feedback. Drs. Gregg Trahey and Jeremy Dahl have always

welcomed questions, and my general understanding of ultrasound and the scanners we use have increased immeasurably through these interactions. I've benefited extensively from working with Steve Hsu, Doug Dumont, Ned Rouze, Kristen Bing, Michael Wang, Brett Byram, and Matthew Panzer. Thank you also to the other members of the Wolf, Trahey, and Nightingale labs for their support. I have particularly enjoyed our day to day interactions, and I treasure our community.

I am so grateful for the support and encouragement I received from my parents and brother as well as my husband Ilan. They, in addition to the medical school and biomedical engineering community at Duke have contributed greatly to my well-being during graduate school. Thanks especially to Jessica, Matt, Nicole, David, Laura, Nicky, and Devin who were always up for adventures and distractions!

There are several professors, teachers, and mentors who helped me on my way to graduate school and continue to inspire me. I still think often about Denise Labieniec and her enthusiasm for physics, as well as Professors Howard Georgi, David Edwards, and Russ Altman, who remain influential to my research and long-term career goals.

I have been honored to receive two individual awards for funding over the course of graduate school which have greatly aided my research and training. Thank you to the Gertrude B. Elion Mentored Medical Student award and the NIH National Institute for Diabetes and Digestive and Kidney Diseases F30 DK095544.

Introduction

1.1 Clinical importance of portal venous pressure

As recently as 2001, cirrhosis and chronic liver disease lead to more than 27,000 deaths per year in the United States, comprising the 10th leading cause of death in men and the 12th leading cause of death in women in 2001 [4]. The progression of liver failure due to advancing liver fibrosis (cirrhosis) leads to increases in portal venous pressure (PVP) [20, 150, 176], which is in turn responsible for the most severe clinical effects of advancing liver disease [69]. These consequences include gastro-esophageal varices, gastrointestinal bleeding, ascites, hepatorenal syndrome, and hepatic encephalopathy [14, 134, 10, 202]. Esophageal varices in particular continue to be the leading cause of death in patients with cirrhosis [176]. Acute esophageal varices, a direct consequence of increasing PVP, have been associated with a mortality of 20% within 6 weeks and immediate mortality of 5-8% [14]. Normal baseline hepatic venous pressure is 1-5 mmHg [69] and portal hypertension is defined as any PVP greater than this [134]. However, clinically significant portal hypertension is defined as a hepatic venous pressure gradient (HVPG) greater than

10 mmHg [70, 41]. Elevated HVPG is shown to predict clinical decompensation from cirrhosis, and produces better predictive accuracy for the prognosis of patients with liver disease than commonly used methods such as MELD or Child-Pugh scores [146, 108]. Various studies have shown that variceal bleeding and other major consequences of increasing PVP do not occur with HVPG measurements below 12 mmHg [187, 55]. The ability to distinguish clinically significant PVP would be important for prognostic and treatment purposes.

Monitoring of PVP is important in the clinical setting. It can be used primarily to guide treatment, as lowering the HVPG to below 12 mmHg is predicted to reduce the serious clinical sequelae of advancing liver disease and increasing hepatic pressure. Pharmacologic decrease of PVP has been associated with a concurrent improvement in liver function [20], and baseline PVP measurements have been shown to predict response to various pharmacologic treatments [20]. Measurement of PVP can also be useful in surgical planning, as elevated PVP is associated with increased mortality from abdominal surgery [113]. Current standards of treatment now suggest targets of pharmacologic lowering of HVPG 10-20% from baseline or decrease of HVPG to below 12 mmHg [14, 187, 55]. These targets have been shown to improve clinical outcomes through protection from variceal bleeding, formation of ascites, development of hepatorenal syndrome, and death in follow up [70, 181, 1, 39, 64]. The diversity of patient response to pharmacologic treatment as well as the variety of treatments available suggests that repeated measures of PVP would be desirable [16, 6, 104, 79]. Thus, a repeatable and inexpensive method for measuring PVP in vivo would be a highly desirable clinical tool.

1.2 Current methods for the measurement of portal venous pressure

Current methods of monitoring hepatic venous pressure rely on invasive or ultrasonic approaches. The invasive approaches tend to be more reliable but are expensive and

can be associated with side effects. The ultrasonic approaches have the advantage of being noninvasive and inexpensive but are less accurate. The most commonly used invasive approach to measuring hepatic pressure relies on occlusion of the hepatic vein using a balloon catheter to measure wedged hepatic pressure [69] and measuring the difference between this pressure and the free hepatic venous pressure. Essentially, this measurement of HVPG measures the gradient between the portal vein and the outflow into the inferior vena cava [69]. This measurement has been shown to correlate well with PVP in patients with cirrhosis [69, 174]. The rate of successful catheterization has exceeded 95% in recent years with skilled operators [69]. However, the expensive nature of an invasive approach, combined with the need for specialized training and equipment, has prevented the widespread adoption of HVPG monitoring [173]. Against this backdrop, a noninvasive approach to HVPG monitoring would lead to improved pharmacologic treatment planning for patients with worsening cirrhosis as well as increased adoption due to decreased cost.

Ultrasound is deployed widely in the evaluation of advancing liver disease. It can be used to look at the liver morphology as well as measurement of hepatic blood flow parameters for hepatic venous pressure assessment [197]. The two major effects of increasing portal venous pressure as a result of advancing liver disease on hepatic blood flow are (1) a decrease in blood flowing through the portal vein and (2) a resultant increase in blood flow in surrounding smaller blood vessels, called collaterals [16]. A major advantage of using ultrasound for this application, in addition to its noninvasive nature, is that qualitative investigation - such as location and functionality of collateral blood flow - can be evaluated in addition to quantitative metrics such as doppler ultrasonography. Color doppler ultrasonography (cDUS) is particularly useful for identification of increased collateral blood flow, but does not very accurately quantify decreased blood flow in the portal vein [197, 172]. Estimates of decreasing portal venous velocities as measured using duplex doppler ultrasound

(dDUS) are more accurate than those obtained using cDUS, but standardized values for diagnosis have not yet been developed because of variations in results obtained with different systems and personnel [197, 42, 154, 196, 80]. Thus, from a clinical perspective, a method for PVP measurement that could provide the noninvasive and qualitative insights of ultrasonography with superior quantitative reproducibility would be highly desirable.

1.3 Use of stiffness metrics to evaluate hepatic venous pressure

Recently, a novel approach using stiffness metrics for noninvasive hepatic pressure characterization has been proposed. Noninvasive estimates of liver stiffness can be achieved using a variety of imaging techniques, but all utilize the same underlying mechanical assumptions and phenomena. Essentially, a mechanical shear wave (defined as a wave in which the tissue displacement direction is perpendicular to the propagation direction) is excited and tracked in the tissue [68, 195]. Such methods can rely on tracking an externally-excited shear wave using either ultrasonic tracking, such as the transient elastography (TE) technique [157], or MRI-based tracking, termed magnetic resonance elastography (MRE) [78, 165]. Alternately, shear waves can be excited remotely using acoustic radiation force provided by the same ultrasound transducer used to track the shear waves [160, 116, 7, 52]. The advantages of the radiation force based approaches are that they use a clinical diagnostic ultrasound scanner and transducer, so they can be combined with qualitative ultrasound approaches for liver interrogation and included in a standard hepatic exam. They also directly couple the mechanical excitation into the liver, which overcomes some of the challenges faced by external vibration methods in larger patients and patients with ascites. The work described herein focuses on acoustic radiation force impulse (ARFI)-induced shear wave induction and tracking using a clinical diagnostic system, an approach which is described in more detail in Chapter 2.

Across all methodologies, shear wave speed (SWS) based estimates of liver mechanical properties have been observed to increase with PVP. Transient elastography has been the most widely explored with increases in its liver stiffness measures directly correlated with elevated hepatic pressures in animal models [107] and clinical patients [29, 186, 155, 25, 97]. Liver stiffness estimates based on TE have also been shown to predict long term complications from cirrhosis in patients similarly to HVPG estimates [149]. However, the main drawback of using liver stiffness estimates as a proxy for measuring PVP is that measurements of liver stiffness using transient elastography [168, 141, 28, 54], magnetic resonance elastography [161, 78], and radiation-force impulse induced shear wave elastography [128, 5], are all observed to increase with advancing liver fibrosis stage [38, 46]. Thus, liver fibrosis stage may provide a confounding effect on predictions of PVP using stiffness metrics. This behavior may also help explain the large variability in stiffness estimates at high hepatic pressures and fibrosis stages that has been observed in some studies [184, 141].

In addition to increases in stiffness metrics of the liver, SWS increases have also been observed in the spleen as a result of elevated PVP. MRE measures in animal models [112] as well as the clinical [171] setting have suggested that increasing PVP leads to higher SWS estimates in the spleen. These findings of increasing splenic stiffness with higher PVP have also been reported using radiation force based methods [170, 60]. In some cases, splenic stiffness from radiation force methods [170] and TE [169] has also been correlated with higher risk esophageal varices. Radiation force induced SWS estimates in the spleen have also returned partially toward normal after partial normalization of hepatic pressures with transjugular intrahepatic portosystemic shunt placement [60]. However, splenic stiffness is also increased generally in the presence of advancing hepatic fibrosis, which may lead to a confounding effect on the ability of splenic stiffness estimates to correlate with PVP metrics [171, 169].

Despite the promise shown by observations of increasing SWS-based stiffness estimates in the liver and spleen with higher portal venous pressures, the confounding effects of fibrosis stage on both of these measures suggest that further investigation is necessary into the mechanism by which these SWS increases are observed.

1.4 Theoretical factors that influence shear wave speed metrics

The two most common parameters that have been reported to affect the relationship between SWS estimates and underlying hepatic material properties are time-dependent, or viscoelastic, effects and strain-dependent, or nonlinear hyperelastic, effects. Viscoelastic effects on shear wave speed estimates manifest through dispersion as a change in phase velocity of the wave propagation as a function of frequency of shear wave speed excitation [159, 68]. The viscoelastic properties of tissue can be explored using external vibration [51, 22], magnetic resonance elastography [95], harmonically modulated radiation force excitations [33], and radiation force impulse based approaches [191, 110]. By contrast, the nonlinear properties of tissue-mimicking materials manifest as a change in SWS estimates as a function of material deformation. The examination of these properties using ultrasonic approaches has been explored in the context of acoustoelasticity experiments, where materials are deformed a known quantity and the change in SWS with applied strain is monitored [67]. Using various invasive and ex-vivo mechanical testing methods, the liver has been shown to have both viscoelastic and nonlinear behavior [86, 2, 114, 111, 82, 162, 103, 177]. The effect of portal venous pressurization on shear wave speed estimates is hypothesized to be nonlinear rather than viscoelastic because the excitation frequencies remain constant in the different methods used to observe this behavior and the deformation state of the liver is considered to be time-independent, due to the fact that the pressure remains relatively constant throughout interrogation of the liver stiffness. In this thesis, we present an experiment designed

to test this hypothesis and to demonstrate that the stiffening effect of PVP is a product of nonlinear behavior in Chapter 3.

1.5 Investigation of hepatic nonlinearity

Classical SWS-based exploration of material nonlinear properties relies on placing the material under a known deformation and tracking the change in SWS as a result of this applied strain [67, 163]. An example derivation for the SWS response to uniaxial compression in a nonlinear Mooney-Rivlin material as described by these types of experiments is described in Appendix A. The geometry of the pressurized liver, however, does not allow for simple modeling of the deformation that results from increasing PVP. The addition of fluid to the material observed during pressurization [151] suggests that it is unlikely to be represented by a simple uniaxial stress experiment because expansion is expected to be uniform in all directions. In order to explore the relationship between hepatic deformation and SWS estimates in the context of increasing PVP, quantitative tools to measure hepatic deformation in three dimensions were developed and implemented in this thesis. The methods used for 3-D ultrasound based interrogation of hepatic displacement are described in Chapter 4. Simulations (described in Chapter 5) were performed to validate the ultrasound-based methods of displacement and strain estimation in 3-dimensions. The tools described in Chapters 4 and 5 were then combined with the experimental setup developed in Chapter 3 to explore the relationship between shear wave speed and deformation in the liver with increasing PVP in Chapter 6. The hypothesis developed and tested in this work utilizing the experiments described is that *shear wave speed estimate increase with increasing portal venous pressure occurs as a result of a nonlinear hyperelastic behavior and is associated with a corresponding increase in measures of hepatic strain.*

2

Background

2.1 Ultrasound Imaging

Classical ultrasound imaging systems provide real-time 2 or 3 dimensional images of tissue. They rely on generation of sound pulses and detection of returning echoes using a transducer composed of piezoelectric elements that convert voltage to pressure and vice versa for the returning waves. A traditional 2-dimensional image is composed of many amplitude or A-lines at each lateral position in which the displayed brightness is related to the amplitude of the received signal at each depth (related to arrival time by the speed of sound). A block diagram of an ultrasound imaging system can be seen in Figure 2.1. Sound waves are longitudinal waves that propagate through periodic perturbations in local pressure and compression. This propagation is described by the speed of sound (c_o), which depends on the bulk modulus (B) and material density (ρ_o), as shown in Equation 2.1.

$$c = \sqrt{\frac{B}{\rho_o}} \quad (2.1)$$

The varying amplitudes in an ultrasound image that provide the basis for contrast

are related to acoustic impedance (Z) differences (see Equation 2.2 in which Z is the acoustic impedance, ρ_o is the material density, and c_o is the speed of sound in the material)

$$Z = \rho_o c_o. \quad (2.2)$$

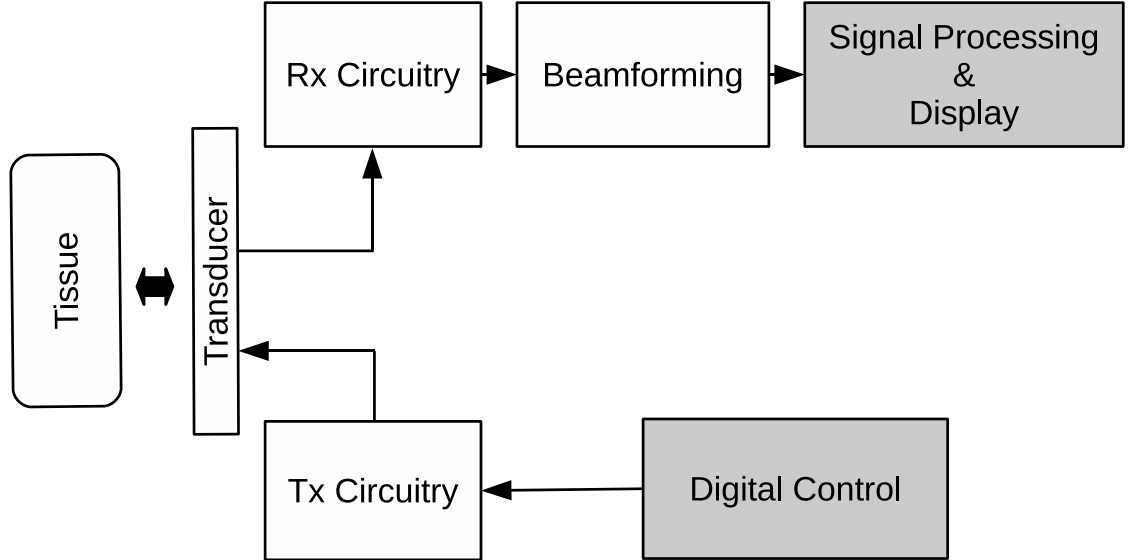


FIGURE 2.1: Flowchart of an ultrasound imaging system. The grey shaded regions on the flowchart are those modified in generating and tracking displacements caused by Acoustic Radiation Force Impulse (ARFI) excitations.

Attenuation of ultrasound pulses in tissues can occur due to two primary effects: scattering and absorption. For an idealized tissue composed of Rayleigh scatterers, the scattering will depend on the frequency of excitation, radius, compressibility, and density of the scatterer as compared with the surroundings (usually assumed to be water) [36]. Most attenuation of ultrasound pulses in tissues occurs due to absorption [133], which describes the loss of ultrasound signal intensity with propagation due to the transfer of energy from the propagating ultrasound wave to the tissue.

2.2 Acoustic Radiation Force

Acoustic radiation force relies on the transfer of energy from the propagating ultrasound wave to the tissue, causing a slight (μm) displacement in the direction of wave propagation [131]. Loss of acoustic energy during propagation in tissue occurs due to both scattering and absorption, and both mechanisms can lead to radiation force [117]. However, absorption provides the majority of tissue attenuation, so it is assumed to be the primary source of observed soft tissue displacement. Under the assumptions of tissue behaving as an incompressible linearly viscous fluid at ultrasonic frequencies and plane wave propagation of the ultrasound waves, the equation for radiation force (\mathbf{F} [kg/(s²cm²)] as a function of temporal average acoustic intensity (\mathbf{I} [W/cm²]), amplitude attenuation coefficient (α [Np/m]), and speed of sound (c_o [m/s]) is [121]:

$$\mathbf{F} = \frac{2\alpha\mathbf{I}}{c_o} \quad (2.3)$$

As implemented for the ARFI imaging described herein, standard clinical ultrasound scanners are used to generate impulsive acoustic radiation force in tissue [131]. The acoustic radiation force is localized to a region of excitation (ROE) that is determined by the focal configuration of the system and attenuation of the tissue. This ROE is usually within 2 mm lateral extent \times 10-20 mm axially \times 0.5-2 mm in the elevation dimension in the tissue and 60-400 μs in duration [131] (see Figures 2.2 and 2.3). Ultrasound-based displacement tracking methods (see section 2.3) are used to monitor the mechanical response of the tissue through time [131, 115, 116, 118, 119]. Commonly observed tissue mechanical behaviors when excited by ARFI are discussed further in section 2.4.

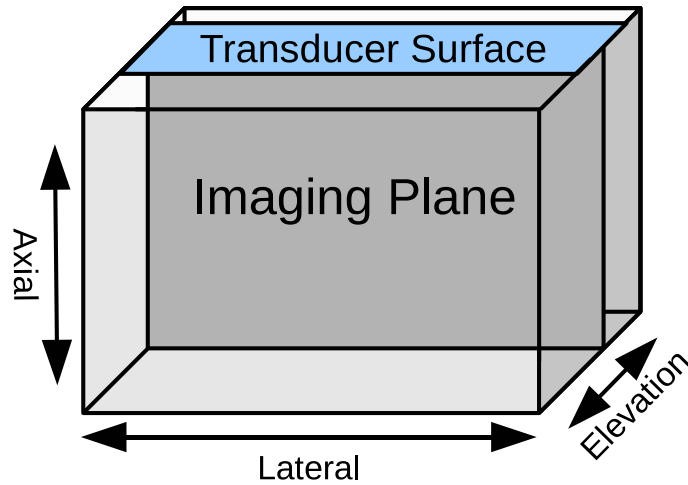


FIGURE 2.2: Diagram of a typical dimension nomenclature and distribution of an ultrasound image.

2.3 Ultrasonic Displacement Tracking

ARFI based imaging requires the generation and tracking of local displacements in tissue. ARFI generates axial displacements in the direction of ultrasound wave propagation (away from the transducer) of magnitude approximately $0.1-0.01(\lambda_u)$, where λ_u is the ultrasound wavelength [138]. In order to track these types of displacements, the pushing beam is preceded by a reference line and followed by a series of tracking beams in a typical A-line configuration. These tracking beams can either be on the axis of the push to generate a qualitative stiffness map of underlying tissue [127, 131, 152], or offset from the push in various lateral locations to monitor the associated shear wave propagation away from the ROE, which can be used to generate a quantitative stiffness estimate of underlying tissue (see section 2.6). The most commonly used techniques for axial displacement estimation caused by an ARFI excitation are normalized cross correlation, Kasai's algorithm, and Loupas' algorithm

[136, 85, 100].

For the work described herein, the Loupas phase shift estimator has been used [137, 100]. The phase shift of the signal between subsequent tracking lines can be converted to a displacement estimate at each axial position using an assumed speed of sound.

Sources of Error in Displacement Estimation

Displacement tracking with ultrasound is subject to many sources of error, primarily decorrelation, electronic noise, and motion. There are two major types of errors that are observed when using the Loupas phase-shift estimator: phase wrapping and jitter.

Phase wrapping errors can be mitigated by having a high pulse repetition frequency (PRF) in order to prevent aliasing errors. In addition, nonlinear post-processing algorithms that identify discontinuities in displacement estimates can be used to limit displacement estimates from $-\lambda_u/2$ to $\lambda_u/2$ [11, 190].

Displacement estimation relies on determination of time or phase shift between two partially-correlated signals. Small error estimates (less than $\frac{\lambda_u}{2}$) lead to increase in displacement estimation variance (jitter). Jitter can be caused by signal decorrelation, noise, and sampling effects [190]. The lower bound for displacement estimation jitter of cross correlation based estimates has been related to the Cramer-Rao Lower Bound (CRLB) [137, 190, 125]:

$$Jitter \geq \sqrt{\frac{3}{2f_c^3\pi^2T(BW^3 + 12BW)} \left[\frac{1}{\rho^2} \left(1 + \frac{1}{SNR^2} \right)^2 - 1 \right]} \quad (2.4)$$

Where *Jitter* depends on signal-to-noise ratio (SNR), fractional bandwidth of the transducer (BW), kernel size (T), correlation coefficient between reference and tracked RF-data (ρ), and center frequency of the tracking (f_c).

As we might expect, jitter reduction can be achieved with higher tracking frequency, higher transducer bandwidth, increased kernel size, and better correlation between tracked lines. For the experimental setups described herein, the standard deviations of on-axis displacement magnitudes at the focus of excitation (jitter) is experimentally determined to be approximately $1.5 \mu m$ for our experimental setup [190, 137], providing a lower bound on the precision of axial displacement estimates.

2.4 Acoustic Radiation Force Impulse (ARFI)-based imaging

The dynamic response of soft tissue to ARFI excitation relies on the properties of the ultrasonic system used for excitation and on the underlying material properties of the tissue. These have primarily been studied using ultrasonic tracking combined with displacement estimation methods discussed in sections 2.2 and 2.3. An example of the soft tissue response to an ARFI excitation from mechanical finite element simulations is shown in Figure 2.3 [131].

The axial region in which the ARFI excitation remains constant in the lateral and elevation dimensions, called the depth of field (DOF), can be estimated [36]:

$$DOF = 8F^2\lambda \quad (2.5)$$

Where F is the $F/\#$ of the focal configuration used for imaging ($F = \frac{z}{D}$) equal to the focal depth (z) divided by the aperture size (D). In Figure 2.3, the excitation frequency is 7.27 MHz, and the DOF is calculated to be 1.7 mm axially. There are two types of information that are usually generated by exciting and tracking ARFI displacements in a particular DOF. The first, qualitative stiffness imaging, is aimed at generating a relative stiffness map for identifying mechanical heterogeneities in tissues [129, 152]. The second, shear wave elasticity imaging (SWEI) targets the propagation of the axial displacement transverse wave laterally in tissue to generate a quantitative estimate of shear wave speed (SWS) [160].

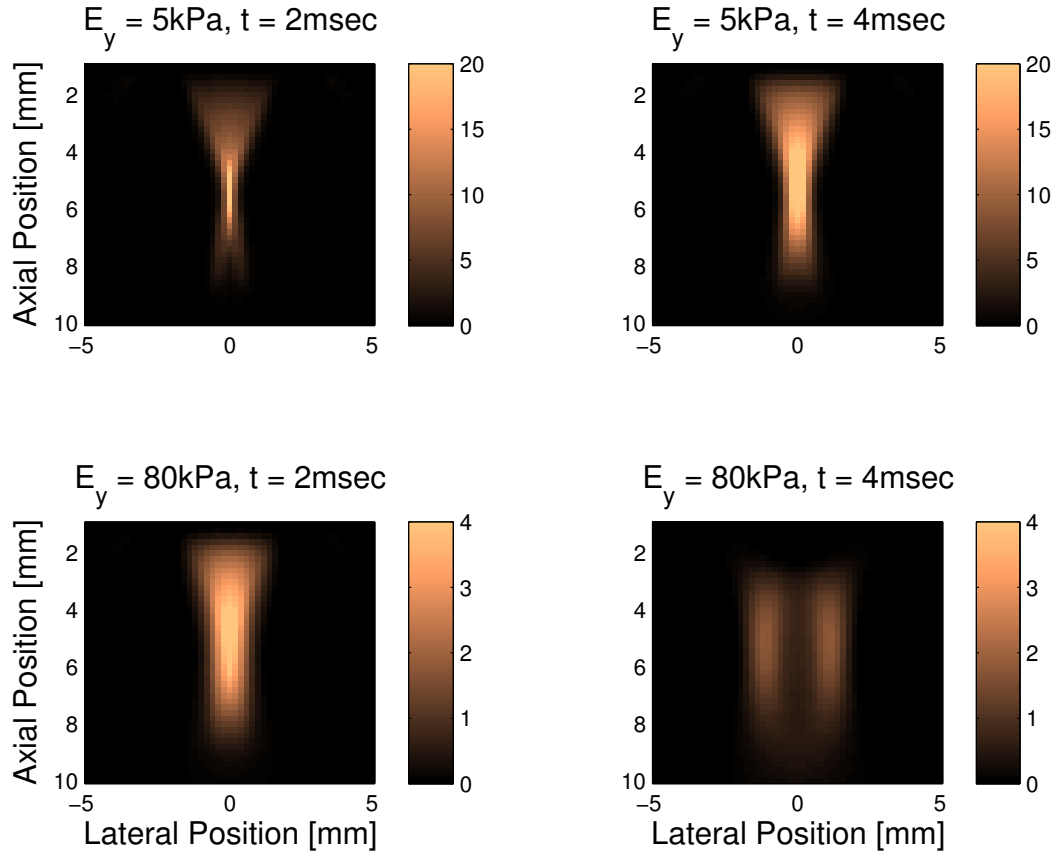


FIGURE 2.3: Examples of simulated axial displacements (as represented by the colorbars in units of μm) at 0.2 msec (left column) and 0.4 msec (right column) after the ARFI push beam in a soft ($E_y = 5 \text{ kPa}$, top row) and stiff ($E_y = 80 \text{ kPa}$, bottom row) elastic solid [130]. Simulations were performed for a SIEMENSTM14L-5 transducer focused at 5.5 mm in depth and using 7.27 MHz for push beams. Both the higher amplitude displacement in the softer material as compared with the stiffer material, and the slower propagation of the axial displacement laterally (in a transverse or shear wave) in the softer material demonstrate the potential for ARFI-based imaging to analyze tissue mechanical properties.

Qualitative Stiffness Imaging

As observed in Figure 2.3, the magnitude of ARFI-induced displacement varies between stiffer and softer materials [120]. The displacement magnitude also depends on other factors such as attenuation, aberration, and focusing, so displacement magnitude images are primarily used for imaging relative mechanical properties in a

particular area of tissue. These types of qualitative images are generated by tracking on the axis of the ARFI excitation. An example of this type of image from experimentally-acquired datasets using the Siemens ACUSON™clinical S2000 ultrasound scanner and a 14L-5 linear array (Siemens Medical Systems, Ultrasound Group, Issaquah, WA, USA) at 7.27 MHz and F/1 focal configuration is shown in Figure 2.4.

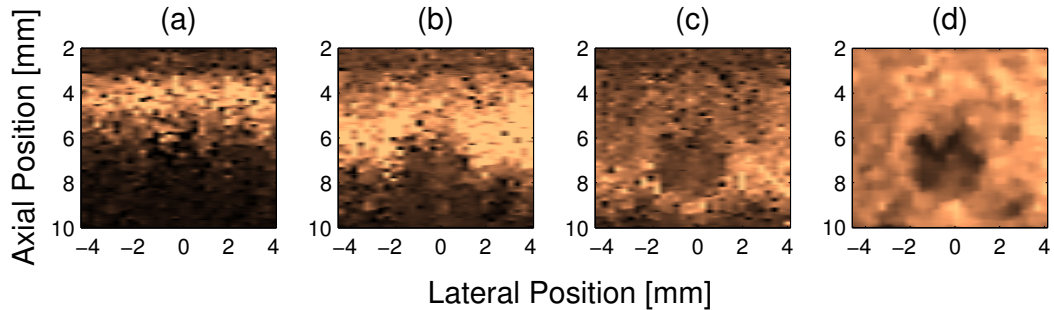


FIGURE 2.4: Qualitative stiffness images of a 4 mm diameter stiff lesion in a tissue-mimicking phantom (Computerized Imaging Reference Systems, Norfolk Virginia) acquired by tracking along the axis of the ARFI excitation. The phantom has an acoustic attenuation of 0.7 dB/cm/MHz. Experiments were performed with a SIEMENS™14L-5 transducer focused at 5.5 mm in depth and using 7.27 MHz for push and track beams. Displacements in subfigures a,b, and c are shown on a scale from zero to 8 microns at 0.2 msec after the ARFI excitation. The brighter areas represent greater displacements which correspond to softer materials. Subfigure a shows the results from an excitation focused at 3.5 mm axially, subfigure b shows the results from an excitation focused 5.5 mm axially, and subfigure c shows the results from an excitation focused at 7.5 mm axially. Subfigure d shows the average of the three focal zone images acquired with focal gain correction and a 0.4×0.6 mm median filter applied. Because displacement magnitude depends on a variety of factors including the ultrasound power supply, tissue attenuation, and geometric lesion effects, the displacement ratio cannot be used as a quantitative measure of stiffness. It can, however, be used as a qualitative depiction of areas that are stiffer or softer than others in the same field of view.

Figure 2.4d demonstrates how the limitations of a confined focal region can be mitigated by using information from several focal configurations combined with gain correction and median filtration. Relative stiffness imaging can be used to identify mechanical inhomogeneities in tissues [152, 201].

Shear Wave Elasticity Imaging

Tissue stiffness can be quantified using shear wave imaging methods [160, 61, 116, 66]. Acoustic radiation force-based methods have yielded consistent and informative liver stiffnesses in clinical subjects with different stages of fibrosis, commonly relying on time-of-flight (TOF) calculation algorithms to identify the arrival time of the wave at various lateral locations [128, 192]. Ultrasonically-tracked displacements through time at each lateral position are used to identify the arrival time for SWS approximation [132, 156]. After determination of SWS, the relationship between the shear wave speed and underlying tissue mechanical properties can be inferred by choosing a specific tissue mechanical model. Often, material linearity, isotropy, incompressibility, and elasticity are assumed [128, 158, 56, 110]. Under these conditions, the shear wave speed (c_T) is related to shear modulus(μ) and density (ρ) as:

$$c_T = \sqrt{\frac{\mu}{\rho}} \quad (2.6)$$

In this thesis, shear wave elasticity imaging (SWEI) relies on ARFI-based quantitative stiffness estimates in which ARFI pushing beams are held at a constant lateral position and each followed by sequential ultrasonic tracking at various locations. A diagram of this experimental configuration is shown in Figure 2.5. A representative dataset acquired in a tissue-mimicking phantom is shown in Figure 3.2.

As shown in Figure 3.2, the peak displacement moves laterally in a homogenous medium at a constant speed. While ordinarily displacement estimates are expected to begin and end at zero, system artifact, transducer face heating, and master clock jitter as well as undersampling may contribute to the nonzero initial and final displacements. Motion, jitter, and sampling rate limitations can also lead to SWS estimation error. In this work, iterative outlier removal is used to generate TOF estimates in order to better estimate shear wave speeds with noisy data. This method

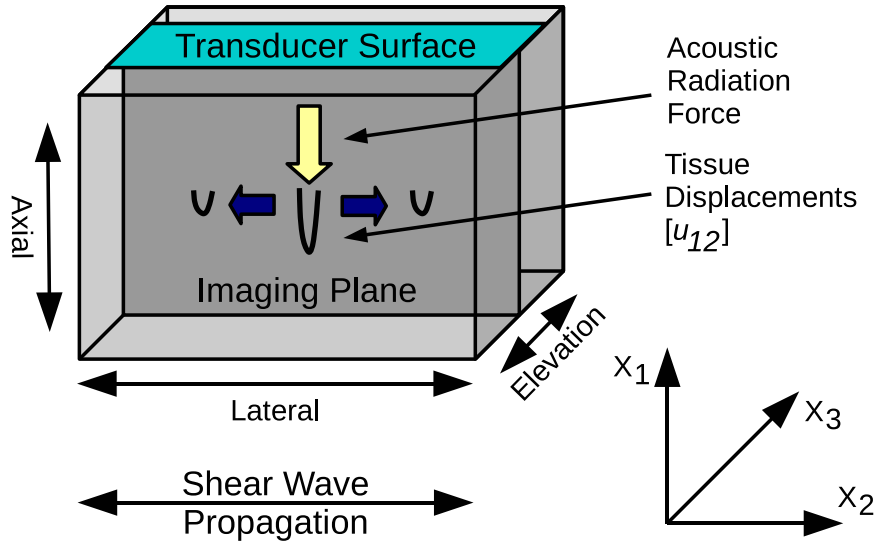


FIGURE 2.5: Diagram of shear wave propagation as generated by an acoustic radiation force impulse.

is based on the random sample consensus (RANSAC) algorithm and has been validated [192]. All datasets with fewer than 40% outliers removed during the iterative line fitting process were kept for shear wave speed calculations. Figure 2.7 shows the precision of RANSAC-based SWS estimation in calibrated tissue-mimicking elasticity phantoms. The precision of shear wave speed estimates is observed to worsen with increasing shear wave speed due to limitations in temporal sampling with the system used.

The primary goal of the work in this thesis is to discover the underlying relationship between shear wave speed estimates in excised canine livers and tissue mechanical properties. Appendix A describes a derivation in which a nonlinear model (Mooney-Rivlin) is assumed and shows the resulting change in shear wave speed that can occur in a deformed nonlinear material [17]. The experiments and

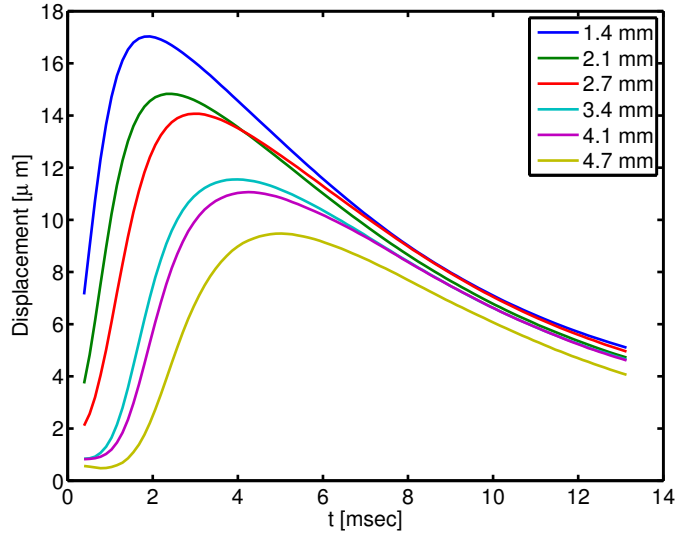


FIGURE 2.6: Sample experimental dataset showing displacements at various lateral positions at one axial depth, the focal depth of 5.5 mm. The tissue-mimicking phantom has a calibrated Young’s Modulus of 4.5 kPa. The ARFI push occurs at lateral position = 0 mm and the displacement through time profiles as tracked ultrasonically and calculated by the Loupas estimation algorithm at various lateral locations are shown. Each colored line represents a different lateral position, and the shear wave speed can be calculated by observing the arrival time shift as the wave propagates laterally. A 1000 Hz low-pass filter has been applied to the displacements in the time dimension.

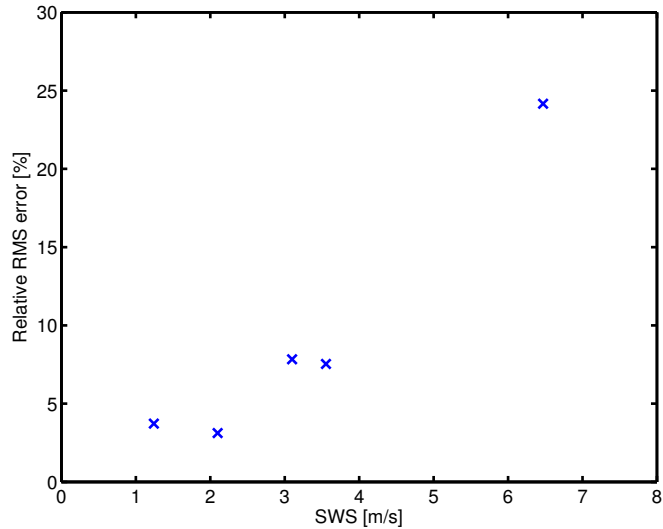


FIGURE 2.7: Relative RMS error for Ransac-based SWS estimation over 12 locations in each of 5 calibrated tissue-mimicking elasticity phantoms.

tools designed were devoted to determining whether the liver behaves nonlinearly when pressurized and to elucidating the quantitative relationship between the tissue deformation and the shear wave speed changes with increasing hepatic pressure.

The Impact of Hepatic Pressurization on Liver Shear Wave Speed Estimates in Constrained vs. Unconstrained Conditions

*This chapter has been published in the journal *Physics in Medicine and Biology* 57(2) pages 329-341 (2012). This work was chosen by the editor to be highlighted in an article in *MedicalPhysicsWeb* on Jan 18, 2012.*

3.1 Abstract

Increased hepatic venous pressure can be observed in patients with advanced liver disease and congestive heart failure. This elevated portal pressure also leads to variation in acoustic radiation-force derived shear wave based liver stiffness estimates. These changes in stiffness metrics with hepatic interstitial pressure may confound stiffness-based predictions of liver fibrosis stage. The underlying mechanism for this observed stiffening behavior with pressurization is not well understood, and is not explained with commonly-used linear elastic mechanical models. An experiment was designed to determine whether the stiffness increase exhibited with hepatic pressurization results from a strain-dependent hyperelastic behavior. Six excised canine

livers were subjected to variations in interstitial pressure through cannulation of the portal vein and closure of the hepatic artery and hepatic vein under constrained conditions (in which the liver was not free to expand) and unconstrained conditions. Radiation force derived shear wave speed estimates were obtained and correlated with pressure. Estimates of hepatic shear stiffness increased with changes in interstitial pressure over a physiologically relevant range of pressures (0-35mmHg) from 1.5 to 3.5 m/s. These increases were observed only under conditions in which the liver was free to expand while pressurized. This behavior is consistent with hyperelastic nonlinear material models that could be used in the future to explore methods for estimating hepatic interstitial pressure noninvasively.

3.2 Introduction

Advanced chronic liver disease (cirrhosis) is the twelfth leading cause of death in the United States with an approximate incidence worldwide of 1 in every 1,000 subjects [63]. The progression of cirrhosis is marked by two important consequences: liver dysfunction, and portal hypertension [63]. Liver dysfunction is often characterized using a combination of serum testing and liver biopsy, while portal hypertension is usually measured by hepatic venous pressure gradient (HVPG). Ultrasound provides an opportunity to evaluate two aspects of clinical hepatic disease that are traditionally measured invasively: liver fibrosis and HVPG [53]. The first, liver fibrosis, has been extensively studied with relation to comparing biopsy-based fibrosis stage to quantitative estimates of liver stiffness [126, 58, 199, 18, 28, 5]. Specifically, Transient Elastography [158], Magnetic Resonance Elastography [78], and Acoustic Radiation Force Impulse (ARFI) [192, 126, 87, 143, 5] based quantitative estimation of tissue stiffness have been successful in distinguishing fibrosis stage noninvasively. Recent studies have suggested that ultrasound-based estimates of liver stiffness also increase with hepatic venous pressurization [107, 185, 25, 149], but the underlying

mechanism for this observed stiffening is not understood.

HVPG measurement in liver disease is important for predicting disease progression, guiding treatment, and longitudinal monitoring [63, 15]. HVPG has been shown to be the most robust predictor of disease progression, or decompensation in patients with cirrhosis [146]. Decompensated cirrhosis is associated with a 30% decrease in 1-year survival for patients with cirrhosis, and is characterized by variceal bleeding, encephalopathy, and jaundice [40]. Specifically, increased HVPG above 10 mmHg (from 5 mmHg normal) predicts variceal bleeding, decompensation of cirrhosis, and hepatocellular carcinoma development [39, 21, 88, 98]. In addition to its prognostic value, lowering HVPG pharmacologically in a cirrhotic patient to below 12 mmHg or 20% decrease from baseline significantly decreases risk of hemorrhage, ascites, encephalopathy, and death [39, 188]. Finally, prediction of portal pressure can inform treatment, such as life expectancy prediction for liver transplant guidance [40] and outcome and safety estimates for antiretroviral therapy in patients with hepatitis C virus related cirrhosis [141]. HVPG is useful at all stages of liver disease, for prognostication, longitudinal tracking, or treatment decision-making purposes [106].

Unfortunately, current methods of HVPG measurement involve portal vein catheterization, which is highly invasive, expensive, and can lead to complications such as infection [106, 142]. Clearly, a non-invasive metric for HVPG measurement would be highly beneficial to reduce these risks and improve liver disease treatment. The greatest current challenge to measuring HVPG noninvasively using elasticity metrics remains that the stiffening observed with advanced fibrosis cannot currently be distinguished from that which may be due to elevated HVPG [149]. This study is aimed at exploring differences in the underlying tissue behavior for these two stiffening effects observed in advanced liver disease.

3.3 Background

Tissue stiffness can be quantified using shear wave imaging methods [160, 61, 116, 7, 32]. Acoustic radiation force-based methods have yielded consistent and informative liver stiffnesses in clinical subjects with different stages of fibrosis, commonly relying on time-of-flight (TOF) calculation algorithms to identify the arrival time of the wave at various lateral locations [5, 126, 192]. Ultrasonically-tracked displacements through time at each lateral position are used to identify the arrival time for SWS approximation [132, 156, 105]. After determination of SWS, the relationship between the shear wave speed and underlying tissue mechanical properties can be inferred by choosing a specific tissue mechanical model. Often, material linearity, isotropy, incompressibility, and elasticity are assumed [126, 158, 56, 110]. Under these conditions, the shear wave speed (c_T) is related to shear modulus(μ) and density (ρ).

$$c_T = \sqrt{\frac{\mu}{\rho}} \quad (3.1)$$

Shear wave speeds have been observed to increase with increasing pressure in excised porcine livers [107] and in humans with elevated portal hepatic pressures [184, 25, 149]. This result is inconsistent with the linear elastic assumptions expressed in Equation 3.1. A change in estimates of liver stiffness with pressure implies a non-linear relationship between stress and strain of a particular material [94, 122]. Non-linear materials which display time-independent elastic behavior (such as rubbers, foams, and tissues) are classically described by hyperelastic theories [19, 59, 122]. Hyperelasticity encompasses many possible nonlinear mechanical models of solids, all of which are described by an assumed strain energy function. The strain energy function can be used to derive strain-dependent stress-strain relationships under different boundary conditions. These models are relevant to the question of hepatic

pressurization because there is evidence that increased hepatic pressure leads to a change in the underlying strain state of the liver. Hepatomegaly, an increase in liver size that would imply a change in underlying liver strain state, has also been reported in patients with increased portal pressure due to right-sided congestive heart failure [37, 53]. The question addressed in this work is whether deformation is necessary to observe increases in measured shear wave speeds with increased hepatic pressure. If the increase in stiffness metrics are associated with hepatic deformation, this result would imply that hyperelastic material models are necessary for describing this behavior.

Extensive theoretical work in nonlinear mechanics has been devoted to analytic predictions of wave speeds under different boundary conditions and material models for soft solids like tissue [17, 45, 44, 200]. Acoustoelastic techniques take advantage of these analytic predictions by characterizing tissue using measured wave speeds in uniaxially compressed hyperelastic materials [163, 89, 178] and have been previously reported using shear wave speed metrics in tissue-mimicking materials [30, 67]. In acoustoelastic testing methods, an underlying hyperelastic expression is assumed, and then the mechanical properties (or parameters of the constitutive model) are determined by measuring wave speed in a compressed material and fitting the experimental results to the material constants of the assumed material model [89]. Hepatic pressurization does not lend itself to explicit characterization by acoustoelastic techniques because of its geometric complexity and because the appropriate hyperelastic model has not yet been determined. In particular, the hepatic pressurization condition does not correspond to that of uniaxial compression, which is examined using acoustoelastic techniques. The study presented herein was designed to test the hypothesis that liver material nonlinearity manifesting as finite strain deformation with hepatic pressurization leads to increased shear wave speeds.

3.4 Methods

3.4.1 *Experimental Setup*

Experimental Animals All experiments were performed using freshly harvested canine livers. The canines were obtained through the Duke University Vivarium, and euthanasia was achieved through methods approved by the Duke Institutional Animal Care and Use Committee (IACUC). Three minutes prior to euthanasia, 3 mL of heparin was given to the animal to prevent clotting in the liver during the experiment. After euthanasia the canine liver was removed, with care taken to preserve the inflow and outflow tracts.

Constrained versus Unconstrained Data Acquisition In order to evaluate the effect of strain on pressure-related observations of shear wave speed changes, a custom experimental setup (see figure 3.1) was constructed to evaluate SWS in the liver under first constrained and then unconstrained conditions. A variable height watertight cylinder was designed with a top transducer window, water release valves and side portal vein access port. The liver was placed within the cylinder, the hepatic artery and vein were closed, and the portal vein was connected to the exterior through an access port for pressurization and connection to a digital manometer (SPER Scientific, Ltd., resolution = 0.075 mmHg). The liver was surrounded with phosphate buffered saline (PBS), with a 4 cm PBS fluid path between the acoustic window and surface of the liver. Air was removed and all valves were closed. Datasets were acquired with pressurization with the valves closed (the constrained condition). Pressure was increased in 5 mmHg steps from 0-45 mmHg by raising the saline reservoir. Then, the reservoir was lowered to achieve 0 mmHg pressure and the valves were opened to allow saline to overflow as the liver expanded with pressurization. The pressurization and data acquisition protocol was repeated in this unconstrained scenario with the

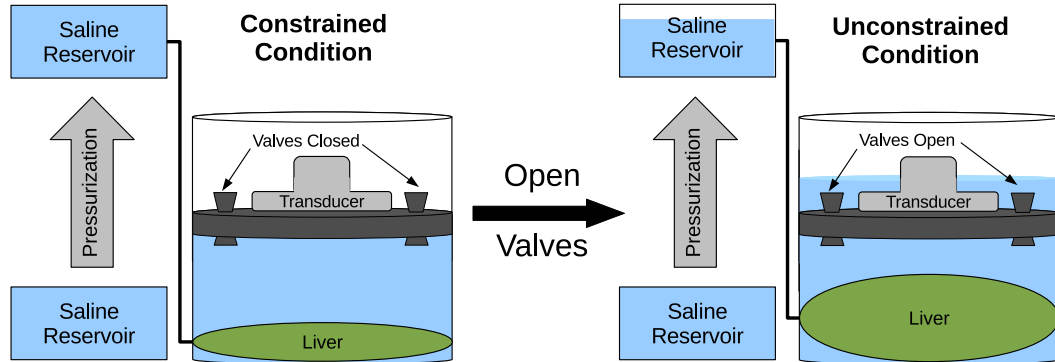


FIGURE 3.1: Diagram of the experimental setup for comparison between excised canine livers that were or were not constrained from deformation throughout pressurization. The increase in hepatic pressure was accomplished by raising the saline reservoir from the level of the portal vein as shown above.

valves open. At each pressurization step, 6 SWS datasets were acquired in the same location with the speeds averaged together to provide a single SWS estimate for each pressurization step.

3.4.2 SWS Estimation Methods

Ultrasonic Parameters Shear waves were generated with focused acoustic radiation force in the ex-vivo livers using a Siemens ACUSON™S2000 scanner and a 4C-1 curvilinear array (Siemens Medical Systems, Ultrasound Group, Issaquah, WA, USA) focused at between 35 mm to 50 mm operating at 2.6 MHz (F/# 3.5). The system has been modified for user control of acoustic beam sequences and intensities, as well as allowing access to the radio-frequency in-phase and quadrature (IQ) data. Data acquisition was performed using a modified version of the Siemens Virtual Touch™tissue quantification tool, with custom processing as described below. The transmit power was increased from standard settings in all collected datasets and the corresponding acoustic output is shown in table 3.1. For each shear wave dataset,

an 8 mm \times 5 mm region of interest (ROI) was interrogated. For each radiation force excitation, or "push," four parallel lateral positions were tracked for a duration of 10 msec, with pulse repetition frequency (PRF) varying from 7-10 kHz with deeper focii corresponding to a slower PRF. Twenty-eight lateral positions spaced 0.17 mm apart were tracked for each push location, requiring 7 pushes. This sequence was repeated once with a push on the left side of the ROI with tracking to the right and once with the push on the right side of the ROI with tracking to the left. The SWS estimates from each push location were then averaged to obtain one SWS estimate. This protocol was repeated 6 times without moving the ROI and the 6 SWS estimates were averaged to obtain one SWS estimate per pressurization condition from each of 6 excised canine livers. Figure 3.2 shows examples of individual datasets acquired in two different unconstrained pressurization conditions. Table 3.1 shows the ultrasound imaging parameters in detail.

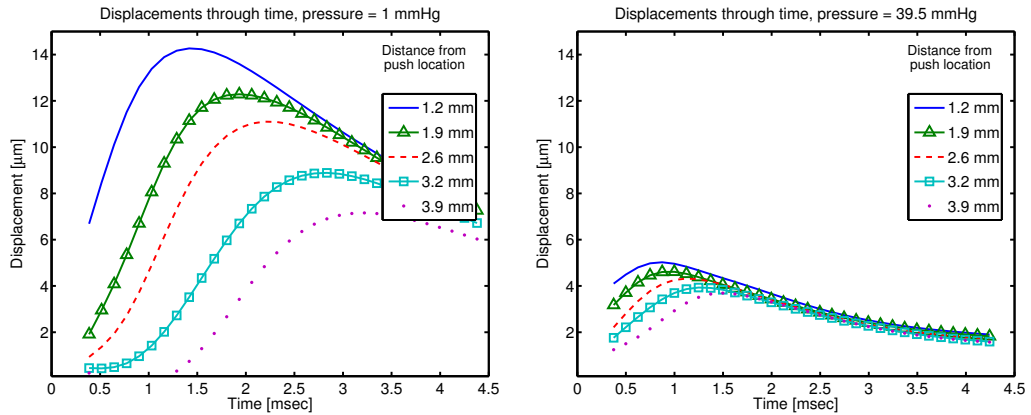


FIGURE 3.2: Two sample unconstrained experimental datasets. Average axial displacements over 4.4-5.1 cm in depth are shown at various lateral positions. The ARFI push occurs at lateral position = 0 mm and the displacement through time profiles as tracked ultrasonically and calculated by the Loupas estimation algorithm [100] are shown. A 1000 Hz low-pass filter has been applied to the displacements in the time dimension. At increased pressure, the displacement amplitudes are observed to be smaller and the displacement peaks occur earlier in time, both of which correspond to faster shear wave speed propagation and increased material stiffness.

Dataset Processing Datasets were processed offline using MATLAB (MathWorksTM, Natick, MA). Local displacement estimates were calculated using the Loupas phase-shift estimator [100, 136]. Displacements from positions 1.4-8 mm lateral to the region of excitation were used to generate shear wave speed estimates using a RANSAC-based time-of-flight algorithm [192, 132]. The RANSAC-based SWS estimator uses an iterative removal of outliers method, which was exploited to eliminate datasets that had greater than 50% outliers. Then, the shear wave speed is found from the inverse slope of the time to peak displacement versus lateral position. Two example datasets are shown in figure 3.3 after the iterative removal of outliers procedure. This process was repeated for both the left and right side shear wave excitations for each of the 6 repeated data acquisitions in a given liver at each pressurization level to obtain a single SWS estimate. The mean SWS at each pressure for each of 6 canine livers were compiled and sorted into 11 equally-spaced bins between 2.25 and 45 mmHg to generate mean and standard deviation of SWS for each pressure bin across all six animals.

Table 3.1: Radiation Force Sequence Parameters

Parameter	Value
Ultrasound Scanner	S-2000
Probe	4C-1
Push Frequency	2.67 MHz
Track Frequency	3.08 MHz
Push Cycles	400
Push Duration	180 μ s
Push F#	3.5
Push Focal Depth (lateral)	3.5-5.0 cm
Elevation Focus	4.9 cm
$I_{sppa} (H_2O)$	1544 W/cm ²
$I_{sppa} (\alpha = 0.3)$	626 W/cm ²
MI (0.3)	1.9

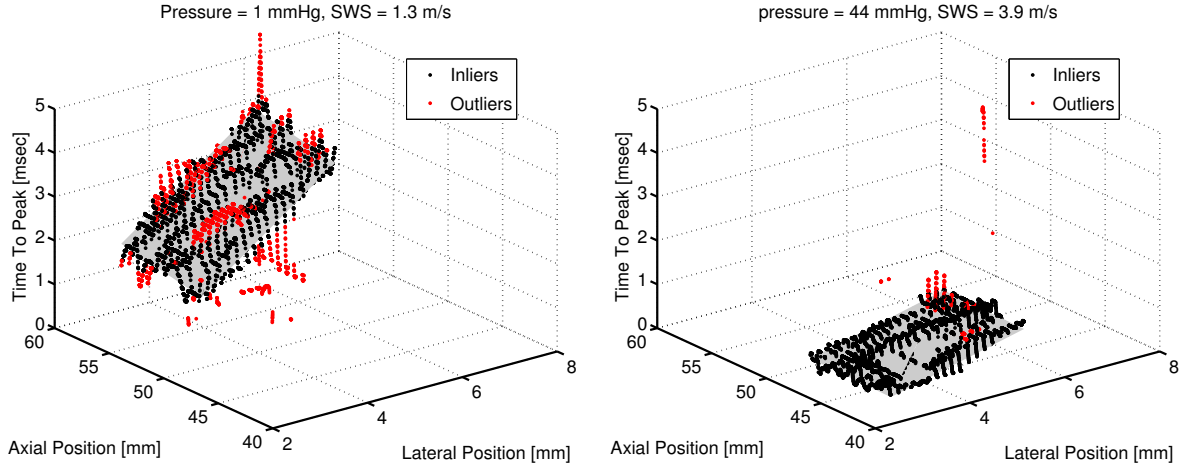


FIGURE 3.3: The RANSAC-based iterative removal of outliers as implemented for SWS estimation [192] is shown for the two datasets examined in figure 3.2. A steeper time to peak displacement versus lateral position corresponds to a slower shear wave speed as shown for the figure on the left at 1 mmHg hepatic pressure as compared with the figure on the right at 44 mmHg pressure. Both datasets were collected in the unconstrained case for which the liver was allowed to expand with increased pressure.

3.4.3 Statistical Analysis

The SWS estimates at increasing pressures were compared between unconstrained and constrained pressurization cases. An analysis of variance (ANOVA) as implemented in MATLABTM was performed on the acquired datasets to compare the constrained and unconstrained datasets at each pressure state [43]. In addition, a linear regression analysis between the average SWS and pressure in all six experimental animals for the unconstrained and constrained cases was used to identify the dependence of SWS on pressure for the two experimental conditions.

3.5 Results

3.5.1 Constrained and Unconstrained Comparison

A sample set of data collected for the constrained/unconstrained conditions in a single experimental liver is shown in figure 3.4.

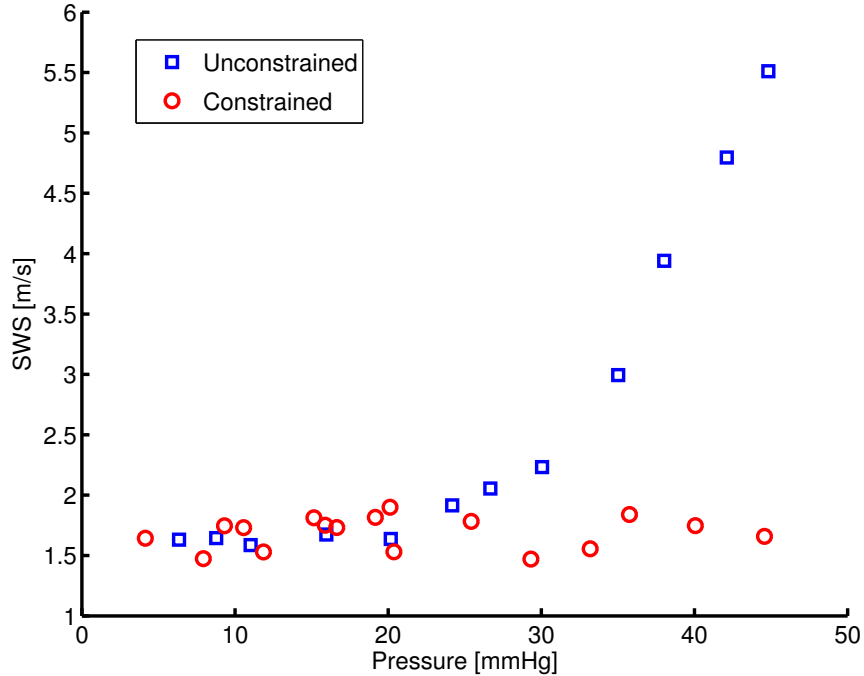


FIGURE 3.4: Comparison within one ex-vivo canine liver between a pressurized case limited in volume (constrained, shown with circles) to one allowed to expand (unconstrained, shown with boxes).

The compiled mean SWS binned into evenly spaced pressure bins across six experiments can be seen in figure 3.5. When the liver is constrained, shear wave speed does not vary with pressure (figures 3.4 and 3.5, red circles). When the liver is unconstrained, the SWS is observed to increase with pressure (figures 3.4 and 3.5, blue squares).

ANOVA were performed between unconstrained and constrained SWS across six animal experiments at each pressure. Statistically significant ($p < 0.01$) differences between the two groups were observed in the pressure bins with mean pressure greater than 20 mmHg. In order to determine the correlation between pressure and shear wave speed estimates for each experimental condition, a linear regression analysis was performed on the constrained and unconstrained datasets as shown in figure 3.6 and results from the linear fit are shown in table 3.2.

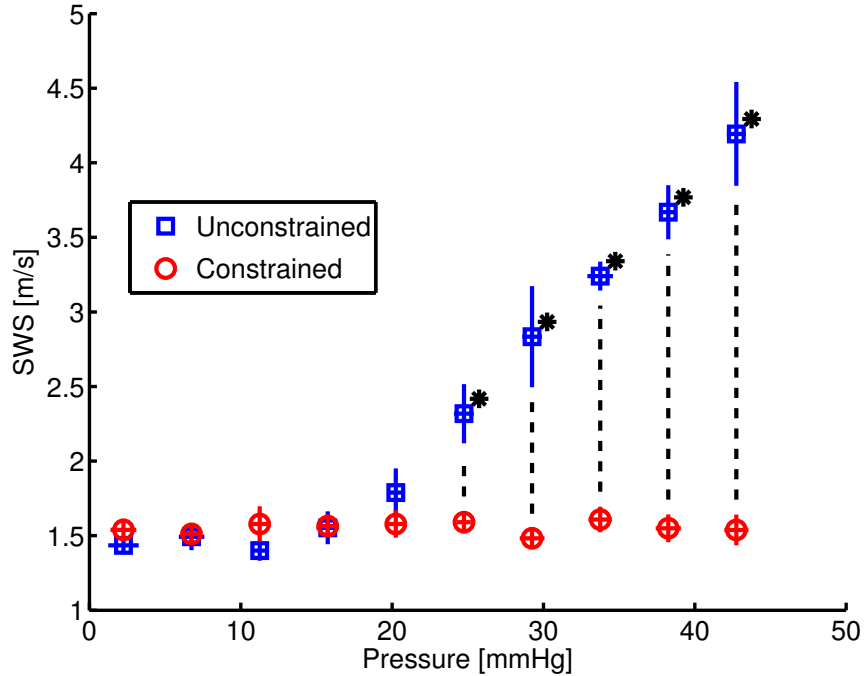


FIGURE 3.5: Comparison between pressurization and SWS for constrained (shown with circles) and unconstrained (shown with boxes) cases from independent measures taken in six ex-vivo canine livers. Standard deviation between the experiments in pressure and SWS are shown as horizontal and vertical errorbars respectively. The * represent groups for which the p -value was less than 0.01.

Ex-vivo livers were also visually observed to expand in the unconstrained case but not in the constrained case. These qualitative observations are shown in a comparison between constrained and unconstrained B-mode screenshots at 45 mmHg in figure 3.7.

3.6 Discussion

HVPG measurement has an important role in the clinical management of hepatic disease. Quantitative liver stiffness measurements have been shown to increase with HVPG [107, 148, 184]. The value of the increase in SWS with pressure is comparable to that observed with fibrosis [192, 126, 158, 199, 58, 161, 5]. Thus, with patients suffering from advanced cirrhosis, it would be difficult to estimate HVPG from SWS

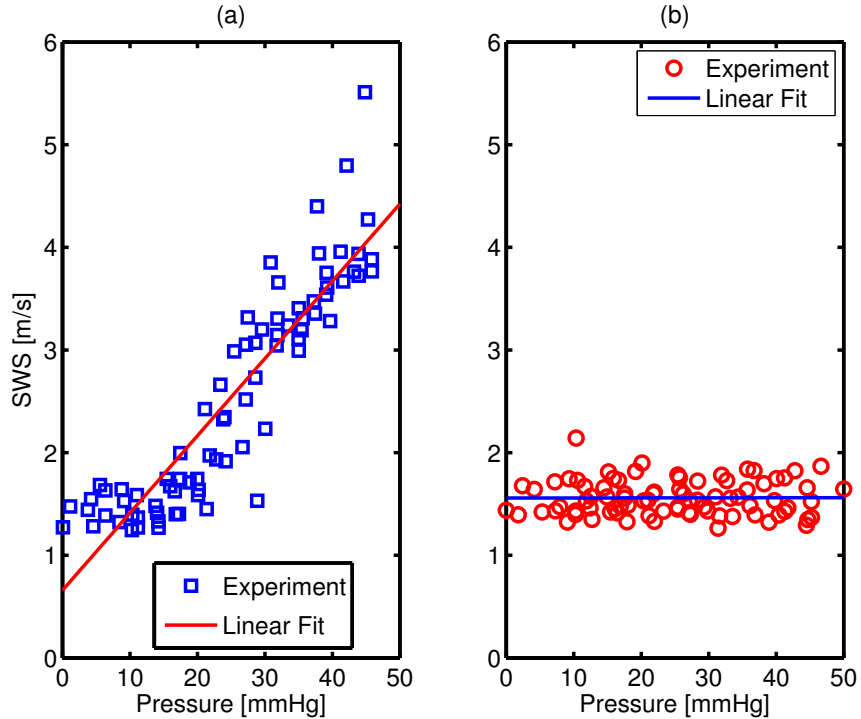


FIGURE 3.6: Multiple linear regression results for the unconstrained (subfigure a) and constrained (subfigure b) SWS estimates across all six experimental animals. The p - values for the hypothesis that SWS does not change with pressure are 0 and .96 for the unconstrained and constrained cases respectively. More quantitative results for the linear fit are shown in table 3.2.

estimates alone. The stiffening observed with advanced stages of fibrosis has been suggested to occur due to increased fibrin and collagen deposition in the tissue [37, 199, 58]. The work described herein investigates a different mechanism that may underlie stiffening observed with pressurization in order to provide the basis for methods that could be used to differentiate the two effects.

In the unconstrained livers at pressure = 2 mmHg and constrained livers across all pressures, the average SWS are 1.4 ± 0.1 m/s and 1.6 ± 0.2 m/s respectively. These were not significantly different groups ($p = 0.63$) and are consistent with the 1-1.7 m/s range reported in surveys of healthy human livers [35, 8, 153]. The similarity between the canine livers described herein and the normal and pressurized results reported in the literature suggest that the strain-dependent mechanisms elucidated

Experimental Condition	y-intercept [m/s]	slope [$\frac{m/s}{mmHg}$]	R^2	$p - value$
Unconstrained	.66	.08	.82	< .01
Constrained	1.56	0.001	2.7E-5	.96

Table 3.2: Linear regression comparing SWS and pressure for constrained and unconstrained conditions across six experiments. The non-zero slope, high R^2 value, and low $p - value$ of the SWS compared with pressure in the unconstrained case indicate a significant correlation between SWS and pressure when the pressurized liver is free to deform. In the constrained case, the high $p - value$ and low R^2 value indicate that there was no correlation between SWS and pressure increase observed when the liver is not free to deform while pressurized.

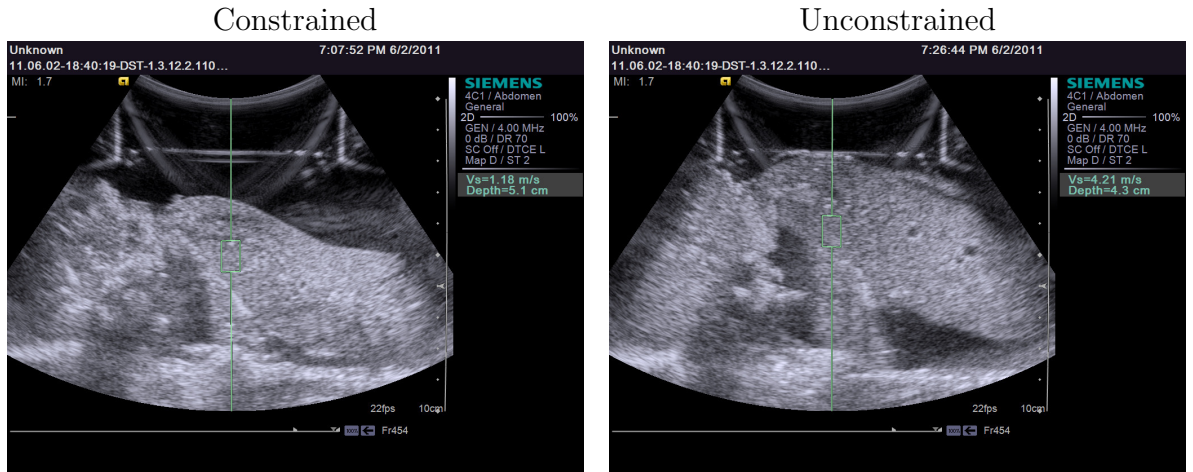


FIGURE 3.7: Screen images from the ultrasound scanner comparing constrained and unconstrained canine livers at 45 mmHg. The green boxes shown above represent the region of interest interrogated using shear wave speed metrics for each case. As shown, the depth of the radiation force excitation varied from 3.5 cm to 5.1 cm in depth from the transducer face. Regions of interest were selected for distance from edges of the liver and relative homogeneity based on B-mode examination. Six shear wave speed datasets were acquired for each pressure at one location of radiation force excitation.

can inform clinical applications of elastography-based technologies. At the highest clinically relevant physiologic pressures of 20-30 mmHg, the SWS estimates have increased from 1.4 m/s to 3 m/s in the unconstrained case as shown in figure 3.5. These results are similar to the ~ 1.6 m/s at 5 mmHg to ~ 4 m/s at 30 mmHg reported in patients with Hepatitis C Virus (HCV)-related chronic liver disease [185]. These results are also comparable to the SWS of 2.5-3.5 m/s reported for fibrosis stage 4

using radiation force-based methods [192, 126]. Because fibrosis is related to an underlying change in collagen content of the tissue [37] while pressurization does not alter fundamental tissue material properties, the strain-based stiffening behavior of pressurized liver observed in this work may provide an opportunity to distinguish fibrotic stiffening from stiffening occurring secondary to pressurization.

The observed increase in volume with increased portal venous pressure (see figure 3.7), suggests that the liver is expanded during hepatic pressurization. This increase in liver size suggests a deformation-dependent increase in shear wave speed that is not consistent geometrically with compression-direction-dependent acoustoelasticity theory. While the underlying theoretical basis of both SWS increases with hepatic pressurization and changes in SWS predicted with acoustoelastic uniaxial compression both rely on hyperelastic material properties, the relationship between the applied stress and corresponding SWS will be different and likely depend on many factors including underlying liver geometry. The liver was qualitatively observed to increase in size with pressurization only in the unconstrained case (see figure 3.7), but it was not possible to evaluate quantitative volume change with this experimental setup. This result supports the hypothesis that increases in liver stiffness with pressurization arise from an increase in underlying strain condition, and can therefore be attributed to tissue nonlinearity. Limitations of this experiment relate to the differences between the experimental setup and *in-vivo* conditions such as the lack of perfusion or active physiologic response, and the difference in temperature between the infusate (~ 23 degrees Celsius) and normal physiology (~ 37 degrees Celsius). The good agreement between experimental results and reports from clinical human literature suggest that these effects are likely to be small. The general increase in SWS errorbar size with increasing SWS noted in figure 3.5 is an expected result related to limitations in temporal and spatial sampling [192].

Table 3.2 shows the results from a linear regression analysis comparing SWS

and increase in pressure for the constrained and unconstrained liver pressurization experiments. There was a high correlation between increasing pressure and SWS when the liver was free to expand ($R^2 = .81$, $p < .01$, slope = $0.08 \frac{m/s}{mmHg}$). In the constrained case, the SWS were not observed to change significantly with pressure ($R^2 < .001$, $p = .96$, slope = $0.001 \frac{m/s}{mmHg}$). These results show a statistically significant relationship between SWS and increasing hepatic pressure only when the liver is free to deform and no relationship when the liver is constrained from expansion. The necessity of deformation to observe increase in SWS suggests that the stiffening effect of pressurization on the liver may be similar to strain-stiffening reported in collagen, kidney, prostate, and other biologic tissues [49, 59, 92]. These similarities may amplify understanding of liver pressurization and provide the basis for using nonlinear strain-stiffening models to quantitate liver pressure *in vivo*.

Hyperelastic behaviors have been previously reported in tissues [49, 92, 59, 179]. Additionally, nonlinear parameter fitting from compression or indentation testing has been studied in liver tissue [24, 34, 81, 62], but *in-situ* testing of nonlinear mechanical properties has not been previously reported. The experiments reported herein provide the basis for exploring nonlinear hyperelastic behavior of the liver *in-situ* or *in-vivo* using radiation force-based methods. The deformation observed with hepatic pressurization may be useful for both elucidating the appropriate mechanical models for liver and modeling the deformation observed with hepatic pressurization. Determining the deformation state of the liver noninvasively using stiffness metrics may provide a noninvasive hepatic pressure measurement tool in the future.

3.7 Conclusions

This work demonstrates that hepatic stiffening with increased pressure requires an underlying tissue deformation indicating that a hyperelastic nonlinear model would be reasonable to adopt for studying shear wave speed increases with hepatic pressur-

ization. Because the mechanism of stiffening from fibrosis stage and pressurization are different, this may provide the basis for distinguishing the two stiffening behaviors, resolving differences between different studies, and for longitudinal tracking of HVPG for prognostic and treatment purposes.

Developing and Validating Methods for Tracking Liver Deformation

4.1 Motivation and Background

Understanding the mechanical properties of the liver relies on tracking the change in strain state of the liver with increasing portal hepatic pressure. In order to accomplish this goal, the deformation of the liver is tracked in two consecutive steps. First, tissue displacement is calculated, and second, the tissue displacements are used to generate estimates of tissue strain [31, 123]. This chapter describes the development and validation of techniques used to calculate tissue displacement using cross correlation of sequential received signals [31, 182, 190], while Chapter 5 discusses the simulations performed to verify strain estimation methods. The imaging system used for the experiments in Chapter 6 and described in Table 4.1 [57] was used. The goals of the work described below were to determine the optimal displacement tracking kernel size to use for hepatic displacement estimation and to quantify the displacement estimation accuracy and precision. These results will inform the data processing algorithms used in the strain simulations described in Chapter 5 and implemented

to determine hepatic strain in the Chapter 6 experiments.

Ultrasonic displacement estimate resolution depends on both window size and displacement magnitude [3, 144]. Three dimensional displacement estimation used for quantifying tissue deformation suffers from the same potential sources of error as the 1-D ultrasonic displacement estimates for radiation force based methods described in Chapter 2.3. The variation of displacement estimates away from the true displacement below a magnitude of $\frac{\lambda}{2}$ is referred to as jitter. Theoretical predictions of the ideal kernel size for strain estimation suggest that there is a direct relationship between displacement estimation jitter and strain estimate variance [31, 180] as shown in Equation 4.1.

$$\sigma_s^2 \geq \frac{2\sigma_\tau^2}{T\Delta t} \quad (4.1)$$

In Equation 4.1, the variance of the strain estimate (σ_s^2) depends on the variance of the time delay estimator (σ_τ^2), the correlation window size (T), and the shift between the echoes (Δt) [180]. This theory predicts that a larger window size will reduce strain estimation variance subject to the effects of decorrelation felt through the displacement estimation jitter value. Decorrelation effects will dominate the effects of displacement error on strain variance in the region of strains larger than 2% [123]. Various methods have been proposed in the literature to balance the decreasing strain variance effect of a larger window size with the increasing strain-derived decorrelation experienced during the initial correlation-based displacement estimation due to that large window size. Axial displacement estimation kernels in cardiac imaging have been used over a range of 1.8mm to 6.9mm [193, 96, 91]. In addition to the variation in window size, the optimal number of dimensions used in the cross correlation kernel and search region are subject to debate. In cardiac strain methods used vary from use of a 1-D axial kernel in a 2-D search region

[90, 96], to 2-D square kernels [91] to a 3-D kernel and search region [26]. While increasing the lateral and elevational sizes of the kernel beyond one dimension can lead to reduced resolution in those additional dimensions [75], they can also lead to improved displacement estimation accuracy [75, 140, 93].

The goal of this study was to choose a displacement estimation kernel size that would minimize displacement spatial variability under conditions of bulk motion, in which no underlying spatial variability in displacement is expected. The results achieved suggest that axial displacement estimation is much more accurate than elevational or lateral displacement estimation accuracy, due to the phase information and broad bandwidth that is present exclusively in the axial dimension [101, 183].

4.2 Methods

In order to analyze the methods proposed for determining hepatic displacement, an experimental setup was used in which tissue-mimicking phantoms [73] were submerged in a water bath 4 cm from the surface of the transducer. The transducer was held with a motorized translation stage (model NM 3000, 0.1 μm precision, Newport Corporation, Irvine, CA). Pure axial, lateral, and elevational motion were generated in 25 μm increments from 25-125 μm in the axial dimension and 25-300 μm in the elevational and lateral dimensions.

Table 4.1: Parameters Used for Displacement Tracking

Parameter	Value
Ultrasound Scanner	SC-2000
Probe	4z1c
F_c	2.8 MHz
Transmit Focus	8cm
Imaging Depth	5-7cm

The following experiments used the SC-2000TM scanner with the 4z1c matrix array transducer (Siemens Ultrasound, Mountain View, CA) [57]. The ultrasonic

parameters of this system are described in Table 4.1. Standard B-mode ultrasound images were acquired and the autocorrelation of the speckle was calculated at a depth of 5 cm in order to quantify system resolution. The full-width-half-max of the speckle autocorrelation describes the system resolution in 3 dimensions [189]. This information was used to predict optimal speckle tracking parameters. These results are shown in Figure 4.1.

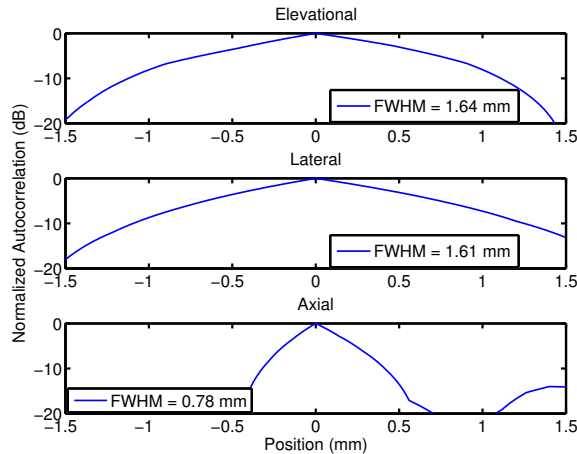


FIGURE 4.1: Three-dimensional normalized autocorrelation of speckle for the imaging parameters used.

Figure 4.1 suggests that axial kernels larger than 0.78mm (the FWHM of the autocorrelation in the axial dimension) would be necessary to adequately sample the data and achieve accurate displacement estimates without peak-hopping artifacts. The lateral and elevational speckle size (as described by the FWHM) are 1.61 and 1.64 mm respectively, significantly larger than that observed in the axial dimension. In order to characterize the behavior of the liver during pressurization, the optimal displacement estimation strategy using the available transducer and ultrasound parameters was explored via experiments using known displacements generated by a mechanical translation stage.

The results shown in Figure 4.1 describe the speckle size in the elevation and lateral dimensions as 1.61 and 1.64 mm. In the case of translation stage bulk motion,

which will be explored in this chapter, we would expect that larger displacement estimate kernel sizes in all three dimensions would lead to more accurate and precise displacement measurement. However, Equation 4.1 reveals that larger displacement estimation kernels in the context of tissue strain (rather than bulk tissue displacement) will lead to strain decorrelation and larger strain estimation errors. This effect has been shown to be much worse in the lateral and elevation dimensions than in the axial dimension [26]. Thus, a balance of large enough displacement estimate kernel size to generate accurate measurement with a small enough kernel to reduce strain decorrelation artifacts is necessary. Based on a review of the literature on multi-dimensional strain imaging, [26, 90, 91, 193, 93], a large axial kernel size with respect to the wavelength (approximately 4λ) and small lateral and elevational kernels with respect to the resolution width (0.4 and 0.6 mm) were tested.

Displacement Estimation

Because hepatic expansion is expected to occur in three dimensions, 3-D displacement estimation techniques were utilized. This is expected to reduce displacement estimation jitter as well as increase accuracy in cases where multiple dimensions of displacement are observed [75, 140, 93]. Displacements were estimated using a 3-D cross correlation approach described in [26]. Phase-sensitive normalized cross correlation with grid slopes algorithm sub-sample estimation was used [48, 194, 65]. A 0.9 correlation coefficient cutoff was implemented for the displacement estimates. The kernel and window sizes chosen correspond to the displacement estimation kernels in cardiac imaging reported in the literature. Particularly, the specific axial kernel sizes used have been observed over a range of 1.8 mm to 6.9 mm [193, 96, 91].

Translation Stage Experiments

Bulk motion in the axial, lateral, and elevational dimensions was implemented using a translation stage. In one experiment, the translation stage was moved at fixed increments of 25-120 μm in the axial dimension and 25-300 μm in the lateral and elevational dimensions between 3-D B-mode volume acquisitions. These datasets were used to characterize the displacement estimation accuracy and spatial variation in each of the 3 dimensions. In addition, experiments were performed to characterize the displacement estimate variability with changes in underlying speckle by generating 10 datasets with the same volume to volume displacement of 110 μm . The variability in the same location in the B-mode volume but with different underlying speckle was used to generate an estimate of displacement estimate jitter (σ_τ^2 in Equation 4.1).

4.3 Results and Discussion

Translation stage experiments under conditions of bulk motion were performed to determine the optimal kernel size for displacement estimation using this imaging system. Various axial kernel sizes were tested on pure axial bulk motion while keeping the lateral and elevational kernels to a constant size (0.45x0.50 mm in the lateral and elevational dimensions respectively). Results are shown in Figure 4.2 and suggest that axial kernel sizes above 0.65mm can accurately estimate displacements from 0-0.12mm.

Because displacement estimation jitter and bias appeared to decrease as a function of increasing axial displacement estimation kernel size, an axial kernel size of 2.88 mm was chosen (which corresponds to slightly larger than 4λ of the imaging system) for further examination. Analysis was then performed to determine the optimal elevational and lateral kernel sizes as a function of displacement estimation

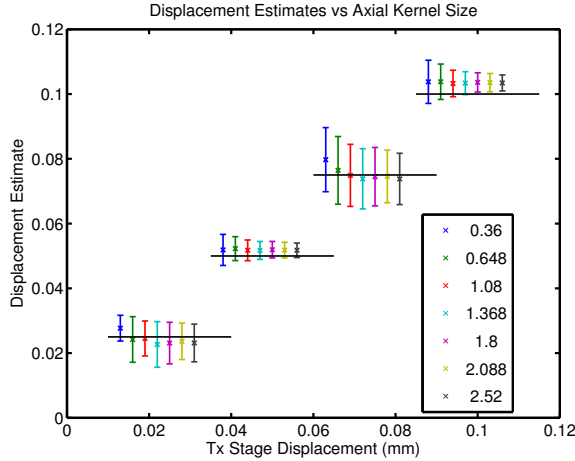


FIGURE 4.2: Displacement estimates from 0.02-0.12 mm as a function of 7 different axial kernel sizes (different colors, shown in mm). Errorbars show the spatial standard deviation of the displacement estimate over a 2x1.1x1.1 cm volume from 5-7 cm in depth. Lateral and elevational kernel sizes were kept constant at 0.40 and 0.45 mm respectively for the data shown.

accuracy, spatial variation, and bias.

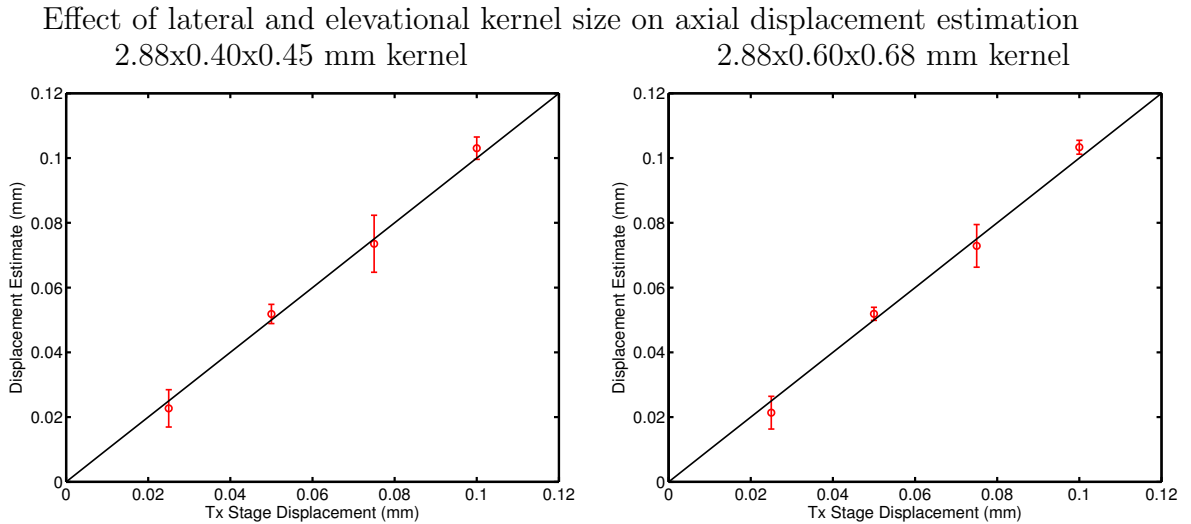


FIGURE 4.3: Two different lateral and elevational kernel sizes were tested on pure axial motion using the translation stage. A 0.9 correlation coefficient cutoff was used for the displacement estimation. A line with unity slope is shown in black. The R^2 of the displacement estimates to this unity line is 0.99 for the smaller kernel (left) and 0.99 for the larger kernel (right).

The lateral and elevational kernels tested in Figure 4.3 yielded accurate mean

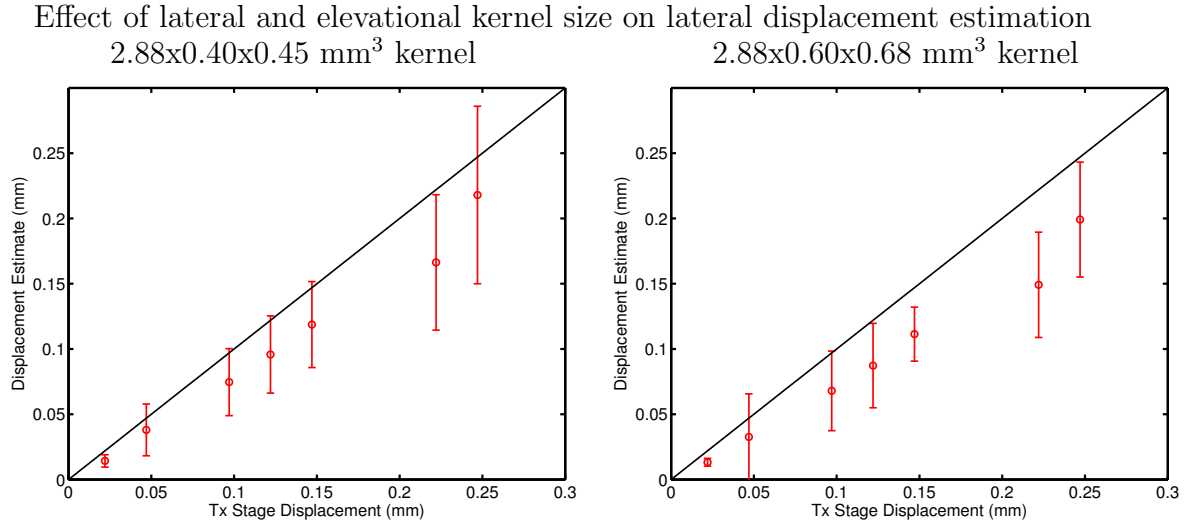


FIGURE 4.4: Two different lateral and elevational kernel sizes were tested on pure lateral motion using the translation stage. A 0.9 correlation coefficient cutoff was used for the displacement estimation. A line with unity slope is shown in black. The R^2 of the displacement estimates to this unity line is 0.88 for the smaller kernel (left) and 0.93 for the larger kernel (right).

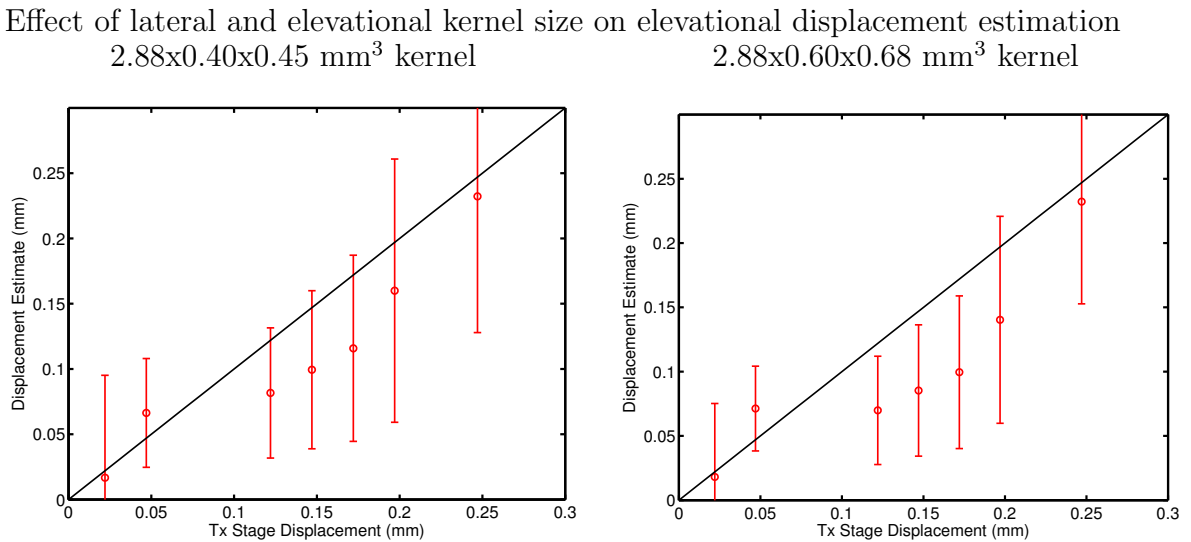


FIGURE 4.5: Two different lateral and elevational kernel sizes were tested on pure elevational motion using the translation stage. A 0.9 correlation coefficient cutoff was used for the displacement estimation. A line with unity slope is shown in black. The R^2 of the displacement estimates to this unity line is 0.48 for the smaller kernel (left) and 0.50 for the larger kernel (right).

displacement estimates to within $15 \mu\text{m}$ across all axial displacements, whereas biases as large as $100 \mu\text{m}$ in magnitude were observed in the elevation (Figure 4.5) and lateral dimensions (Figure 4.4) for large bulk displacements. No significant change in displacement estimation bias was observed with increasing kernel size. These results as a function of lateral and elevational kernel size are shown in Figure 4.6.

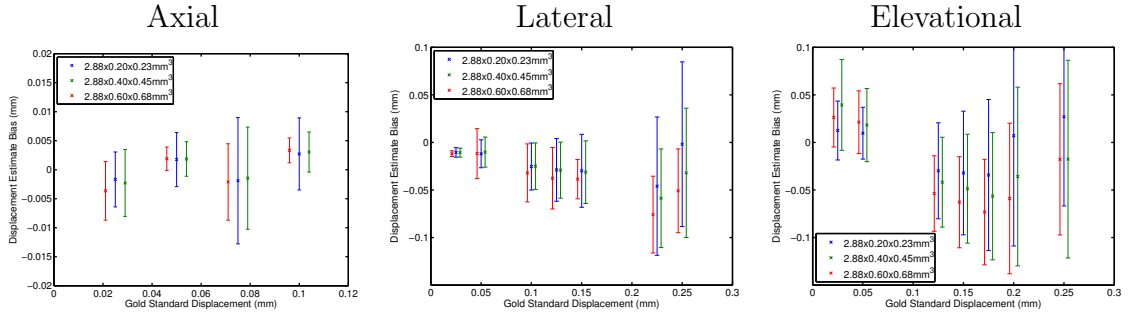


FIGURE 4.6: Effect of kernel size on bulk displacement estimate bias. The axes are changed between the axial plot and the lateral and elevation plots to provide information about the slight differences observed in the kernel sizes tested. Three kernel sizes were tested on pure axial, elevational, and lateral motion using the translation stage. A 0.9 correlation coefficient cutoff was used for the displacement estimation. The average bias for each displacement estimation volume across different kernel sizes is shown above. The bias for each displacement magnitude does appear to increase in magnitude in the lateral and elevational dimensions with kernel size, but the results are not statistically distinguishable from each other.

Strain estimation relies on the assumption that all displacement estimates in the same axial, elevation, or lateral location are the same. Thus, measurement of spatial variation of displacement in a volume when we know all displacement estimates should be identical was also examined in order to determine the optimal kernel size for strain estimation. These results are shown in Figure 4.7. Spatial variation of displacement estimate is observed to decrease slightly, though the differences were not statistically significant, as a function of increasing elevation and lateral kernel size. In the case of three different elevational and lateral kernel sizes tested with a constant axial kernel size, displacement estimation bias and average correlation coefficient magnitude did not change with increasing kernel size. These results are

Kernel Size (mm ³)	Jitter with constant 110 μm axial motion between volumes	Jitter in the liver (no motion)
2.88x0.20x0.23	$3.23 \pm 3.94\mu\text{m}$	$1.25 \pm 0.75\mu\text{m}$
2.88x0.40x0.45	$1.92 \pm 2.21\mu\text{m}$	$1.15 \pm 0.72\mu\text{m}$
2.88x0.60x0.68	$1.28 \pm 1.23\mu\text{m}$	$1.04 \pm 0.68\mu\text{m}$

Table 4.2: Comparison between axial displacement estimation jitter in hepatic volume comparisons without motion and those with a constant inter-volume displacement.

consistent with the expectation for a bulk motion case, but average decorrelation between received echoes would be expected to increase with increasing kernel size in the case of strain due to increasing decorrelation within the kernel itself [99].

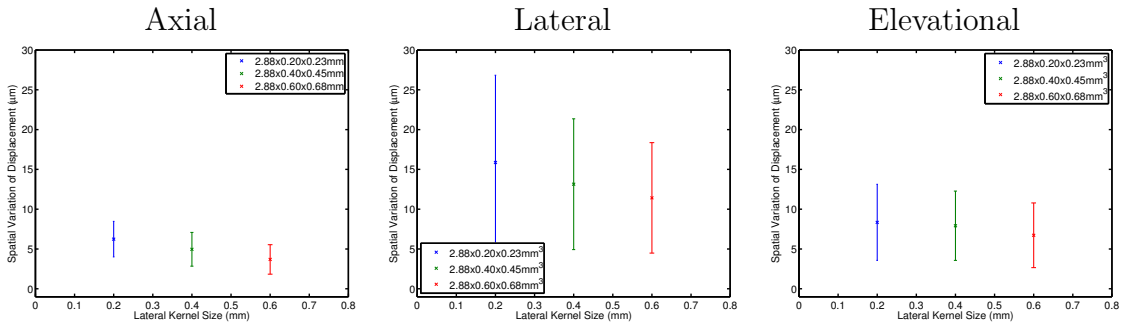


FIGURE 4.7: Effect of kernel size on displacement estimate spatial variability for bulk motion. Three kernel sizes were tested on pure axial, elevational, and lateral motion using the translation stage. A 0.9 correlation coefficient cutoff was used for the displacement estimation. The spatial variation of each displacement estimate for the corresponding translation stage motion direction is shown above and appears to decrease with increasing elevation and lateral kernel size.

The displacement estimation jitter was also calculated in the case of multiple sequential volumes with known 110 μm displacement between each subsequent volume as compared with displacement estimates in the case of no motion. These results are shown in Table 4.2.

The expected jitter for all three dimensions of bulk motion is shown in Table 4.3. There was a significant increase in lateral displacement estimation jitter as compared with elevation estimation jitter in the case of 100 μm constant motion in subsequent

Axial Jitter	Lateral Jitter	Elevation Jitter
$1.28 \pm 1.23\mu m$	$15.59 \pm 6.9\mu m$	$5.08 \pm 1.87\mu m$

Table 4.3: Three dimensional displacement estimation jitter calculated for constant velocity translation stage motion.

volumes. This relationship was not predicted by the previous studies of displacement estimate accuracy or spatial variation, but could have a detrimental effect on the potential for three dimensional strain estimation in the liver experiments.

Since strain estimation variance is dependent on displacement estimation jitter magnitude (σ_7^2 in Equation 4.1), the displacement estimation kernel size was chosen to decrease the spatial variability and jitter of displacement estimate in the context of bulk motion limited by the kernel sizes tested under the expectation that displacement estimation jitter will dramatically increase in the context of tissue strain [26]. This kernel size of 2.88x0.60x0.68 mm was chosen for the experimental efforts to characterize hepatic deformation with increasing hepatic pressure.

4.4 Conclusions

Experiments were performed to validate the proposed methods for measuring hepatic tissue displacement with increasing pressure. A 3-dimensional displacement estimation kernel of 2.88x0.60x0.68 mm³ was selected to minimize spatial variability and precision in the displacement estimate that would then be input to the strain calculation algorithm. Displacement estimates in the lateral and elevation dimension were significantly worse than the axial estimates by metrics of displacement estimate bias and jitter. For displacements less than 100 μm , lateral and elevational bulk displacements were able to be measured to within 50 μm and within 15 μm in the axial dimension.

Establishing methods used to calculate hepatic strain

5.1 Motivation and Background

Understanding the mechanical properties of the liver as they relate to the effect of hepatic pressurization relies on tracking the change in strain state of the liver with increasing portal hepatic pressure. While Chapter 4 discussed the methods explored to accurately calculate displacements in the case of bulk motion, it was also necessary to verify the strain estimation methods used. Accurate description of hepatic deformation during pressurization will form the basis for conclusions that can be drawn about hepatic elasticity in the thesis work described herein. Simulations were performed to characterize the accuracy of the ultrasonic imaging system used as well as the post-processing algorithms for the purpose of strain estimation.

Strain can be calculated by differences between time delayed received echoes [31, 182, 190]. In our case, the delays between signals were calculated in the form of 3-D displacements using cross correlation, as described in Chapter 4. These displacements were then input to the strain estimation algorithms to generate an

estimate of the strain state of the deformed material being simulated.

The relationship between tissue displacement, deformation, and strain underly our ability to deduce mechanical properties of tissue using ultrasound. We can begin to explore this by looking at a model of a simple compression state in a cartesian coordinate system with pure compression in the axial (x_1) direction. The deformation state is shown below in which the capital X (e.g. X_i) denotes the undeformed state while the lowercase x (e.g. x_i) denotes the deformed state.

$$\begin{aligned}x_1 &= \lambda X_1 \\x_2 &= \frac{1}{\sqrt{\lambda}} X_2 \\x_3 &= \frac{1}{\sqrt{\lambda}} X_3\end{aligned}$$

from which we can find the deformation gradient:

$$F = \begin{pmatrix} \lambda & 0 & 0 \\ 0 & \frac{1}{\sqrt{\lambda}} & 0 \\ 0 & 0 & \frac{1}{\sqrt{\lambda}} \end{pmatrix} \quad (5.1)$$

The relationship between the deformations in the x_1 dimension as compared with x_2 and x_3 are dictated by the assumption of incompressibility (which requires that $F_{11}F_{22}F_{33} = 1$). Most biological tissues can be accurately modeled as being incompressible [2, 151, 27, 177, 175, 111]. The strain can be calculated for this general deformation state as explained below. The incompressibility condition requires a particular relationship between the displacements imposed in the axial (x_1) dimension as compared with the other two dimensions in that without adding or subtracting volume, a compression in one dimension requires equal expansion in the other two dimensions. The displacement (u_i) will be equal to the difference between the deformed state and the undeformed state. The derivative of the deformed state with

respect to the undeformed state in the axial dimension is defined as λ below because it also represents the stretch of the deformed material.

$$\begin{aligned}
 u_1 &= x_1 - X_1 = \lambda X_1 - X_1 = (\lambda - 1)X_1 \\
 u_2 &= x_2 - X_2 = \frac{1}{\sqrt{\lambda}}X_2 - X_2 = \left(\frac{1}{\sqrt{\lambda}} - 1\right)X_2 \\
 u_3 &= x_3 - X_3 = \frac{1}{\sqrt{\lambda}}X_3 - X_3 = \left(\frac{1}{\sqrt{\lambda}} - 1\right)X_3
 \end{aligned}$$

The Lagrangian Strain Tensor (E_{KL}) is defined in Equation 5.2 using the spatial derivatives of the displacement.

$$E_{KL} = \frac{1}{2} \left(\frac{\partial u_K}{\partial X_L} + \frac{\partial u_L}{\partial X_K} + \frac{\partial u_M}{\partial X_K} \frac{\partial u_M}{\partial X_L} \right) \quad (5.2)$$

Thus, for the deformation state described by simple compression above, the strain tensor will be:

$$E = \begin{pmatrix} \lambda - 1 & 0 & 0 \\ 0 & \frac{1}{\sqrt{\lambda}} - 1 & 0 \\ 0 & 0 & \frac{1}{\sqrt{\lambda}} - 1 \end{pmatrix} \quad (5.3)$$

Relating these quantities to more standard notation, the change in height in the axial dimension (i.e. the change in “length” of the material: $\frac{\Delta l}{l}$) equals λ , which equals $1 + E_{11}$ in the deformation state described. Since there are no shear strains induced during compression (the off-diagonal zeros in Equation 5.3), the major quantities needed to be calculated to generate an estimate of the strains are the derivatives $\frac{\partial u_i}{\partial X_i}$. In the case of static and constant strain, we expect these derivative values to be the same at all positions, which implies that, for example, the axial displacement will be expected to be the same at all elevation and lateral positions that correspond to a specific axial position. This development of predictions about

an incompressible material under uniaxial deformation informs the generation of simulated materials for testing strain estimation algorithms. In the case of bulk motion this would also hold true, but the derivative of the axial displacement as a function of position would be zero.

The goal of this work was to validate methods for interrogating deformation of the liver as portal venous pressure is increased. Accurate estimates of hepatic strain will provide the basis for future development of tissue mechanical models. Using the underlying theory of incompressible materials under uniaxial compression, strain estimation methods were tested against finite element simulations. The strain calculation method of linear regression over a large strain estimation kernel was compared with finite element strains using scatterer motion and tracked 3-D displacements of simulated deformation.

5.2 Methods

Mechanical Simulations In order to test the strain estimation algorithm used to characterize hepatic expansion, four compressive strains between 0.08% and 0.8% were simulated using LS-DYNATM(LSTC, Livermore, CA). An implicit solver method [77] was used and the compressive strain was achieved through axial compression of the top nodes while fixing the bottom boundary of the phantom from any movement. The phantom was simulated as an isotropic nearly-incompressible ($\nu = 0.499$) solid with a Young’s Modulus of 4kPa and square elements. Details of the simulated phantom size are shown in Table 5.1.

Table 5.1: LS-DYNATMparameters for simulation of tissue compression.

Parameter	Value
Axial Extent	5 cm
Lateral Extent	1.5 cm
Elevation Extent	1.5 cm
Element Size	1 mm ³

Post-processing of the simulation results was performed using LS-PREPOSTTM and MATLABTM (Mathworks, Natick, MA). Methods similar to those described in [131, 130] were used to generate scatterer fields corresponding to the simulated strains. A scatterer density of 55,000 scatterers per cm^3 was used with 8 independent scatterer fields generated per strain simulation. For each scatterer field, the positions of the scatterers were randomly determined, but amplitudes were held constant and not varied. The number of scatterers was chosen as the minimum required to maintain a signal to noise ratio in the tracked simulated detected data greater than 1.91.

Strain Estimation The strain estimation algorithm of fitting a line using least-squares estimation on the displacement versus position was utilized [123]. In order to test this, the displacement of the imposed scatterer fields was calculated prior to simulation of the ultrasound motion tracking. Scatterers were limited to 5-7 cm away from the transducer in the axial dimension. These displaced scatterers' movements were fit to a linear regression over a 2 cm strain estimation kernel. The slope of the displacement vs position was calculated to generate a strain estimate.

Radiofrequency data in 3-D was simulated in Field II by tracking of the 8 scatterer realizations with the 4z1cTM (Siemens Ultrasound, Mountain View, CA) matrix array transducer using the parameters that correspond to the imaging case used in the hepatic pressurization setup [130] (see Table 5.2). At 6 cm depth, the region of interest interrogated by simulated tracking beams was 17mm x 15mm x 20mm in the lateral, elevation, and axial planes respectively. Beams were spaced 0.8mm apart in the lateral dimension and 1.0 mm apart in the elevation dimension (as compared to 0.798 mm and 0.99 mm respectively for the imaging system). The transmit $F/\#$ was 2 in both elevation and lateral with dynamic receive focusing applied. The center frequency of the probe was simulated at 2.5 MHz with 100 MHz sampling.

Once the RF-data was simulated, post-deformation displacements were estimated

Table 5.2: Comparison of Simulation and Experimental Parameters

Parameter	Simulated Value	Experimental Value
Ultrasound Scanner		SC-2000
Probe		4z1c
Center Frequency	2.5 MHz	2.8 MHz
Focal Depth	0.08 m	0.08 m
Lateral Beam Spacing at 6 cm depth	0.8 mm	0.81 mm
Elevation Beam Spacing at 6 cm depth	1.0 mm	0.99 mm
Displacement Estimation Kernel	2.3x0.4x0.42 mm	2.88x0.60x0.68 mm

on demodulated IQ data ($f_{dem} = 2.5$ MHz) using a 3-D cross correlation algorithm with a grid-slopes sub-sample estimator [26]. The 3-D kernel used was 0.4mm x 0.42mm x 2.3mm and the search region was 0.8mm x 0.9mm x 4.6mm in the lateral, elevation, and axial dimensions respectively, as calculated at 5cm depth. The exact method used for displacement estimation as well as the verification of displacement estimation accuracy for the bulk motion of scatterers was described in more detail in Chapter 4.

Since the strain is expected to be constant through the region of interest, bulk static strains were approximated as a linear regression to the slope of the displacement estimate as a function of position [84, 175, 102]. Using a linear regression will significantly decrease the effect of noise in the displacement estimate on the final strain calculation as compared with a gradient operator [84]. In the case of constant strain, strain variance can be reduced and SNR can be increased by lengthening the strain estimation window and increasing the number of displacement estimates used for the strain estimate [84]. This approach was evolved from methods to estimate local strains using an approximation of the derivative from local time shift estimates from received echoes [124]. In cases where the strain does not vary spatially, large spatial shifts between measured displacement positions are shown to increase the strain estimation SNR with an associated decrease in resolution [9, 167, 144].

5.3 Results and Discussion

Axial Strain Estimation

The outputs from LS-DYNATM were used as the gold standard in this simulation work as they formed the basis of scatterer field placement and motion for the ultrasonic tracking. The displacement and strain output from the finite element simulations are shown in Figures 5.1 and 5.2. The imposed displacement gradient in each of the strain cases can be clearly observed in Figure 5.1. Boundary-related artifacts on the simulation strain state at the bottom of the solid model can clearly be seen in Figure 5.2 for all strain cases. The region of interest is far from this boundary, which should mitigate the effects of having a fixed bottom boundary (rather than one which is free to move in the elevation-lateral plane). The gold standard strain estimate upon which the strain estimate algorithm is tested is the mean of finite element calculation in the simulation. Thus, the effect of a fixed bottom boundary should be controlled for as it is included in the comparison.

The line fitting methods were verified by fitting a linear regression to the individual scatterer displacements and compared with the average finite element strain calculation in the region of interest. Eight different scatterer realizations were simulated for each strain state. Examples of the scatterer displacements (with the mean displacement subtracted so all displacements are centered about zero) and the linear regression used to calculate strain for one speckle realization are shown in Figure 5.3. Good agreement can be observed between the strain estimate linear fit and the scatterer displacements.

The axial strain estimates from LS-DYNATM are compared with the linear regression to the scatterer displacements for the three different dimensions in Figure 5.4. For the 8 speckle realizations and each of the four deformation states tested, the axial strain estimates based on linear regression of scatterer displacement and

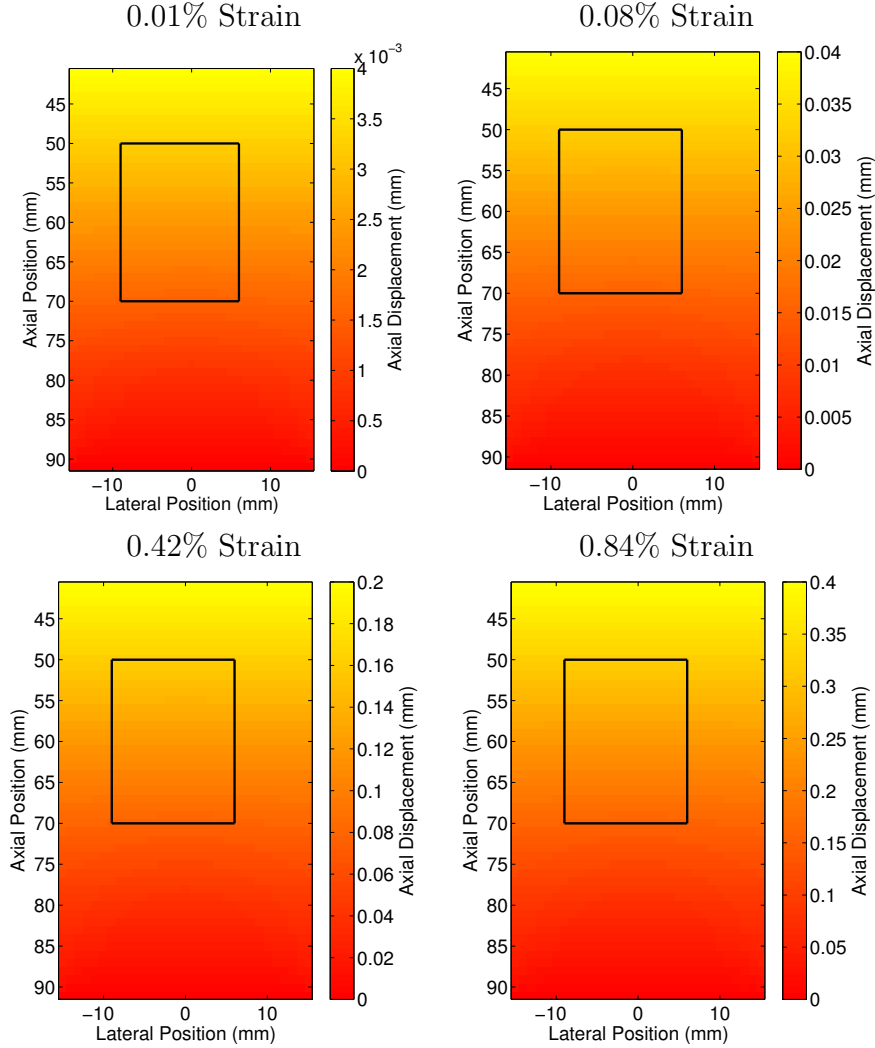


FIGURE 5.1: Axial displacement calculation from finite element simulations using LS-DYNATM. The region of interest interrogated by the simulated transducer is shown in black. The gradient of displacement can clearly be seen in the top row of each image (the color limits of the images vary with different strains).

position agreed very well with the finite element simulated strains. The scatterer input to Field II for simulation of the 3-D tracking are deforming as expected and the proposed strain estimation algorithm is generating accurate estimates of strain using a linear regression of displacement estimates and position of the scatterers. The average error of the strain fit to the scatterer positions as compared with the finite element strain output was $2.5\% \pm 0.4\%$.

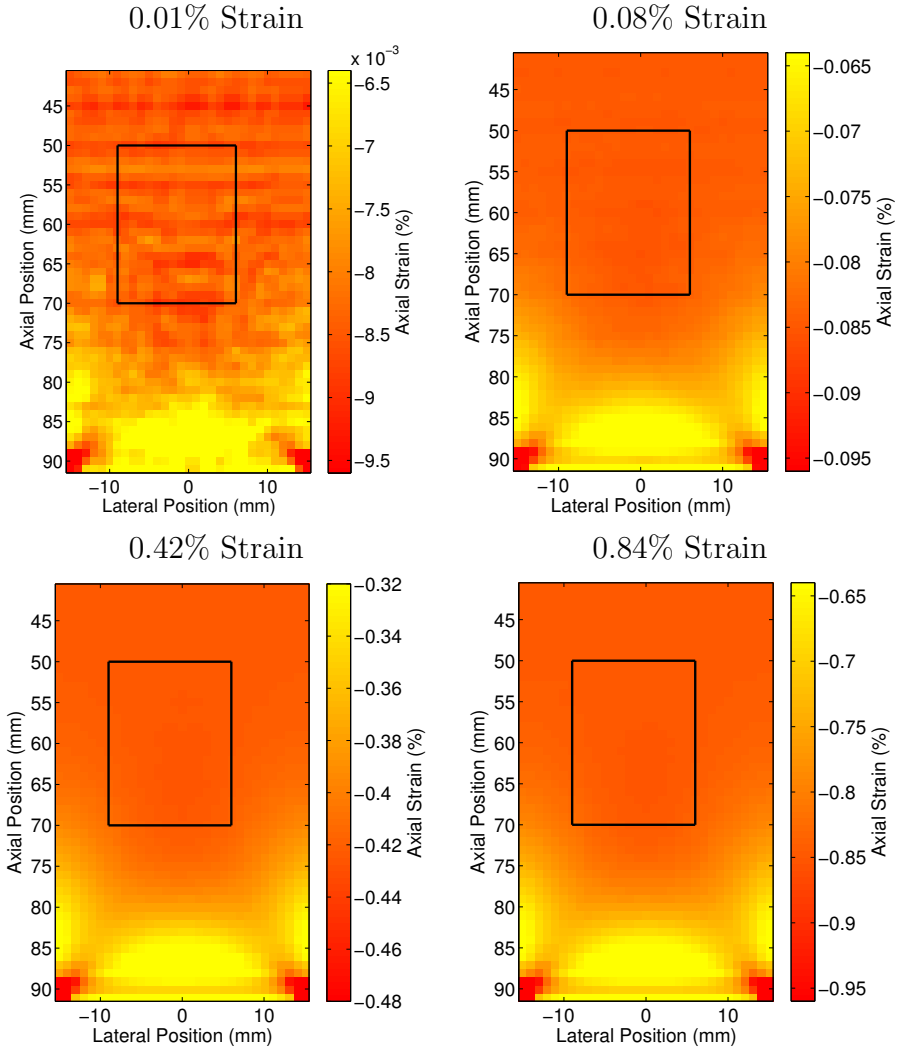


FIGURE 5.2: Axial strain calculated using LS-DYNATM finite element simulations. The region of interest interrogated by the simulated transducer is shown in black.

In addition to testing the strain estimation algorithm on simulated scatterer locations, the ultrasonic images of the scatterers were generated using Field II and the resulting RF-data was used for 3-D displacement estimation using the algorithms described in Chapter 4. These 3-D displacements were used to generate estimates of strain in 3 dimensions using the algorithms validated by linear regression to scatterer position. The linear regressions as compared with the axial displacement versus axial position (with the mean displacement subtracted) are shown for all four strain

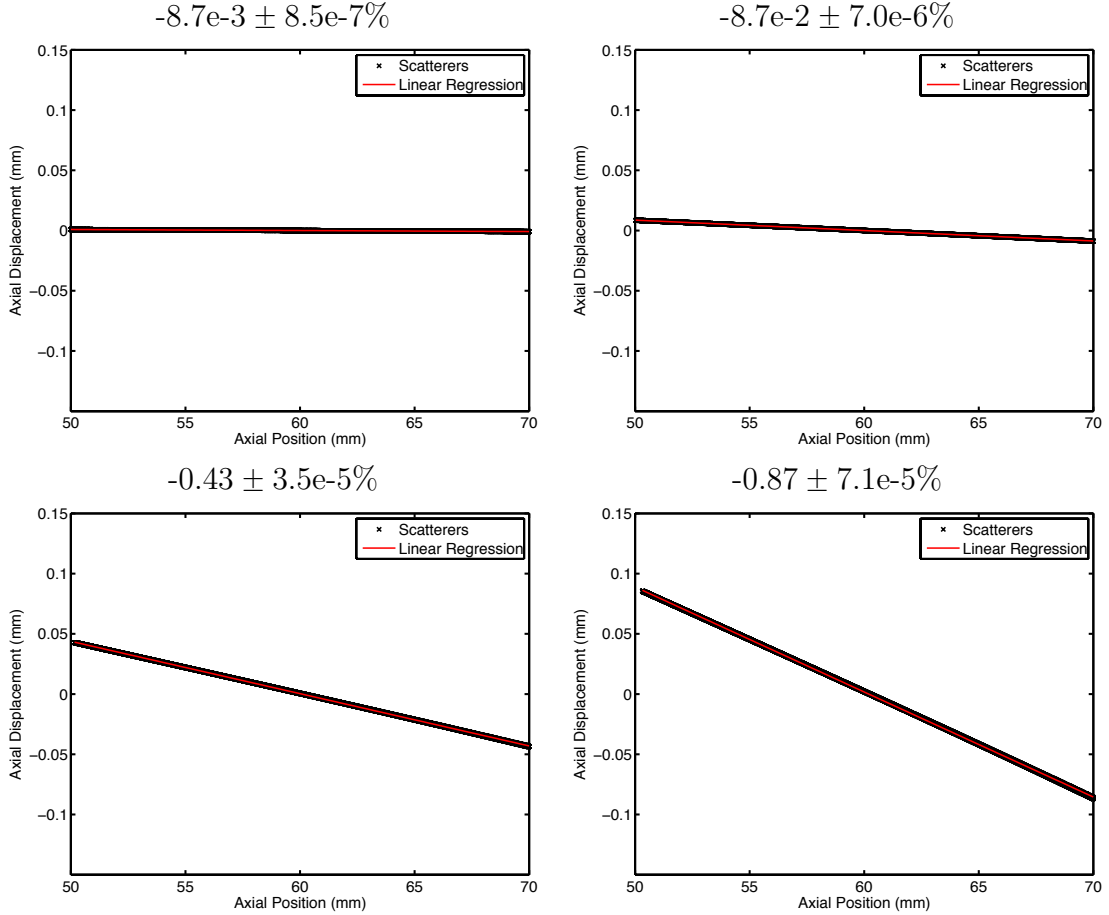


FIGURE 5.3: Examples of the line fit used to generate axial strain estimates for the four deformation cases using the scatterer positions generated from LS-DYNATM simulation output. The scatterer displacements are shown in black and the line fit is shown in red. In this case, the 95% confidence interval is given rather than a standard deviation because there is only one measurement.

cases in Figure 5.5. The raw displacements are plotted as a function of position for all the strain cases with the scatterer displacements overlaid in Figure 5.7 and also illustrates why the fourth plot of linear fit to the displacement estimates was counterintuitive for the largest strain case tested instead of the expected negative result.

Figure 5.7 shows the axial displacement estimates as a function of axial position for all four strain states simulated in this work. For the two smaller strain states simulated, there is good agreement between the scatterer displacement and the dis-

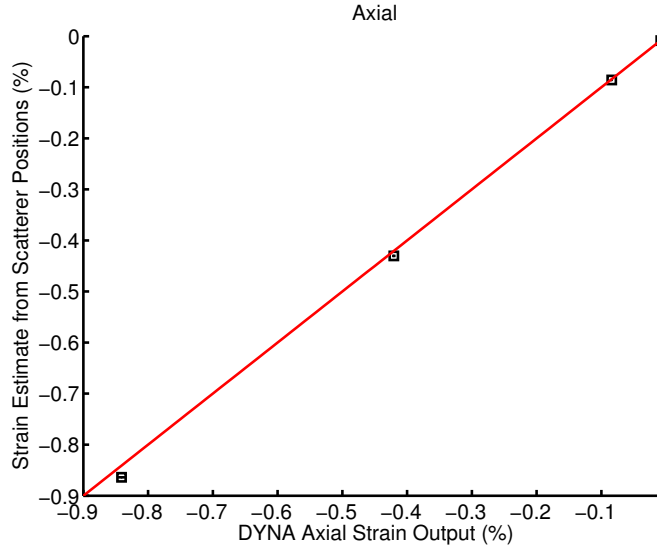


FIGURE 5.4: Axial strain estimate based on linear regression of scatterer displacement versus position as compared with the average of the finite element simulation strain estimate in the region of interest. Errorbars shown which appear to be generally smaller than the marker size are the standard deviation of eight scatterer realizations (for the scatterers) or the strain estimate in the region of interest (for the simulations).

placements estimated based on the tracked simulated ultrasound signal. For the two larger strain states, it appears that the strain simulation implementation used in this work, for which the top boundary of the simulated material is being compressed, is leading to large bulk displacements at the top of the region of interest (at 50 mm in depth) in order to achieve the desired applied strain. In addition, there appears to be a slight flattening of the displacement estimate at the surface, which may be a result of the fact that the simulated scatterer position begins at 50 mm exactly. This lack of shallow scatterers may be affecting the displacement estimates right at the edge of the scatterer field, but is not expected in the experimental datasets for which the region of interest begins below the liver capsule. Figure 5.6 suggests that this slight flattening of the displacement estimates is a result of the low RF-signal amplitude at 5cm in depth away from the transducer.

For the -0.84% strain case, the gradient of displacements across the 2 cm strain

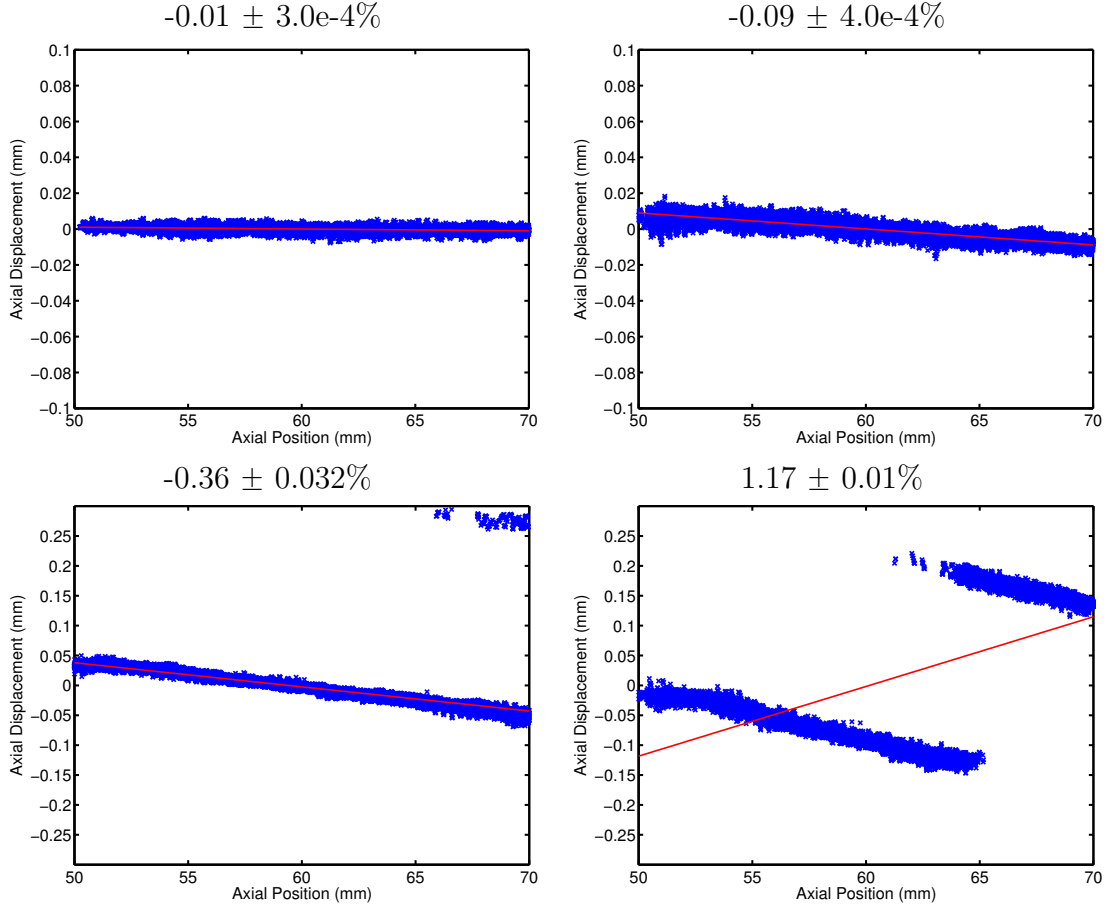


FIGURE 5.5: Example simulated and tracked axial displacement versus position using 3-D tracking for the four simulated strain cases. The calculated strain for each of the datasets are shown with intervals quoted as the 95% confidence interval of the line fit and the mean displacement is subtracted so all the displacements are centered around zero. The axes for the top row are smaller than for the bottom row in order to show all displacement estimates in the four cases. The bottom right plot shows the erroneous positive fit achieved for the largest strain case (strain expected -0.88% strain as compared to the estimate of 1.17%).

estimation kernel is 0.15 mm while the offset of the displacements is up to 0.3 mm. We hypothesize that this large bulk displacement offset is leading to peak hopping of the displacement estimates as the discontinuities correspond to $\frac{\lambda}{2}$ and λ and an implementation of displacement estimation with a larger search region did not mitigate this effect. These aberrant displacements were observed across all lateral and elevational positions for the axial positions affected. The dependence of the incorrect

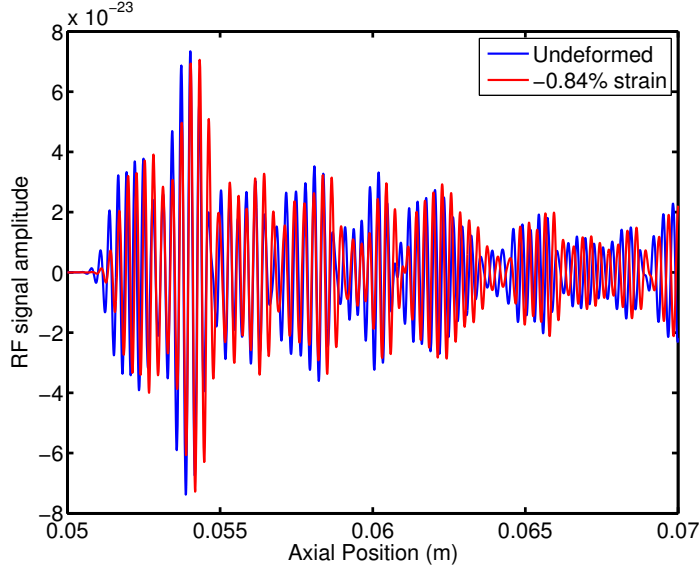


FIGURE 5.6: One axial A-line acquired from simulated deformed scatterers with imposed 0.84% compressive strain. From 0.05 to 0.052 m in depth there is no signal, which is an artifact of the simulation approach in which scatterers were populated starting at 0.05 m. This artifact may lead to bias in the strain and displacement estimates but is not expected in vivo. The addition of many scatterers closer to the transducer could reduce the effect of this error in the region of interest, but at the expense of much larger datasets and longer run times for the simulation.

(as compared with underlying scatterer displacement) displacement estimates on $\frac{\lambda}{2}$ can be seen in Figure 5.8 and is repeated for the 8 scatter realizations in 0.42% and 0.84% strain cases tested.

Figure 5.8 shows that the relationship between the correct underlying scatterer displacements and the displacement estimate is related to $\lambda/2$ and λ . Using the displacement estimation approach described, it is the lag at the peak of the correlation function between the search region imaging data from the reference configuration as compared to the kernel from the deformed configuration that corresponds to the displacement estimate [195]. Utilization of a phased array transducer to track high underlying displacements can lead to a peak of the correlation function used to calculate displacements that is significantly less than unity. This decorrelation can cause random variations in speckle brightness to generate high secondary peaks that can

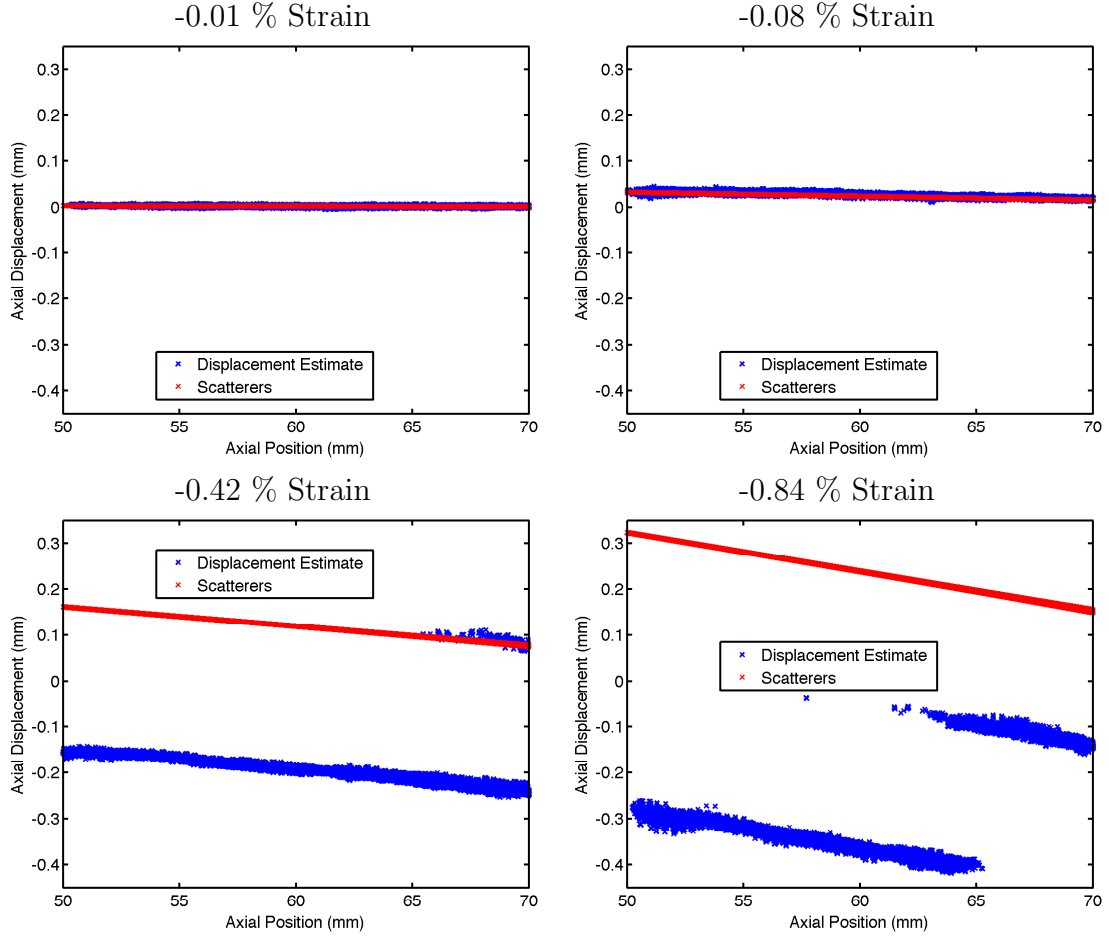


FIGURE 5.7: Example axial displacement versus position using 3-D tracking as compared with the input scatterer displacement for all strains simulated. In the lower plots (that correspond to larger displacement amplitudes), there are differences observed between the displacement estimates and the change in scatterer position simulated.

exceed the magnitude of the true peak [135, 195]. The 3-D phase sensitive normalized cross correlation algorithms used for displacement estimation have previously been shown to be susceptible to peak hopping artifacts [26]. These errors can be addressed using nonlinear correction methods [72, 135], but these have not been implemented in this work as they can be computationally intensive and correction in one dimension of displacement will not generally correct errors in displacement estimates in the lateral and elevational dimensions.

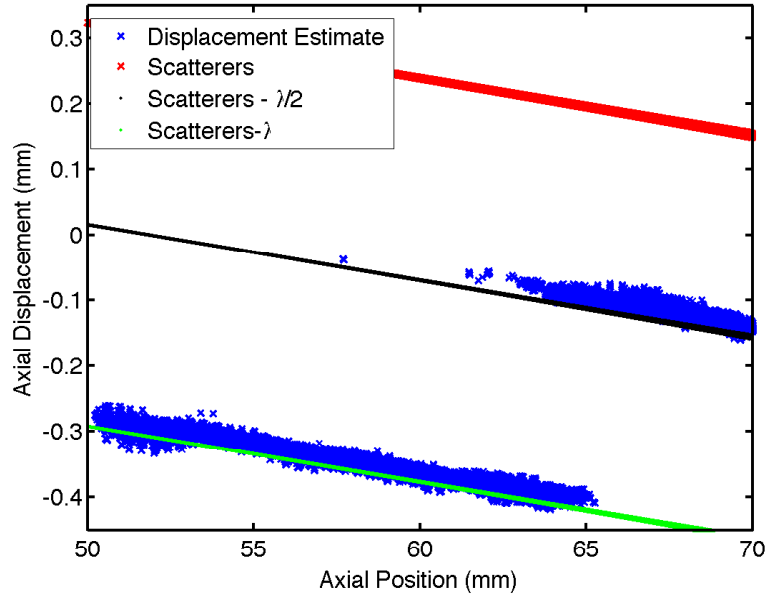


FIGURE 5.8: Displacement estimate plotted with the correct scatterer displacement and the scatterer displacement shifted by $\lambda/2$ and λ . The relationship between the underlying simulated displacement (as represented by the scatterer red line) and the displacement estimate is clearly either a factor of $\lambda/2$ or of λ , a pattern which strongly suggests peak hopping behavior.

The axial strain estimation results for the simulated and tracked displacements are shown in Table 5.3. In the table, the values shown for the variability of the estimate are the standard deviation of the 8 independent speckle realizations tested and not the 95% confidence interval. All the values of the strain estimate are consistent and correct for the simulations except for the 0.84% strain case. It is clear that the 0.84% strain estimation case linear regression is severely impacted by the peak hopping displacement estimation error as the estimates are the wrong sign and in no cases did the 95% confidence interval (not shown in the table) of the strain fit overlap the correct value. In all strain estimation cases tested, the method of using linear regression to scatterer displacements versus axial position in the underlying scatterers yielded accurate estimates of axial strain. This accuracy was also reflected in strain estimates generated from 3-D displacement estimates of tracked simulated

RF-data for strains $< 0.42\%$. However, for cases with larger underlying bulk displacement (corresponding to axial strains $> 0.42\%$), peak hopping of displacement estimates was observed and increasingly affected the estimates of axial strain to the point where strain estimates generated in the 0.84% strain case were incorrect.

Axial strain estimates using different displacement inputs		
LS-DYNA TM	Scatterer Position	Displacement Estimate
$-8.3e-3 \pm 3.0e-4$	$-8.6e-3 \pm 2.8e-7$	$-9.0e-3 \pm 1.4e-3$
$-8.41e-2 \pm 1.1e-3$	$-8.6e-2 \pm 2.7e-6$	$-8.9e-2 \pm 3.2e-3$
$-0.42 \pm 5.4e-3$	$-0.43 \pm 1.3e-5$	$-0.40 \pm 4.0e-2$
$-0.84 \pm 1.1e-2$	$-0.86 \pm 1.7e-5$	1.21 ± 0.06

Table 5.3: Axial strain estimates (quoted in %) based on averaging finite element strain estimates, linear regression to the assigned scatterer positions, and linear regression to the axial displacements using 3-D cross correlation methods on simulated tracked data. Average and standard deviation of 8 speckle realizations are given for the scatterer and displacement estimate results. For the simulated LS-DYNATM output, the average and standard deviation of the region of interest is shown.

As shown in Figure 5.5, the 95% confidence interval on the strain estimate for the 0.84% compression case is still relatively small (0.01%). This value was much smaller than values of 0.06% seen with some liver strain estimates and thus cannot be used as a cutoff to determine the presence or absence of peak hopping artifacts in underlying displacement data.

Elevation and Lateral Strain Estimation

Lateral and elevational strain estimation accuracy were also tested using the same methods as described in the axial strain estimation section. However, a slightly different gold standard was used to compare the LS-DYNATM axial strain estimate gold standard to different strain estimation methods using assumptions of incompressibility. Since the model was nearly incompressible ($\nu = 0.499$), we can extrapolate from the calculated axial strains to the predicted lateral and elevational strains. This is due to the fact that $\lambda = 1 + E_{11}$ and the perpendicular strains will equal

$E_{22} = E_{33} = \frac{1}{\sqrt{\lambda}} - 1$. This approach has been used extensively to generate estimates of perpendicular strains using ultrasound data as well [123, 101, 166]. The strains estimated by linear regression of scatterer position and 3-D cross-correlation based displacement estimate versus position were compared to the predicted elevation and lateral strain using the FEM based axial strain calculation and assumptions of incompressibility. The lateral and elevational strain estimates from LS-DYNATM are compared with the linear regression to the scatterer displacements for the three different dimensions in Figures 5.9, and 5.10. For all four strain states and 8 scatterer realizations, lateral and elevational strain estimates based on linear regression of scatterer displacement and position agreed very well with the finite element simulated strains. The average error of the scatterer displacement-based strain estimate for the four strain states in the lateral and elevation dimensions were $2.3\% \pm 0.5\%$. These results are shown quantitatively as well in Tables 5.4 and 5.5.

Lateral strain estimates using different displacement inputs		
LS-DYNA TM	Scatterer Position	Displacement Estimate
$4.2e-3 \pm 3.0e-4$	$4.3e-3 \pm 1.1e-7$	$-2.2e-3 \pm 0.01$
$4.2e-2 \pm 1.1e-3$	$4.3e-2 \pm 1.0e-6$	-0.03 ± 0.03
$0.21 \pm 5.4e-3$	$0.22 \pm 5.0e-6$	0.27 ± 0.02
$0.42 \pm 1.1e-2$	$0.43 \pm 1.0e-5$	0.36 ± 0.03

Table 5.4: Lateral strain estimates (quoted in %) based on averaging finite element strain estimates, linear regression to the scatterer displacements, and linear regression to the ultrasound-based displacement estimates generated with 3-D cross correlation methods on simulated tracked data. Average and standard deviation of 8 speckle realizations are given for the scatterer and displacement estimate results. The LS-DYNATM errors quoted are based on average and standard deviation in the region interrogated with the simulated ultrasound beams.

Figure 5.11 shows the estimates of lateral displacement with the lateral strain estimate overlaid. The lateral strain estimate for small strains is not close to the expected value but improves with larger strains as expected. The banding close to position 0 relates to the angular component of the phased array - at larger angles

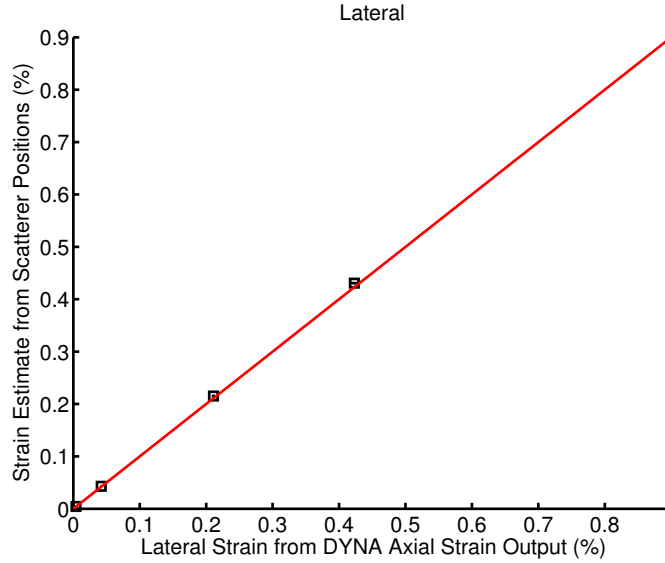


FIGURE 5.9: Lateral strain estimate based on linear regression of scatterer displacement versus position as compared with the average of the finite element simulation strain estimate in the region of interest. Errorbars shown which appear to be generally smaller than the marker size are the standard deviation of eight scatterer realizations (for the scatterers) or the strain estimate in the region of interest (for the simulations).

away from the center line, the lateral position of the displacement estimate will vary more with depth for one B-mode line. Table 5.4 suggests that above a lateral strain of 0.21% we were able to accurately estimate lateral strains using our experimental and simulation setup. This is consistent with existing literature that suggests lateral strain estimation feasibility only above the displacement estimation jitter-induced noise floor [145]. Below this value, the strain estimates were wrong and the wrong sign, but continued to be very close to zero.

Table 5.5 describes a similar pattern in the elevation dimension to that observed in the lateral strain estimation data. These results suggests that above an elevational strain of 0.21% we were able to accurately estimate elevational strains using our experimental and simulation setup. Since we are using a matrix array, we would expect this result to be consistent with existing literature that suggests strain estimation

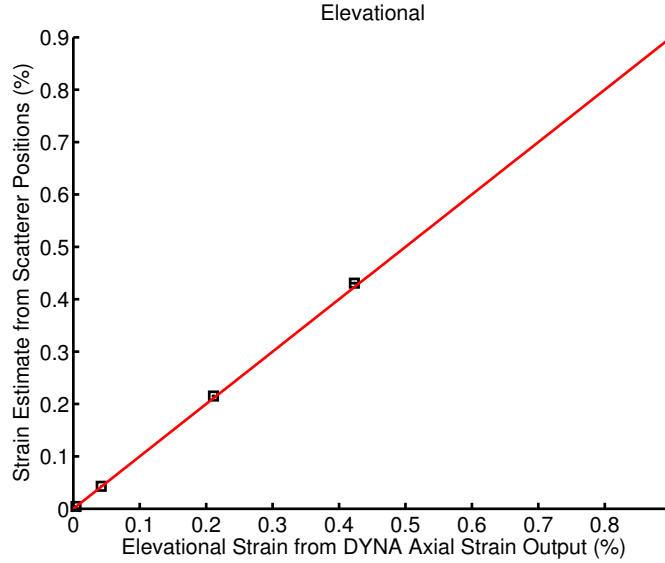


FIGURE 5.10: Elevational strain estimate based on linear regression of scatterer displacement versus position as compared with the average of the finite element simulation strain estimate in the region of interest. Errorbars shown which appear to be generally smaller than the marker size are the standard deviation of eight scatterer realizations (for the scatterers) or the strain estimate in the region of interest (for the simulations).

Elevational strain estimates using different methods		
LS-DYNA TM	Scatterer Position	Displacement Estimate
$4.2e-3 \pm 3.0e-4$	$4.3e-3 \pm 5.3e-8$	$1.3e-2 \pm 0.01$
$4.2e-2 \pm 1.1e-3$	$4.3e-2 \pm 6.0e-7$	$-2.8e-2 \pm 0.04$
$0.21 \pm 5.4e-3$	$0.22 \pm 2.6e-6$	0.23 ± 0.02
$0.42 \pm 1.1e-2$	$0.43 \pm 5.3e-6$	0.30 ± 0.03

Table 5.5: Elevational strain estimates (quoted in %) based on averaging finite element strain estimates, linear regression to the assigned scatterer positions, and linear regression to the elevational displacements using 3-D cross correlation methods on simulated tracked data. Average and standard deviation of 8 speckle realizations are given for the scatterer and displacement estimate results. The LS-DYNATM errors quoted are based on average and standard deviation in the region interrogated with the simulated ultrasound beams.

feasibility only above the displacement estimation jitter-induced noise floor [145]. The elevational strain estimation accuracy is slightly worse than that observed in the lateral dimension due to coarser beam spacing in this dimension.

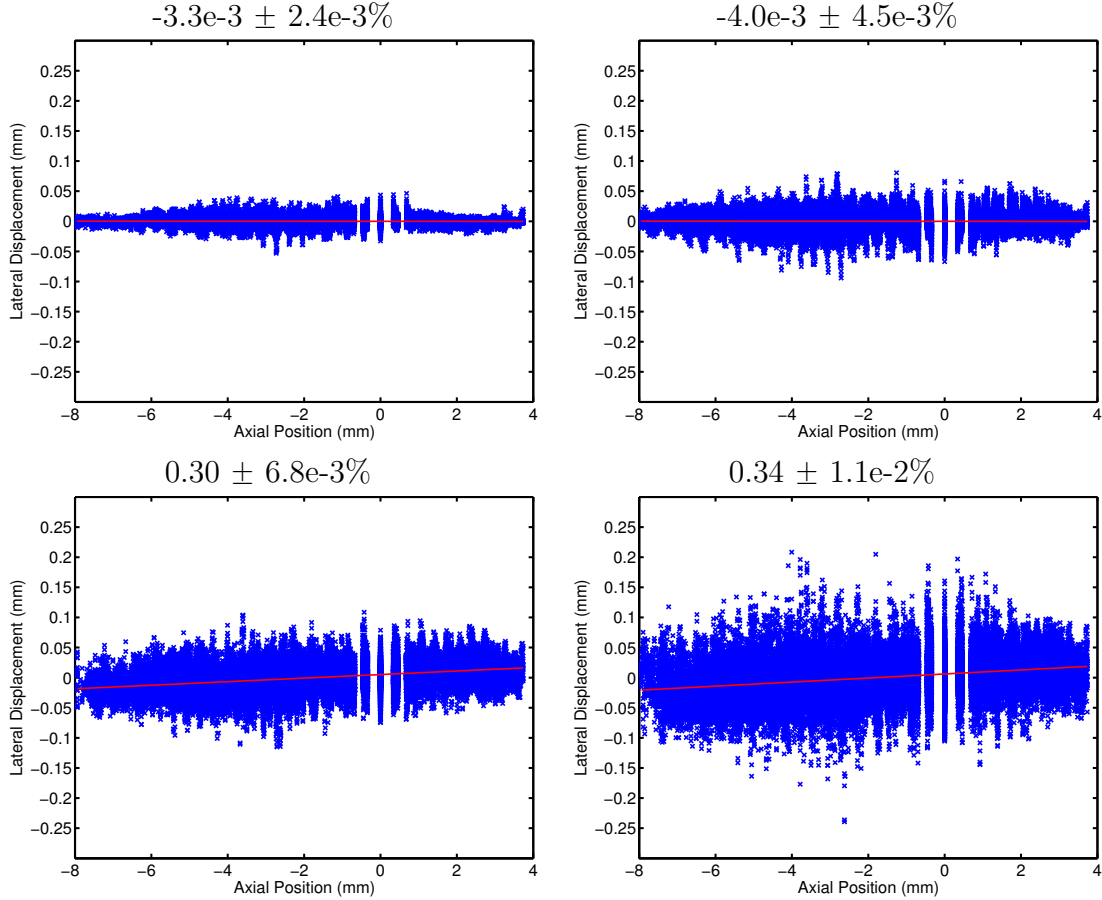


FIGURE 5.11: Example simulated and tracked lateral displacement versus position using 3-D tracking for the four simulated strain cases. The calculated strain for each of the datasets are shown with intervals quoted as the 95% confidence interval of the line fit and the mean displacement is subtracted so all the displacements are centered around zero. While the two largest strain cases (bottom row) are close to the expected result, the smallest strain estimates are the incorrect sign. Lateral displacement estimate variability increases with increasing lateral strain.

5.4 Conclusions

This work has described the validation for methods used to calculate the strain of hepatic deformations by linear regression of displacement as compared with position for the imaging parameters used in our experimental setup. The simulated ultrasonic tracking setup and described strain estimation algorithms will be used to generate volume-to-volume strain estimates experimentally which will be accumulated to gen-

erate estimates of change in hepatic strain with increasing portal venous pressure. Thus, a method for accurately measuring strain for each hepatic pressurization increment is necessary. In the axial dimension, large bulk displacements led to peak hopping which caused inaccuracies in large strain estimation. However, strains below 0.42% could be accurately measured using the linear regression and displacement estimation methods described. Thus, the ultrasound volume acquisition rate can be increased experimentally to the point where the change in strain between volumes is less than 0.42%. As described in Chapter 4, jitter on lateral and elevational displacement estimates is much larger than that observed in the axial dimension. This causes the observed behavior that the minimum strain that is able to be quantified accurately in the lateral and elevational dimensions is 0.2%, which is much higher than that reported in the axial dimension. Given the strains simulated in all three dimensions, the minimum strain that can be accurately tracked and estimated with our experimental setup in the elevation and lateral dimensions and the maximum strain that can be assessed without peak hopping artifacts in the axial dimension were able to be predicted. While in the hepatic pressurization experiments, the volume rate can be increased to prevent strains greater than 0.42% between volumes, it is unfortunately not possible to decrease the volume rate in order to generate strain estimates in the lateral and elevation dimension greater than 0.2%. This is due to the nature of the planned experiments in that the strains are expected to be accumulated for each 5-10 mmHg portal venous pressure increase increment. In some of these increments, strains lower than 0.2% were observed for the entire pressurization step. This would prohibit elevational and lateral strains from being accumulated accurately in the experimental methods described for the hepatic pressurization experiments described in Chapter 6. While axial strain estimates are predicted to be accurate for hepatic strain accumulation, the low frequency used for ultrasonic tracking and the lack of phase information in the lateral and elevation dimensions [145]

prevent three-dimensional strain tracking for the experiments described in Chapter 6.

6

Ultrasonic characterization of the nonlinear properties of canine livers by measuring shear wave speed and axial strain with increasing portal venous pressure

This paper has been submitted to the Journal of Biomechanics

coauthors: Brett Byram, Mark Palmeri, Michael Wang, and Kathryn Nightingale

6.1 Abstract

Hepatic venous pressure is increased in advancing liver disease and is considered the primary source of complications (such as variceal bleeding and ascites). Measurement of clinically significant increases in portal pressure is important for managing liver disease and is performed using the invasive method of hepatic venous pressure gradient (HVPG). We have previously reported that ARFI based shear wave speed (SWS) estimate increases with increasing hepatic venous pressure require an underlying tissue deformation. This study is designed to elucidate the nonlinear properties of the liver during pressurization by measuring both the shear wave speed and

strain. In this work, tissue deformation during hepatic pressurization was tracked in 8 canine livers using successively acquired 3-D B-mode volumes and compared with concurrently accrued SWS datasets. When portal venous pressure was increased from clinically normal (0-5 mmHg) to pressures representing highly diseased states at 20 mmHg, axial strain was observed to increase up to 10%. At the same time, SWS estimates were observed to increase from 1.5-2 m/s at 0-5 mmHg (baseline) to 3.25-3.5 m/s at 20 mmHg.

6.2 Introduction

Increasing portal venous pressure is one of the hallmarks of advancing liver disease and contributes to leading causes of death and morbidity from cirrhosis, such as variceal hemorrhage [146, 71, 164]. In addition, monitoring hemodynamic response to therapies for reducing hepatic pressure through use of Hepatic Venous Pressure Gradient (HVPG) measurement has proven effective in prolonging life, but is expensive and invasive [79]. Ultrasound imaging has been widely used for imaging the liver and gallbladder [197] and therefore is ideal for potential noninvasive hepatic pressure measurements. Duplex Doppler ultrasonography has been previously proposed for HVPG estimation [198, 203, 197] and has shown a clear relationship between quantitative results and esophageal varices development [12]. However, this method is not sufficiently accurate or reproducible between observers for implementation in clinical practice for HVPG quantification [13, 42, 184]. Ultrasound-based estimates of liver stiffness have been reported to increase with hepatic pressure [107, 184, 25, 149], suggesting that stiffness-based approaches may provide the basis for a noninvasive and inexpensive approach toward characterizing portal vein pressure in the clinic. These include splenic stiffness measurements [170] and direct liver stiffness measures [149, 74].

The major challenge to noninvasive stiffness-based metrics for characterizing hep-

atic pressure in-vivo is that estimates of hepatic stiffness are also known to increase with advancing fibrosis stage [170, 149, 128, 58, 199, 5, 38]. While splenic stiffness has also been observed to increase with esophageal varices risk and portal venous pressure, splenic stiffness is also increased from baseline in patients with cirrhosis and without high levels of esophageal varices risk [170]. Thus, a better understanding of the mechanisms by which hepatic pressure modulates estimates of liver stiffness could provide information needed to distinguish increasing hepatic pressure from advancing fibrosis stage. We have previously reported the nonlinear hyperelastic behavior of the liver as portal venous pressure increases [151]. In this work, an experiment was designed to simultaneously measure changes in hepatic strain and stiffness with increasing hepatic pressure in excised canine livers.

6.3 Background

This work primarily focuses on the potential applications of nonlinear characterization of the liver using shear wave speed metrics toward noninvasive hepatic pressure characterization. Nonlinear properties of the liver have previously been explored for the purpose of computational surgery guidance [82] and modeling car accident injury [23] as well as development of power law based models for soft tissues [114]. Nonlinear mechanical property evaluation of soft tissues such as the liver often requires information about corresponding stress and strain at particular time points. In the pressurized liver, because the geometry is so complicated, it is not feasible to translate the portal venous pressure directly into a stress without many simplifying assumptions. However, it is of clinical interest for potential applications of noninvasive pressure characterization to characterize the nonlinear mechanical properties that determine the increase in liver stiffness corresponding to portal venous pressure increases. The experiments described herein are inspired by acoustoelasticity experiments in that they generate estimates of shear wave speed and applied strain

[67, 163], but novel in that both the applied strain and the resulting shear wave speed increase are measured using ultrasonic metrics in response to an unknown applied stress in the form of portal venous pressure.

6.4 Methods

Experimental Animals: Experimental excised canine livers were obtained through cooperation with the Duke University Vivarium and euthanasia was achieved within the guidelines provided by the Duke Institutional Animal Care and Use Committee. Imaging was performed within 2 hours of excision and heparin was administered prior to euthanasia in 7 of the 8 cases to reduce coagulation effects.

Evaluation of Hepatic Changes with Pressurization: The experiments described were designed to compare changes in hepatic deformation and stiffness estimates with increasing portal venous pressure. Eight excised canine livers were investigated. After the canine liver was removed, the hepatic artery, hepatic vein, and portal vein were cannulated and the hepatic artery and vein were closed. In all livers, super glue (Loctite[®] Westlake, OH) was used to seal any observed defects in the liver capsule due to the liver extraction (all defects were $< 2\text{mm}$). The liver was then placed in a heparinized saline bath for five minutes to remove remaining air in the liver. We attempted to mitigate the effects of included air, saline leakage, and clotting, because all could contribute to decreased observed strain and stiffness response to increasing hepatic pressure.

Increasing portal venous pressure was achieved by attachment of the portal vein to a variable height saline reservoir as described in [151]. A diagram of the experimental setup is shown in Figure 6.1.

In order to characterize hepatic expansion, the livers were allowed to expand in a heparinized saline bath throughout the experiment. Liver pressure was increased

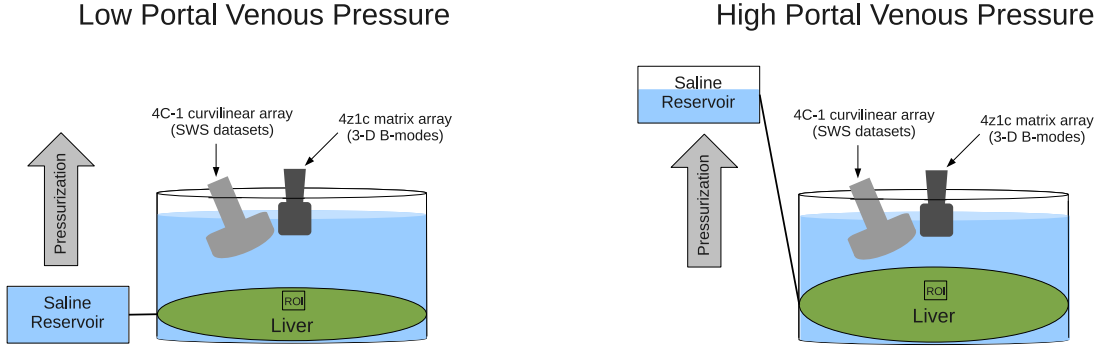


FIGURE 6.1: Diagram of the hepatic pressurization and monitoring setup

stepwise from 0-20 mmHg with pressurization steps at 0.5-5 mmHg in magnitude as measured using a handheld digital manometer (SPER Scientific, Ltd., resolution = 0.075 mmHg) attached to the portal vein cannulation setup. During each pressurization step, 3-D B-mode datasets were acquired using a Siemens SC-2000TM scanner and 4z1c matrix array ([57] Siemens Medical Systems, Ultrasound Group, Mountain View, CA, USA). The 3-D B-mode volumes were acquired with a frame rate of 0.1 Hz for up to 4 minutes over a 2x1.2x1.2 cm volume located 5-7 cm axially away from the transducer. An example of a single A-line through time from the 4-D dataset acquired for one pressurization increment is shown in Figure 6.2. After each pressurization step, 6 SWS datasets were acquired with a separate system as described below from the region corresponding to that in which the 3-D B-mode acquisition occurred.

Three-Dimensional Displacement Estimation: Because the liver expansion occurs in all directions, a 3-D displacement estimation kernel and search region were used to determine the axial displacements used for calculation of axial strain. Axial displacements were estimated using phase-sensitive 3-D cross correlation [47, 194]. Phase-sensitive normalized cross correlation with grid slopes algorithm sub-sample estimation was implemented as described in by Byram et al. [26]. A 0.9 correlation coefficient

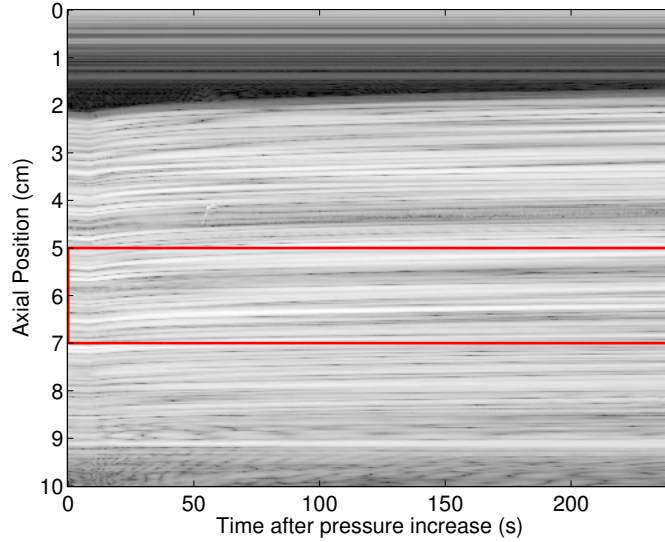


FIGURE 6.2: Example of data acquired in a pressurization increment between 17 and 18 mmHg portal venous pressure in one excised canine liver. One axial A-line through the center of the volume interrogated is shown through time after pressure increase. Expansion is observed in the growth of the brighter region, which represents the liver. The red lines represent the axial extent of the 3-D region of interest over which strain was computed.

cutoff was implemented for the displacement estimates. Details of the displacement estimation parameters for hepatic deformation quantification can be found in Table 6.1.

These parameters are consistent with the kernel sizes and dimensions previously reported for strain imaging in 2-D [90, 91, 193] and 3-D displacement estimation

Table 6.1: Parameters used for 3-D Displacement Estimation

Parameter	Value
Ultrasound Scanner	SC-2000
Probe	4z1c
F_c	2.8 MHz
Transmit Focus	8 cm
Imaging Depth	5-7 cm
Volume Rate	0.1 Hz
Axial Kernel	2.88 mm
Lateral Kernel	0.60 mm
Elevational Kernel	0.68 mm

[26, 93].

Strain Calculation: The axial strain was calculated using a least-squares fit to the axial displacement estimates in the region of interest as a function of axial position [83, 84]. Two examples of this calculation over the entire volume are shown in Figure 6.3. For each pressurization increment, displacement estimates were acquired every 10 seconds for a duration of up to 4 minutes (24 time steps). The volume rate was maintained so that all strains calculated were less than 0.42% as simulations of this experimental setup showed significant peak hopping for strain states above this value. Strain was calculated between each volume acquired and then accumulated for each pressurization increment.

SWS estimation Methods: Tissue stiffness was quantified using standard shear wave imaging methods [160, 116]. Radiation force-induced displacements were estimated from IQ data offline using Loupas phase-shift estimator [139, 100]. The time of the peak displacement at each lateral position was used to identify the arrival time for SWS approximation [132, 157] as shown in Figure 6.4. Shear waves were generated via acoustic radiation force using a Siemens ACUSON scanner and 4C-1 curvilinear array using the Siemens quantitative elasticity imaging tool with post-processing of the I/Q data acquired performed offline [151]. Displacements between 1.4-8 mm lateral to the radiation force excitation were used to generate shear wave speed estimates using a RANSAC-based time-of-flight algorithm [192].

6.5 Results

The comparison between shear wave speed and strain estimates in pressurized livers was performed in order to evaluate the relationship between strain and stiffness in a material with known nonlinear mechanical properties and irregular geometry. Ultrasound based estimates of tissue stiffness (via shear wave speed estimation) and

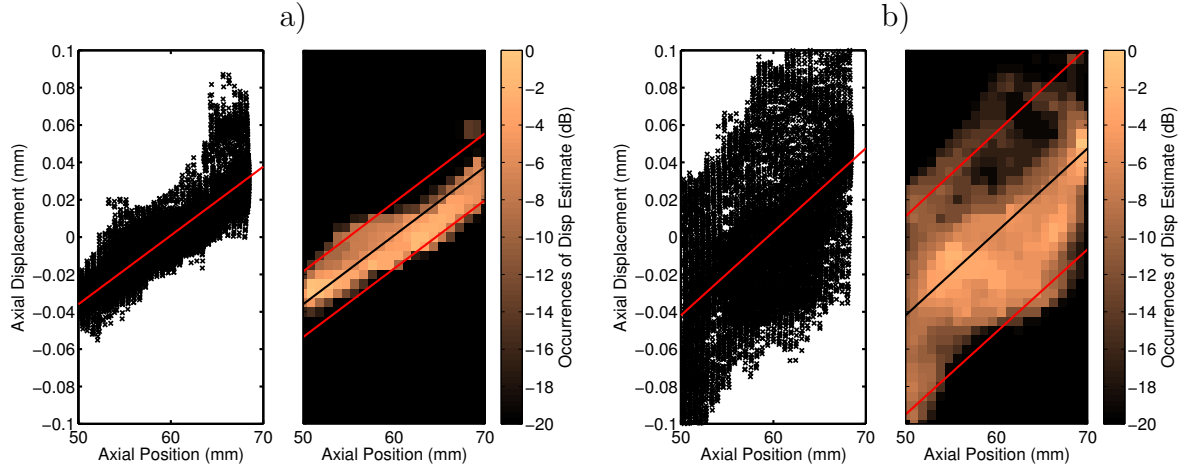


FIGURE 6.3: Axial strain calculation was performed using linear regression between axial displacement and axial position throughout the imaging volume for each time step (14080 kernels/volume). Subplots a) and b) provide example results from similar strain states in two different livers but with very different 95% confidence intervals on the strain estimate. In the left of each subfigure, all the displacement estimates used to perform the linear regression are shown while on the right the distribution of displacement estimates at each axial position is shown. The red lines on the right side of each subfigure show the bounds of the 95% confidence interval of the linear regression. In subfigure a), the strain was 0.37% with the confidence interval of 0.03% while in subfigure b), the strain was 0.45% and the confidence interval was 0.1%.

axial strain were acquired in the same region to develop a better understanding of tissue nonlinear properties. These nonlinear properties dictate the response of the liver to increasing portal venous pressure and may provide the basis for a noninvasive method for pressure measurement in the future.

Figure 6.5 shows an example of the strain accumulation process for one pressurization increment. An increase of 5% axial strain was observed during an increase in portal venous pressure from 17 to 18 mmHg. The red markers show the summed axial strain while the errorbars on the red line in the figure represent the summed 95% confidence intervals on each strain fit shown in blue.

The region of interest interrogated was observed to move toward the transducer in addition to expanding with increases in portal venous pressure. Figure 6.6 shows a comparison between the original region of interest with change in position calculated

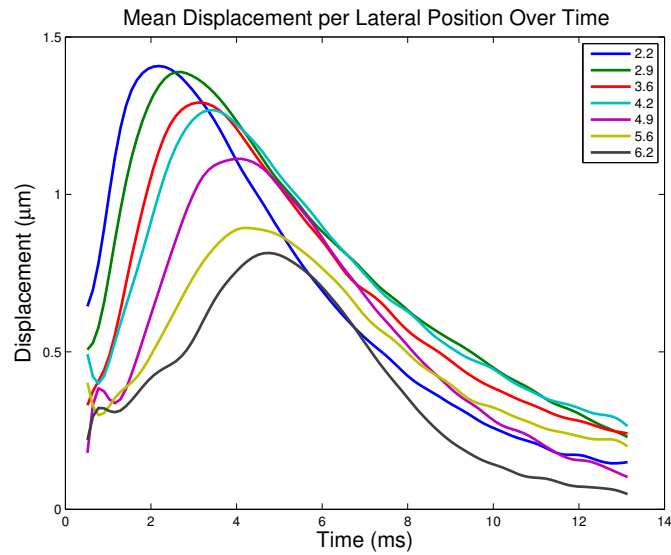


FIGURE 6.4: Sample dataset showing displacements at various lateral positions averaged over the depth of field around the focal depth in a sample hepatic experimental dataset. The ARFI push occurs at lateral position = 0mm and the displacement through time profiles at various locations are shown. Each colored line represents a different lateral position, and the shear wave speed can be calculated by observing the arrival time shift as the wave propagates laterally. A 1000 Hz low-pass filter has been applied to the displacements in the temporal dimension.

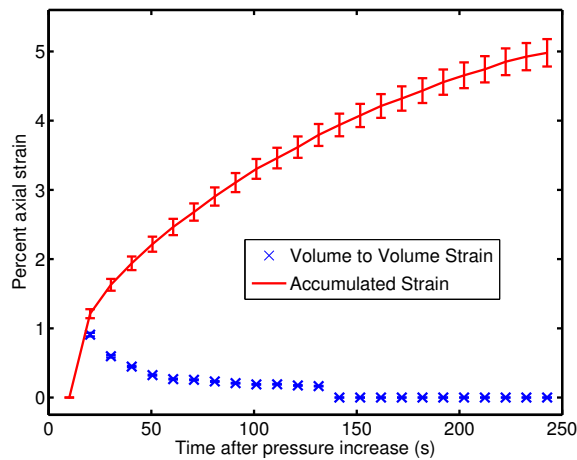


FIGURE 6.5: Axial strain during a pressurization increment between 17 and 18 mmHg as estimated using accumulation of individual volume-to-volume strain calculations. The errorbars shown are the accumulated 95% confidence intervals on the strain estimates (calculated as described in Figure 6.3).

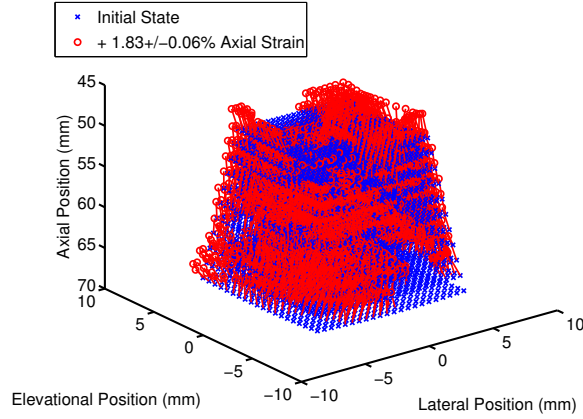


FIGURE 6.6: Example change in position and extent of the hepatic region interrogated for part of a pressurization step between 17 and 18 mmHg. Displacements were accumulated to demonstrate the change in the 3-D position and extent of the volume for an estimated 1.83% increase in axial strain.

using 3-D displacement estimation for an accumulated 6 volume-to-volume comparisons in one pressurization increment. The new locations of the estimated kernels are shown in red as compared with the original displacement estimation locations shown in blue.

Increases in SWS estimates and axial strain were observed with increasing portal

Shear Wave Speed vs. Portal Venous Pressure

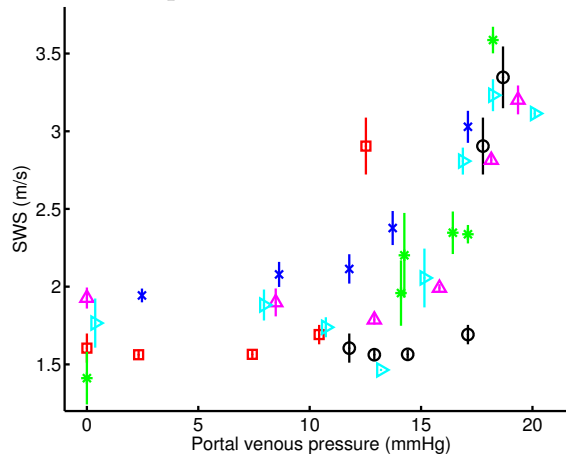


FIGURE 6.7: Shear wave speed increases observed with increasing portal venous pressure across 6 excised canine livers (differentiated by color). Errorbars shown represent the standard deviation of 6 shear wave speed datasets acquired in the same location at each pressure.

Axial Strain vs. Portal Venous Pressure

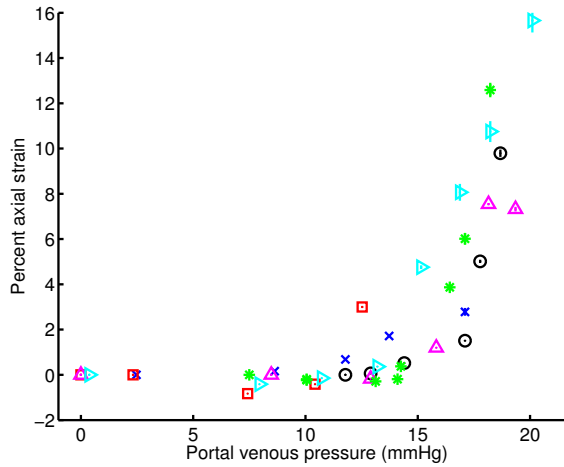


FIGURE 6.8: Percent axial strain increases observed as a function of increasing portal venous pressure for 6 excised canine livers (differentiated by color). Errorbars shown represent the accumulated 95% confidence interval on the strain estimate.

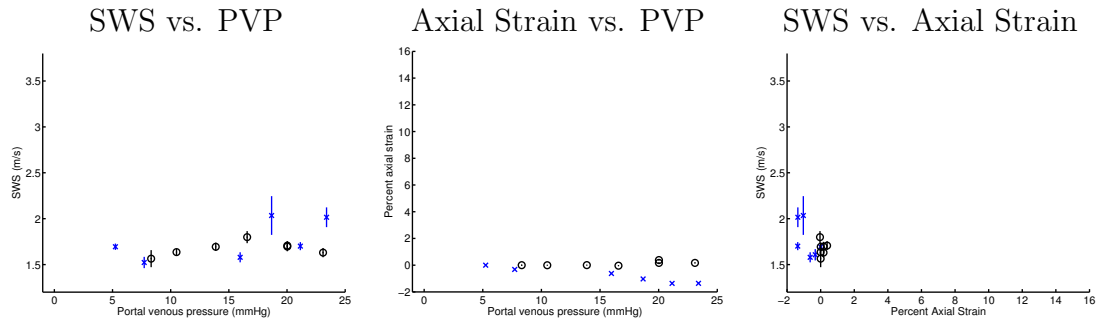


FIGURE 6.9: Comparison between shear wave speed, percent axial strain, and pressure in the two livers that were not observed to expand. For clarity, axes and errorbars shown correspond to those shown for the 6 cases in which expansion was seen.

venous pressure in six of the eight canine livers interrogated (see Figure 6.7 and Figure 6.8). SWS errorbars represent the standard deviation of 6 repeated measures in the same region of interest in a given liver while no percent axial strain errorbars are shown to represent that each is a single measure of accumulated strain.

In two livers, there were no increases in percent axial strain with pressurization. The relationship between shear wave speed, axial strain, and pressure for both cases are shown in Figure 6.9.

In each of the canine livers examined, increases in shear wave speeds were asso-

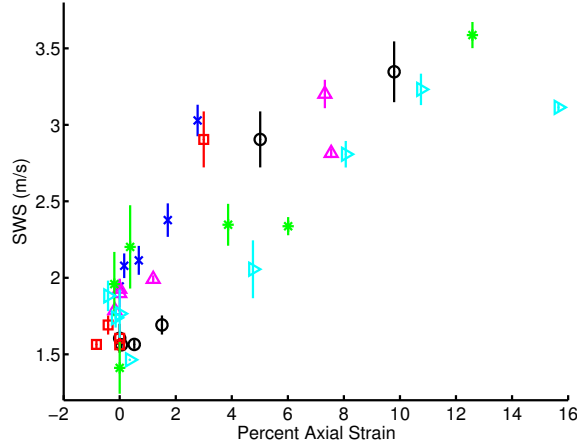


FIGURE 6.10: Shear wave speed compared with percent axial strain across 6 excised canine livers (differentiated by color) Because the six SWS estimates were in the same region of interest, the errorbars (which represent the standard deviation of the six SWS estimates) do not show potential tissue heterogeneity but rather the limits of system precision on SWS estimates.

icated with corresponding increases in estimates of percent axial strain. This relationship for the six cases in which both were observed to increase is shown in Figure 6.10.

6.6 Discussion

Increasing hepatic venous pressure is associated with advanced liver disease and worsening patient outcomes [164]. It has been shown that pharmacologically lowering and tracking portal pressure can be beneficial [79]. Therefore, a noninvasive metric for determining hepatic pressure and distinguishing it from the effect of advancing fibrosis stage would be clinically desirable. While hepatic stiffening reported due to advancing fibrosis stage has been suggested to occur due to increased fibrin and collagen deposition in the tissue [199, 58], previous work has suggested that a nonlinear strain-based mechanism underlies hepatic stiffening observed with pressurization [151]. In order to better understand the nonlinear hyperelastic properties of the pressurized liver, a novel experimental setup for determining concurrent shear

wave speed and axial strain estimates was designed and utilized.

In Figure 6.5, the accumulation of incremental axial strain estimates and 95% confidence interval can be observed for one pressurization increment. Since the strain estimation kernel does not change between acquisitions, the strains can be summed to generate an estimate of the accumulated strain. The summed 95% interval represents the confidence interval of the summed strain estimate.

Figure 6.6 shows an example of the deformation and bulk motion observed with increasing hepatic pressure in the liver region interrogated. The 1.83% axial strain increase quoted corresponds to the accumulated strain calculated for the displacements shown. In addition, some blue points do not appear to have corresponding red points. This is due to removal of displacement estimates with a correlation coefficient lower than 0.9. Since pressure should correspond to a tri-axial expansion, we would expect to see the same expansion in all three Cartesian dimensions. The example shown appears to support this hypothesis as there appears to be 3-dimensional expansion. However, the low center frequency of the matrix transducer used (2.8 MHz) and small aperture did not allow for estimation of lateral or elevational strains for this experimental system [145].

SWS estimates were observed to increase from 1.5-2 m/s at 0-5 mmHg (baseline) to 3.25-3.5 m/s at 20 mmHg in 6 of the 8 canine livers interrogated. Shear wave speeds at baseline varied between 1.4 and 2 m/s in the livers tested. While this result is consistent with reported variability in healthy human livers [153], it may be that this baseline difference affects the response of the liver to applied portal pressure. This remains to be further investigated from the perspective of selecting either a nonlinear model to encompass the behavior of all healthy livers or choosing a class of models that should be fit to each liver individually in future work.

When portal venous pressure was increased from clinically normal (0-5 mmHg) to pressures representing highly diseased states at 20 mmHg, axial strain was observed

to increase up to 10%. Between 0 and 10 mmHg, some estimates of axial strain were observed to decrease slightly (up to 1%). It is possible that the static pressure in the saline bath around the liver plays a confounding role in the experiment. If that is the case, when the portal vein pressure is lower than the external static pressure, the liver may appear to decrease in size.

Although there was a clear correlation between increasing strain and shear wave speed, there was variability among the different livers. We hypothesize that some of the variability in shear wave speed increase as a result of elevating portal venous pressure may be a result of different strains achieved in different livers at the same pressure. For example, the canine liver corresponding to the red squares clearly has a lower pressure at which an increase in shear wave speed and percent axial strain were observed (Figure 6.7), but appear consistent with the relationship between shear wave speed and percent axial strain seen in the other hepatic cases (Figure 6.8). This result is likely due to the pressure behaving differently on livers with different geometries and supports the use of strain and shear wave speed measures for quantifying tissue nonlinear behavior. The complex geometry of the liver does not allow use of the relationship between pressure and strain or stiffness to directly generate predictions of nonlinear behavior. In addition, the increases in SWS corresponding to axial strain increases of 4% above baseline configuration suggest that a transition between where a linear model may be sufficient to states in which nonlinear regimes dominate occurs at smaller strain states in these data than the greater than 10% strain that is classically assumed to correspond to nonlinear hyperelastic behavior [94].

In two of the livers examined, neither expansion in the form of axial strain increase nor stiffening was observed. Figure 6.9 shows these results. This lack of expansion and stiffening still supports our hypothesis that deformation is required in order to observe SWS increases. In one of the cases, heparin was not administered prior

to euthanasia, so we hypothesize that clotting effects prevented the pressurization from communicating throughout the liver. In the other case, it is possible that a small defect in the liver capsule or air in the portal venous system prevented the distribution of the increasing portal venous pressure throughout the liver. It is unlikely that air, excessive clotting, or capsule defects would exist when interrogating increasing portal venous pressure in vivo, but the fact that even in those cases the shear wave speed and expansion of the liver were correlated continues to support the use of a strain-dependent model for the effect of hepatic pressure on stiffness metrics.

Increases in measurements of hepatic axial strain were associated with increases in concurrently acquired SWS estimates. Figure 6.10 shows the relationship between the accumulated axial strain at a given pressure and the average of 6 SWS estimates generated at each pressurization step. This data provides the correlation between SWS and strain, which will be used moving forward to generate nonlinear material models of hepatic tissues. A limitation of this initial study is that we used only healthy canine livers for the experiment. Because most patients who suffer from elevated portal venous pressure have advanced liver disease, it will also be important to explore the effect of cirrhosis on hepatic nonlinear behavior. However, these initial results suggest that hyperelastic material modeling of the liver on the basis of the correlation between shear wave speed and axial strain is possible and appropriate and may provide the basis for a nonlinear mechanical model that leads to an improved understanding of liver stiffening with disease-associated portal venous pressure increases.

6.7 Conclusions

This work shows that increasing shear wave speed estimates with hepatic pressurization are associated with increases in hepatic axial strain, and quantifies these behaviors. Increases from normal portal venous pressure to diseased (an increase

from about 0 to 20 mmHg) were associated with up to a 10% increase in axial strain and up to a 230% increase in liver shear wave speed estimate from baseline in normal canine livers. These results provide a foundation for hyperelastic material modeling of the liver.

Conclusions

Cirrhosis and chronic liver disease is an important cause of death and disability globally [4]. The increase in portal venous pressure (PVP) due to advancing liver failure [20, 150, 176] is responsible for the most severe clinical effects of hepatic disease [69]. Monitoring of PVP is important in the medical setting, and a repeatable and inexpensive method for measuring PVP in vivo would be a highly desirable and novel clinical tool. The novel contributions of this work toward these clinical goals span characterizing the stiffening behavior of the pressurized liver as resulting from nonlinear mechanical behavior, developing and validating tools such as displacement tracking and tissue strain estimation for the clinical imaging system used, and characterizing the hepatic nonlinear behavior with pressurization by comparing tissue deformation and stiffness.

The experiments described in Chapter 3 determined that the liver behaves in a nonlinear deformation-dependent manner by comparing a pressurized liver that was constrained from expansion with one that was free to deform. Hepatic deformation was shown to be correlated with observed liver stiffness increases, implying the need for a hyperelastic material model to describe this behavior.

In Chapters 4 and 5, a 3-D clinical system was used to validate methods later employed for 3-D tissue displacement and strain estimation. Accuracy and precision of 3-D displacement estimation was quantified and simulations were used to determine that only 1-D axial strain estimation could be performed within system limitations.

Finally, the results from Chapter 3 were used to inform experiments performed with the validated experimental methods (Chapters 4 and 5) to examine the relationship between metrics of liver stiffness and deformation in excised pressurized canine livers. The results from these experiments shown in Chapter 6 demonstrated that shear wave speed estimates and hepatic axial strain increase with portal venous pressure. Increase in portal venous pressure of excised canine livers from that representative of healthy (0-5 mmHg) to severely diseased (20-25 mmHg) states led to a 10% increase in hepatic axial strain and 230% rise in liver stiffness metrics as measured with shear wave speeds. These data provide the basis for nonlinear material modeling of liver behavior and inform future work toward noninvasive hepatic pressurization characterization.

7.1 Future work

Nonlinear material characterization using the experimentally-determined relationship between strain and shear wave speed in the pressurized canine liver can be performed by analyzing the fit of Neo-Hookean or Mooney-Rivlin hyperelastic material model [147, 17, 122, 19] parameters to experimental stiffness data collected from ex-vivo canine hepatic pressurization experiments shown in Chapter 6. The Neo-Hookean model contains one nonlinear parameter and the Mooney-Rivlin contains two. The theoretical basis for strain-dependent shear wave speed increases in a nonlinear material are described for the Mooney-Rivlin model in Appendix A. These models were chosen because they provide the basic mechanism of strain-dependent

stiffening seen in hyperelasticity and have previously been used to describe nonlinear tissue behavior [49, 122, 59, 19, 17]. Results shown in Chapter 6 provide the necessary strain and shear wave speed information to determine appropriate nonlinear parameters.

The work described in this dissertation is devoted to understanding the underlying mechanical properties of the liver. In the context of portal venous pressurization, the liver is observed to expand and stiffen. These behaviors were measured in Chapter 5 and the relationship between increases in pressure, shear wave speed, and hepatic axial strain have been quantified. However, the experiments shown fall short of generating a noninvasive quantitative metric for portal venous pressure characterization. In order to fully characterize the pressure and fibrosis stage of the liver, one measure of hepatic stiffness would not be sufficient. A fully characterized nonlinear tissue model would require two stiffness measures at different strain or pressurization stages in order to characterize underlying hepatic mechanics. There are several potential methods for gaining this information. First, a patient with liver disease could have their stiffness measured at each clinic visit. Thus, once the patient reached an F4 fibrosis stage in which no further replacement of normal liver tissue with fibrotic material is expected, further increases of hepatic stiffness could be attributed to pressurization. While this potential method is the simplest, new experiments and histological studies would be required of patients with cirrhosis to determine if there is a point beyond which the hepatic stiffness at normal pressure is no longer predicted to increase. The second potential method for noninvasive hepatic pressurization characterization using stiffness metrics would be to generate two estimates of strain and SWS at different pressurization or strain states using pharmacology to lower portal venous pressure or external compression to modulate the strain state. With both methods, the relationship between the change in strain state with compression or pressure-lowering drug administration and shear wave speed could provide the ba-

sis for determining the hepatic fibrosis stage and pressurization state noninvasively. While this method has the potential for determining hepatic pressure and fibrosis stage for all potential stages of liver disease, experimental work on the potential for changing hepatic strain state via compression or pharmacology as well as development of simulations to predict the nature of the strain state changes required and potential underlying pressures associated with them would be necessary. The data collected and discussed in this work provides the basis for nonlinear mechanical modeling of the liver and the potential basis noninvasive characterization of hepatic pressure using stiffness metrics.

Appendix A

Nonlinear Material Modeling Example

Shear wave speeds have been observed to increase with increasing pressure in excised porcine livers [107] and in humans with elevated portal hepatic pressures [184, 25, 149]. This result is inconsistent with the linear elastic assumptions expressed in Equation 3.1. A change in estimates of liver stiffness with pressure implies a nonlinear relationship between stress and strain of a particular material [94, 122]. Nonlinear relationships between stress and strain in other biologic tissues have been previously reported [50, 92]. Hepatomegaly, an increase in liver size that would imply a change in underlying liver strain state, has also been reported in patients with increased portal pressure due to right-sided congestive heart failure [37, 53]. The behavior of shear wave speeds in nonlinear materials should be considered for examining these effects.

Shear Wave Propagation in a Hyperelastic Material

Biologic tissues such as the liver are known to behave nonlinearly [81, 59]. The relationship between shear wave speed and mechanical properties of tissue can be derived from governing equations that describe tissue. This relationship has been

thoroughly examined in the linear case to yield the results shown in Equation 3.1. A diagram of the dimensions referred to in the following derivation is shown in Figure 2.5. Unlike linear materials, a hyperelastic material will require definition of a strain-energy function, W , with a fixed relationship to the strain state of the material [76, 122] and the following correspondence to the stresses:

$$\sigma_{ij} = \frac{\partial W}{\partial \epsilon_{ij}} \quad (\text{A.1})$$

The Mooney-Rivlin (MR) and Neo-Hookean (NH) models are commonly used hyperelastic formulations for modeling biologic tissues [81]. They can be described by the nonlinear strain-energy function which depends on two material constants C_1 and C_2 [122, 109, 147]:

$$W = 2C_1(I_1 - 3) + 2C_2(I_2 - 3) \quad (\text{A.2})$$

In Equation A.2, I_1 and I_2 are two principal invariants of the right Cauchy-Green deformation tensor, \mathbf{C} as described by:

$$I_1 = Tr[\mathbf{C}]$$

and

$$I_2 = \frac{1}{2}(Tr[\mathbf{C}]^2 - Tr[\mathbf{C}^2]).$$

When considering small strains (such as those generated by acoustic radiation force), the first strain invariant (I_1) will not be largely affected by shear strains while the second strain invariant (I_2) depends primarily on shear strain components. The MR formulation is described by the full Equation A.2, while the NH case corresponds to $C_2 = 0$ in Equation A.2.

Shear Waves in an Uncompressed Hyperelastic Solid The relationship between shear wave speed and mechanical properties in a hyperelastic material is similar to that of an elastic material in that it begins with a deformation state constrained to physical laws (wave equation and conservation of momentum) in a material defined by the hyperelastic constitutive law described above. In the case of a shear wave excitation using radiation force, we expect there to be shear waves radiating outward from the excitation in the elevation (x_3) and lateral (x_2) dimensions. The derivation follows the simple shear loading case described in [122]:

$$x_1 = X_1 + u_1(X_2, t) + u_1(X_3)$$

$$x_2 = X_2$$

$$x_3 = X_3$$

Lower case letters represent the deformed configuration and capital letters represent the undeformed (or reference) configuration.

We begin by calculating the deformation gradient, $F = \frac{\partial x_i}{\partial X_j}$:

$$F = \begin{pmatrix} 1 & \frac{\partial u_1}{\partial X_2} & \frac{\partial u_1}{\partial X_3} \\ 0 & 1 & 0 \\ 0 & 0 & 1 \end{pmatrix} \quad (\text{A.3})$$

The right Cauchy-Green deformation tensor $\mathbf{C} = FF^T$ will be:

$$\mathbf{C} = \begin{pmatrix} 1 + \left(\frac{\partial u_1}{\partial X_2}\right)^2 + \left(\frac{\partial u_1}{\partial X_3}\right)^2 & \frac{\partial u_1}{\partial X_2} & \frac{\partial u_1}{\partial X_3} \\ \frac{\partial u_1}{\partial X_2} & 1 & 0 \\ \frac{\partial u_1}{\partial X_3} & 0 & 1 \end{pmatrix} \quad (\text{A.4})$$

The strain-energy function follows:

$$W = 2(C_1 + C_2) \left(\frac{\partial u_1}{\partial X_2}^2 + \frac{\partial u_1}{\partial X_3}^2 \right) \quad (\text{A.5})$$

Because the transducer we image with is limited to the axial-lateral plane, we measure the shear wave speed in the lateral direction (described by the ϵ_{12} strain). We can take the derivative of W with respect to shear strain utilizing the following relationship between strain and displacement:

$$\epsilon_{12} = \frac{1}{2} \frac{\partial u_1}{\partial X_2} \quad (\text{A.6})$$

$$\Rightarrow \sigma_{12} = 4(C_2 + C_1)\epsilon_{12} \quad (\text{A.7})$$

The stress-strain relationship for this type of simple shear loading is:

$$\sigma_{12} = 4(C_1 + C_2)\epsilon_{12} = 2\mu\epsilon_{12} \quad (\text{A.8})$$

where $\mu = 2(C_1 + C_2)$ matches the linear isotropic elasticity case [94].

The general equation for a shear wave (direction of motion perpendicular to wave propagation direction) is as follows:

$$\frac{\partial^2 u_1}{\partial x_2^2} = \frac{1}{c^2} \frac{\partial^2 u_1}{\partial t^2} \quad (\text{A.9})$$

Above, u_1 is the displacement in the x_1 direction but it will only depend on x_2 as fits with the definition of shear (or transverse) wave propagation [94].

The relationship between strain and displacement from Equation A.6 can be plugged into Equation A.7 to produce:

$$\sigma_{12} = 2 \frac{\partial u_1}{\partial X_2} (C_1 + C_2) \quad (\text{A.10})$$

Navier's equations of motion [94] are expressed as:

$$\frac{\partial \sigma_{12}}{\partial X_2} \hat{e}_1 = \rho_o \frac{\partial^2 u_1}{\partial t^2} \hat{e}_1 \quad (\text{A.11})$$

Taking the derivative with respect to X_2 of Equation A.10 using the chain rule returns:

$$\frac{\partial \sigma_{12}}{\partial x_2} = 2 \frac{\partial^2 u_1}{\partial X_2^2} (C_1 + C_2)$$

Combining this result with the wave equation (Equation A.9) and again employing the chain rule gives the following expression.

$$\frac{\partial \sigma_{12}}{\partial X_2} = \frac{2}{c^2} \frac{\partial^2 u_1}{\partial t^2} (C_1 + C_2)$$

This result can be plugged in to Equation A.11 to derive the expression for shear wave speed, c_T as a function of material constants as follows.

$$\Rightarrow \frac{2(C_1 + C_2)}{c_T^2} \frac{\partial^2 u_1}{\partial t^2} \hat{e}_1 = \rho_o \frac{\partial^2 u_1}{\partial t^2} \hat{e}_1$$

$$c_T = \sqrt{\frac{2(C_1 + C_2)}{\rho_o}} \tag{A.12}$$

This result corresponds to the linear case for $\mu = 2(C_1 + C_2)$ and depends only on underlying material parameters without dependence on the magnitude of acoustic radiation force applied. Because acoustic radiation force magnitude can depend on ultrasonic parameters such as frequency and number of transducer elements used as well as tissue parameters such as attenuation, the independence of shear wave speed on the applied force provides a good mechanism for determining underlying quantitative material stiffness parameters in the linear regime.

Shear Waves in a Compressed Hyperelastic Solid In order to model hepatic pressurization, it will be useful to consider the case of underlying strain condition added to a

shear excitation in the hyperelastic material. This can be simply done using superposition of strain states when defining the displacements and deformation tensor, F . We can begin by examining uniaxial stress acting in the normal direction (as seen in [122, 76, 17]) combined with a small shear excitation used to describe shear waves propagating in tissue. This derivation follows the description of a finite amplitude wave in a compressed Mooney-Rivlin solid described in [17].

We begin by defining a deformation state:

$$x_1 = \lambda X_1 + u_1(X_2, t)$$

$$x_2 = \frac{1}{\sqrt{\lambda}} X_2$$

$$x_3 = \frac{1}{\sqrt{\lambda}} X_3$$

In this deformation state described, λ is also approximated as the stretch ratio in the compressive direction where $\lambda = \frac{x_1}{X_1}$ (since u_1 is much much smaller than the compression present in the material). The stretch can also be approximated as one plus the engineering strain in the compressive direction:

$$\lambda = 1 + \epsilon_{11}$$

We can find the deformation gradient from the deformation state:

$$F = \begin{pmatrix} \lambda & \frac{\partial u_1}{\partial X_2} & 0 \\ 0 & \frac{1}{\sqrt{\lambda}} & 0 \\ 0 & 0 & \frac{1}{\sqrt{\lambda}} \end{pmatrix} \quad (\text{A.13})$$

and $C = FF^T$:

$$\mathbf{C} = \begin{pmatrix} \lambda^2 + \left(\frac{\partial u_1}{\partial X_2}\right)^2 & \frac{\partial u_1}{\partial X_2} \frac{1}{\sqrt{\lambda}} & 0 \\ \frac{\partial u_1}{\partial X_2} \frac{1}{\sqrt{\lambda}} & \frac{1}{\lambda} & 0 \\ 0 & 0 & \frac{1}{\lambda} \end{pmatrix} \quad (\text{A.14})$$

$$I_1 = \left(\frac{\partial u_1}{\partial X_2}\right)^2 + \frac{2}{\lambda} + \lambda^2$$

$$I_2 = \frac{1}{\lambda^2} + \left(\frac{\partial u_1}{\partial X_2}\right)^2 \frac{1}{\lambda} + 2\lambda$$

These substitutions give the strain energy function:

$$W = 2C_1\left(\left(\frac{\partial u_1}{\partial X_2}\right)^2 + \frac{2}{\lambda} + \lambda^2 - 3\right) + 2C_2\left(\frac{1}{\lambda^2} + \left(\frac{\partial u_1}{\partial X_2}\right)^2 \frac{1}{\lambda} + 2\lambda - 3\right) \quad (\text{A.15})$$

In order to find the parameter interrogated by the shear wave propagation speed, we again can take the derivative of the strain energy function with respect to the shear component of the strain (using the fact that $2\epsilon_{12} = \frac{\partial u_1}{\partial X_2}$).

$$\sigma_{12} = 4\left(C_1 + \frac{C_2}{\lambda}\right) \frac{\partial u_1}{\partial X_2} \quad (\text{A.16})$$

In order to derive the appropriate relationships, we again take the derivative with respect to X_2 of Equation A.16:

$$\frac{\partial \sigma_{12}}{\partial X_2} = 2 \frac{\partial^2 u_1}{\partial X_2^2} \left(C_1 + \frac{C_2}{\lambda}\right) \quad (\text{A.17})$$

Navier's equation (see Equation A.11) produces another expression for $\frac{\partial \sigma_{12}}{\partial X_2}$:

$$\frac{\partial \sigma_{12}}{\partial X_2} = \rho_o \frac{\partial^2 u_1}{\partial t^2} \quad (\text{A.18})$$

Equations A.17 and A.18 combine to reveal this relationship:

$$2 \frac{\partial^2 u_1}{\partial X_2^2} \left(C_1 + \frac{C_2}{\lambda}\right) = \rho_o \frac{\partial^2 u_1}{\partial t^2} \quad (\text{A.19})$$

Noting that $\left(\frac{\partial X_2}{\partial x_2}\right)^2 = \lambda$, and using the chain rule and wave equation substitutions into Equation A.19 yields:

$$2\frac{\partial^2 u_1}{\partial X_2^2}\left(C_1 + \frac{C_2}{\lambda}\right) = \lambda\rho_o c^2 \frac{\partial^2 u_1}{\partial X_2^2}$$

This equation can lead to a prediction of shear wave speed (c_T) as a function of material parameters C_1 and C_2 as well as uniaxial compression state (λ).

$$2\left(C_1 + \frac{C_2}{\lambda}\right) = \rho_o c_T^2 \lambda$$

$$c_T = \sqrt{\frac{2\left(\frac{C_1}{\lambda} + \frac{C_2}{\lambda^2}\right)}{\rho_o}} \quad (\text{A.20})$$

The expression for shear wave speed simplifies to the linear result in the limit where $\lambda = 1$ (no compression). In addition, this expression suggests a relationship between the shear wave speed based estimates of tissue stiffness and the underlying strain state (λ) of the material. While this result predicts a dependence of shear wave speed on underlying compression state (λ), it still suggests an independence of shear wave speed from acoustic radiation force excitation magnitude. Because uniaxial compression or tension in an isotropic material supports two orthogonal strain quantities, this type of deformation will allow for two orthogonal shear wave speeds corresponding to Equation A.20 [17]. These will depend on the deformation λ or its orthogonal counterpart, $\sqrt{\lambda}$, leading to two excitable shear wave speeds in this type of hyperelastic material, propagating in orthogonal directions [17]:

$$v_1 = \sqrt{\frac{2\left(\frac{C_1}{\lambda} + \frac{C_2}{\lambda^2}\right)}{\rho_o}} \quad (\text{A.21})$$

$$v_2 = \sqrt{\frac{2(C_1\sqrt{\lambda} + C_2\lambda)}{\rho_o}} \quad (\text{A.22})$$

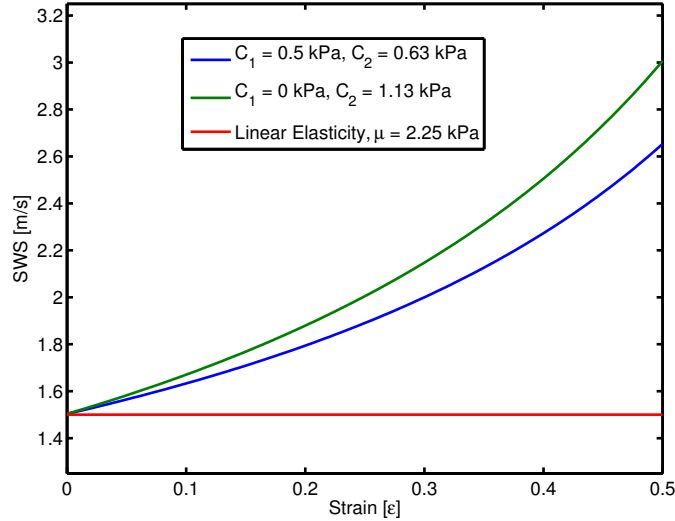


FIGURE A.1: Comparison between the theoretically predicted linear elastic behavior of SWS under material compression with those shear wave speeds predicted for two sets of Mooney-Rivlin material parameters.

An example of expected v_1 (or transverse SWS estimates) for deformations from 0-0.5 strain in a compressed Mooney-Rivlin material for shear wave speeds perpendicular to the compression are shown in Figure A.1.

The relationship between shear wave speed increases and hepatic strain have been experimentally determined for pressurized excised canine livers in Chapter 6. Thus, nonlinear material characterization using the experimentally-determined relationship between strain and shear wave speed in the pressurized canine liver can rely on fitting this data to parameters shown in Equation A.20. This model was chosen because it provides the basic mechanism of strain-dependent stiffening seen in hyperelasticity and has previously been used to describe tissue behavior [49, 122, 59].

Bibliography

- [1] JG Abraldes, I Tarantino, J Turnes, JC Garcia-Pagan, J Rodés, and J Bosch. Hemodynamic response to pharmacological treatment of portal hypertension and long-term prognosis of cirrhosis. *Hepatology*, 37(4):902–8, April 2003.
- [2] B Ahn and J Kim. Measurement and characterization of soft tissue behavior with surface deformation and force response under large deformations. *Medical Image Analysis*, 14(2):138–148, 2010.
- [3] SK Alam, J Ophir, and T Varghese. Elastographic axial resolution criteria: an experimental study. *IEEE Trans Ultrason Ferroelec Freq Control*, 47(1):304–309, 2000.
- [4] RN Anderson and BL Smith. Deaths: leading causes for 2001. *National Vital Statistics Reports*, 52(9):1–85, November 2003.
- [5] E Bavu, JL Gennisson, M Couade, J Bercoff, V Mallet, M Fink, A Badel, A Vallet-Pichard, B Nalpas, M Tanter, and S Pol. Noninvasive in vivo liver fibrosis evaluation using supersonic shear imaging: a clinical study on 113 hepatitis C virus patients. *Ultrasound in Medicine & Biology*, 37(9):1361–1373, 2011.
- [6] R Bendtsen, JH Henriksen, and TLA Srensen. Propranolol and haemodynamic response in cirrhosis. *Journal of Hepatology*, 13:144–148, 1991.
- [7] J Bercoff, M Tanter, and M Fink. Supersonic Shear Imaging: A new technique for soft tissue elasticity mapping. *IEEE Trans Ultras Ferroelec Freq Control*, 51(4):409, 2004.
- [8] A Berzuini, A Colli, A Gerosa, L Raffaele, I Guarnori, B Foglieni, M Spreafico, P Duca, F Bonino, and D Pratti. Factors related to liver stiffness values among healthy individuals: results from a prospective study. *Digestive and Liver Disease*, 41(A1-A45):A13, 2009.
- [9] M Bilgen and MF Insana. Error analysis in acoustic elastography. I. displacement estimation. *The Journal of the Acoustical Society of America*, 101(2):1139–46, February 1997.

- [10] W Bleibel and AMS Al-Osaimi. Hepatic encephalopathy. *Saudi Journal of Gastroenterology*, 18(5):301–9, September 2012.
- [11] LN Bohs, BH Friemel, BA McDermott, and GE Trahey. A realtime system for quantifying and displaying two-dimensional velocities using ultrasound. *Ultrasound in Medicine & Biology*, 19(9):751–761, 1993.
- [12] L Bolondi and S Gaiani. The relationship of endoscopy, portal Doppler ultrasound flowmetry, and clinical and biochemical tests in cirrhosis. *Journal of Hepatology*, 20:11–18, 1994.
- [13] L Bolondi, S Gaiani, and L Barbara. Accuracy and reproducibility of portal flow measurement Doppler ultrasound. *Journal of Hepatology*, 13:269–273, 1991.
- [14] J Bosch, JG Abraldes, and R Groszmann. Current management of portal hypertension. *Journal of Hepatology*, 38:54–68, 2003.
- [15] J Bosch, A Berzigotti, JC García-Pagán, and JG Abraldes. The management of portal hypertension: rational basis, available treatments, and future options. *Journal of Hepatology*, 48(S1):S92, 2008.
- [16] J Bosch and JC García-Pagán. Complications of cirrhosis. I. Portal hypertension. *Journal of Hepatology*, 32(S1):141–56, January 2000.
- [17] P Boulanger and M Hayes. Finite-amplitude waves in Mooney-Rivlin and Hadamard materials. In Michael Hayes and Giuseppe Saccomandi, editors, *Topics in Finite Elasticity*. Springer-Verlag Wein, New York, 2001.
- [18] J Boursier, A Konate, G Gorea, S Reaud, E Quemener, F Oberti, I Hubert-Fouchard, and P Cales. Reproducibility of liver stiffness measurement by ultrasonographic elastometry. *Clinical Gastroenterology and Hepatology*, 6(11):1269, 2008.
- [19] AF Bower. *Applied Mechanics of Solids*. CRC Press, 2010.
- [20] A Braillon, P Cales, D Valla, D Gaudy, P Geoffroy, and D Lebrec. Influence of the degree of liver failure on systemic and splanchnic haemodynamics and on response to propranolol in patients with cirrhosis. *Gut*, 27(10):1204–9, October 1986.
- [21] J Bruix, A Castells, J Bosch, F Feu, J Fuster, JC García-Pagán, J Visa, C Bru, and J Rodes. Surgical resection of hepatocellular carcinoma in cirrhotic patients: Prognostic value of preoperative portal pressure. *Gastroenterology*, 111(4):1022, 1996.

- [22] J Brum, JL Gennisson, TM Nguyen, N Benech, M Fink, M Tanter, and C Negrreira. Application of 1-D transient elastography for the shear modulus assessment of thin-layered soft tissue: comparison with supersonic shear imaging technique. *IEEE Trans Ultras Ferroelec Freq Control*, 59(4):703–14, April 2012.
- [23] A Brunon, K Bruyère-Garnier, and M Coret. Mechanical characterization of liver capsule through uniaxial quasi-static tensile tests until failure. *Journal of Biomechanics*, 43(11):2221–7, August 2010.
- [24] A Bummo and J Kim. Measurement and characterization of soft tissue behavior with surface deformation and force response under large deformations. *Medical Image Analysis*, 14(2):138–148, 2010.
- [25] C Bureau, S Metivier, JM Peron, J Selves, MA Robic, PA Gourraud, O Rouquet, E Dupuis, L Alric, and JP Vinel. Transient elastography accurately predicts presence of significant portal hypertension in patients with chronic liver disease. *Alimentary Pharmacology and Therapeutics*, 27(12):1261–1268, 2008.
- [26] B Byram, G Holley, D Giannantonio, and G Trahey. 3-D phantom and in vivo cardiac speckle tracking using a matrix array and raw echo data. *IEEE Trans Ultras Ferroelec Freq Control*, 57(4):839–54, April 2010.
- [27] TJ Carter, M Sermesant, DM Cash, DC Barratt, C Tanner, and DJ Hawkes. Application of soft tissue modelling to image-guided surgery. *Medical Engineering & Physics*, 27(10):893–909, December 2005.
- [28] L Castera, X Forns, and A Alberti. Non-invasive evaluation of liver fibrosis using transient elastography. *Journal of Hepatology*, 48(5):835–847, 2008.
- [29] L Castera, M Pinzani, and J Bosch. Non invasive evaluation of portal hypertension using transient elastography. *Journal of Hepatology*, 56(3):696–703, March 2012.
- [30] S Catheline, JL Gennisson, and M Fink. Measurement of elastic nonlinearity of soft solid with transient elastography. *The Journal of the Acoustical Society of America*, 114(6):3087–3091, 2003.
- [31] I Céspedes, M Insana, and J Ophir. Theoretical bounds on strain estimation in elastography. *IEEE Trans. Ultrason., Ferroelec., Freq. Contr.*, 42(5):969–972, 1995.
- [32] S Chen, M Fatemi, and J Greenleaf. Quantifying elasticity and viscosity from measurement of shear wave speed dispersion. *The Journal of the Acoustical Society of America*, 115(6):2781–2785, 2004.

- [33] S Chen, MW Urban, C Pislaru, R Kinnick, Y Zheng, A Yao, and JF Greenleaf. Shearwave dispersion ultrasound vibrometry (SDUV) for measuring tissue elasticity and viscosity. *IEEE Trans Ultrason Ferroelectr Freq Control*, 56(1):55–62, January 2009.
- [34] C Chui, E Kobayashi, X Chen, T Hisada, and I Sakuma. Combined compression and elongation experiments and non-linear modelling of liver tissue for surgical simulation. *Med Biol Eng Comput*, 42(6):787–798, 2004.
- [35] JFL Cobbold and SD Taylor-Robinson. Liver Stiffness values in healthy subjects: implications for clinical practice. *Journal of Hepatology*, 48:531, 2008.
- [36] RS Cobbold. *Foundations of Biomedical Ultrasound*. Oxford University Press, New York, NY, 2007.
- [37] RS Cotran, V Kumar, and T Collins. *Robbins Pathologic Basis of Disease*. W.B. Saunders Company, Philadelphia, PA, 1999.
- [38] G Crespo, G Fernández-Varo, Z Mariño, G Casals, R Miquel, SM Martínez, R Gilabert, X Forns, W Jiménez, and M Navasa. ARFI, FibroScan, ELF, and their combinations in the assessment of liver fibrosis: a prospective study. *Journal of Hepatology*, 57(2):281–7, August 2012.
- [39] G D’Amico, JC Garcia-Pagan, A Luca, and J Bosch. Hepatic vein pressure gradient reduction and prevention of variceal bleeding in cirrhosis: a systematic review. *Gastroenterology*, 131(5):1611–24, November 2006.
- [40] G D’Amico, JC Garcia-Pagan, and L Pagliaro. Natural history and prognostic indicators of survival in cirrhosis: a systematic review of 118 studies. *Journal of Hepatology*, 44(1):231, 2006.
- [41] G D’Amico, L Pagliaro, and J Bosch. The treatment of portal hypertension : a meta-analytic review. *Hepatology*, 22(1):332–354, 1995.
- [42] PJ de Vries, J van Hattum, JBL Hoekstra, and P de Hooge. Duplex Doppler measurements of portal venous flow in normal subjects. *Journal of Hepatology*, 13:358–363, 1991.
- [43] MH DeGroot and MJ Schervish. *Probability and Statistics: Third edition*. Addison-Wesley, 2002.
- [44] M Destrade and RW Ogden. On the third- and fourth-order constants of incompressible isotropic elasticity. *The Journal of the Acoustical Society of America*, 128(6):3334–3343, 2010.
- [45] M Destrade and G Saccomandi. Finite-amplitude inhomogeneous waves in Mooney-Rivlin viscoelastic solids. *Wave Motion*, 40:251–262, 2004.

- [46] A Duarte-Rojo, JT Altamirano, and JJ Feld. Noninvasive markers of fibrosis: key concepts for improving accuracy in daily clinical practice. *Annals of Hepatology*, 11(4):426–39, July 2012.
- [47] PM Embree and WD O’Brien. The accurate ultrasonic measurement of the volume flow of blood by time domain correlation. In *IEEE Ultrasonics Symposium*, pages 963–966, 1985.
- [48] PM Embree and WD O’Brien. Volumetric blood flow via time-domain correlation: experimental verification. *IEEE Trans Ultras Ferroelec Freq Control*, 37:176–189, 1990.
- [49] Ramon Q Erkamp, Stanislav Y Emelianov, Andrei R Skovoroda, and Matthew O’Donnell. Nonlinear elasticity imaging: theory and phantom study. *IEEE Trans Ultras Ferroelec Freq Control*, 51(5):532–539, May 2004.
- [50] RQ Erkamp, AR Skovoroda, SY Emelianov, and MO Donnell. Measuring the nonlinear elastic properties of tissue-like phantoms. *IEEE Trans Ultras Ferroelec Freq Control*, 51(4):410–9, 2004.
- [51] M Fatemi and J Greenleaf. Vibro-acoustography: an imaging modality based on ultrasound-stimulated acoustic emission. *Proc. Natl. Acad. Sci.*, 96:6603–6608, 1999.
- [52] M Fatemi and J Greenleaf. Probing the dynamics of tissue at low frequencies with the radiation force of ultrasound. *Phys. Med. Biol.*, 45(6):1449–1464, 2000.
- [53] M Feldman, LS Friedman, and LJ Brandt. *Feldman: Sleisenger and Fordtran’s Gastrointestinal Liver Disease, 9th ed.* Saunders, An Imprint of Elsevier, St. Louis, MO, 2010.
- [54] G Ferraioli, C Tinelli, A Malfitano, BD Bello, and C Filice. Performance of real-time strain elastography, Transient Elastography, and Aspartate-to-Platelet Ratio Index in the assessment of fibrosis in chronic hepatitis C. *American journal of Roentgenology*, 199(1):19–25, July 2012.
- [55] F Feu, JC García-Pagán, J Bosch, A Luca, J Terés, A Escorsell, and J Rodés. Relation between portal pressure response to pharmacotherapy and risk of recurrent variceal haemorrhage in patients with cirrhosis. *Lancet*, 346(8982):1056–9, October 1995.
- [56] J Foucher, E Chanteloup, J Vergniol, L Castera, B LeBail, X Adhoute, J Bertet, P Couzigou, and V DeLedinghen. Diagnosis of cirrhosis by transient elastography (FibroScan): a prospective study. *Gut*, 55(1):403–408, 2006.

- [57] G Frey and R Chiao. 4Z1c real-time volume imaging transducer. *Whitepaper*, pages 1–6, 2008.
- [58] M Friedrich-Rust, MF Ong, S Martens, C Sarrazin, J Bojunga, S Zeuzem, and E Herrmann. Performance of transient elastography for the staging of liver fibrosis: a meta-analysis. *Gastroenterology*, 134(4):960–974, 2008.
- [59] YC Fung. *Biomechanics: Mechanical Properties of Living Tissues*. Springer, 1993.
- [60] J Gao, HT Ran, XP Ye, YY Zheng, DZ Zhang, and ZG Wang. The stiffness of the liver and spleen on ARFI Imaging pre and post TIPS placement: a preliminary observation. *Clinical Imaging*, 36(2):135–41, 2012.
- [61] L Gao, K Parker, R Lerner, and S Levinson. Imaging of the elastic properties of tissue—a review. *Ultrasound in Medicine & Biology*, 22(8):959–977, 1996.
- [62] Z Gao, K Lister, and J Desai. Constitutive modeling of liver tissue: experiment and theory. *Annals of Biomedical Engineering*, 38(2):505–516, 2010.
- [63] G Garcia-Tsao. *Cirrhosis and its Sequelae*. Saunders Elsevier, Philadelphia, PA, 2008.
- [64] G Garcia-Tsao, AJ Sanyal, ND Grace, and W Carey. Prevention and management of gastroesophageal varices and variceal hemorrhage in cirrhosis. *Hepatology*, 46(3):922–38, September 2007.
- [65] BJ Geiman, LN Bohs, ME Anderson, and SM Breit. A novel interpolation strategy for estimating subsample speckle motion. *Phys Med Biol*, 1541(45):1541–1552, 2000.
- [66] JL Gennisson, T Deffieux, E Mace, G Montaldo, M Fink, and M Tanter. Viscoelastic and anisotropic mechanical properties of in vivo muscle tissue assessed by supersonic shear imaging. *Ultrasound in Medicine & Biology*, 36(5):789–801, 2010.
- [67] JL Gennisson, M Rénier, S Catheline, C Barrière, J Bercoff, M Tanter, M Fink, M Renier, and C Barriere. Acoustoelasticity in soft solids: assessment of the nonlinear shear modulus with the acoustic radiation force. *The Journal of the Acoustical Society of America*, 122(6):3219, December 2007.
- [68] James F Greenleaf, Mostafa Fatemi, and Michael Insana. Selected methods for imaging elastic properties of biological tissues. *Annual review of biomedical engineering*, 5:57–78, January 2003.

- [69] R Groszmann, JD Vorobioff, and H Gao. Measurement of portal pressure: when, how, and why to do it. *Clinics in Liver Disease*, 10(3):499–512, viii, August 2006.
- [70] RJ Groszmann, G Garcia-Tsao, J Bosch, ND Grace, AK Burroughs, R Planas, A Escorsell, JC García-Pagán, D Patch, DS Matloff, H Gao, and R Makuch. Beta-blockers to prevent gastroesophageal varices in patients with cirrhosis. *The New England Journal of Medicine*, 353(21):2254–61, November 2005.
- [71] GM Gulzar, SA Zargar, S Jalal, MS Alaie, G Javid, PK Suri, NA Shah, MS Ha-keem, A Shoukat, and GA Dar. Correlation of hepatic venous pressure gradient with variceal bleeding, size of esophageal varices, etiology, acites and degree of liver dysfunction in cirrhosis of liver. *Indian Journal of Gastroenterology*, 28(2):61, 2009.
- [72] Timothy J Hall, Paul E Barbone, Assad A Oberai, Jingfeng Jiang, Jean F. Dord, Sevan Goenezen, and Ted G Fisher. Recent results in nonlinear strain and modulus imaging. *Current Medical Imaging Reviews*, 7(4):313–327, 2012.
- [73] TJ Hall, M Bilgen, MF Insana, and TA Krouskop. Phantom materials for elastography. *IEEE Trans Ultras Ferroelec Freq Control*, 44(6):1355–1365, 1997.
- [74] JY Han, JH Cho, HJ Kwon, and KJ Nam. Predicting portal hypertension as assessed by acoustic radiation force impulse: correlations with the Doppler ultrasound. *The British Journal of Radiology*, 85(1016):e404–9, August 2012.
- [75] IA Hein and WR O’Brien. Current time-domain methods for assessing tissue motion by analysis from reflected ultrasound echoes—a review. *IEEE Trans Ultras Ferroelec Freq Control*, 40(2):84–102, January 1993.
- [76] G A Holzapfel. *Nonlinear Solid Mechanics: a continuum approach for engineering*. John Wiley & Sons, LTD, 2000.
- [77] TJR Hughes. *The Finite Element Method: Linear Static and Dynamic Finite Element Analysis*. Dover Publications, Mineola, New York, 2000.
- [78] L Huwart, F Peeters, R Sinkus, L Annet, N Salameh, LC ter Beek, Y Horsmans, and BE van Beers. Liver fibrosis: non-invasive assessment with MR elastography. *NMR Biomed*, 19(2):173–179, 2006.
- [79] T Imperiale. Measuring the hemodynamic response to primary pharmacoprophylaxis of variceal bleeding: a cost-effectiveness analysis. *The American Journal of Gastroenterology*, 98(12):2742–2750, December 2003.

- [80] T Iwao, A Toyonaga, H Shigemori, K Oho, M Sumino, M Sato, and K Tanikawa. Echo-Doppler measurements of portal vein and superior mesenteric artery blood flow in humans: inter- and intra-observer short-term reproducibility. *Journal of Gastroenterology and Hepatology*, 11(1):40–46, 1996.
- [81] P Jordan, S Socrate, T E Zickler, and R D Howe. Constitutive modeling of porcine liver in indentation using 3D ultrasound imaging. *Journal of the Mechanical Behavior of Biomedical Materials*, 2:192–201, 2009.
- [82] P Jordan, S Socrate, TE Zickler, and RD Howe. Constitutive modeling of porcine liver in indentation using 3D ultrasound imaging. *Journal of the Mechanical Behavior of Biomedical Materials*, 2(2):192–201, 2009.
- [83] F Kallel, M Bertrand, and J Ophir. Fundamental limitations on the contrast-transfer efficiency in elastography: an analytic study. *Ultrasound in Medicine & Biology*, 22(4):470, 1996.
- [84] F Kallel and J Ophir. A least-squares strain estimator for elastography. *Ultrasonic Imaging*, 19(3):195–208, July 1997.
- [85] C Kasai, N Koroku, A Koyano, and R Omoto. Real-time two-dimensional blood flow imaging using an autocorrelation technique. *IEEE Trans Ultras Ferroelec Freq Control*, SU-32(3):463, 1985.
- [86] AE Kerdok, MP Ottensmeyer, and RD Howe. Effects of perfusion on the viscoelastic characteristics of liver. *Journal of Biomechanics*, 39(12):2221–2231, 2006.
- [87] JE Kim, JY Lee, YJ Kim, JH Yoon, SH Kim, JM Lee, JK Han, and BI Choi. Acoustic Radiation Force Impulse Elastography for chronic liver disease: comparison with ultrasound-based scores of experienced radiologists, child-pugh scores, and liver function tests. *Ultrasound in Medicine & Biology*, 36(10):1643, 2010.
- [88] WR Kim and PS Kamath. Hepatic vein pressure gradient greater than 10 mmHg: prognostic or reflective? *Gastroenterology*, 134(2):641, 2008.
- [89] H Kobayashi and R Vanderby. Acoustoelastic analysis of reflected waves in nearly incompressible hyper-elastic materials: forward and inverse problems. *The Journal of the Acoustical Society of America*, 121(2):879–887, 2006.
- [90] E Konofagou, WN Lee, Ji Luo, J Provost, and J Vappou. *Physiologic cardiovascular strain and intrinsic wave imaging.*, volume 13. August 2011.
- [91] S Korukonda and MM Doyley. Estimating axial and lateral strain using a synthetic aperture elastographic imaging system. *Ultrasound in Medicine & Biology*, 37(11):1893–908, November 2011.

- [92] TA Krouskop, TM Wheeler, F Kallel, BS Garra, and T Hall. Elastic moduli of breast and prostate tissues under compression. *Ultrasonic Imaging*, 20:260–274, 1998.
- [93] J Kuo and OT von Ramm. Three-dimensional motion measurements using feature tracking. *IEEE Trans Ultras Ferroelec Freq Control*, 55(4):800–10, April 2008.
- [94] WM Lai, D Rubin, and E Kremple. *Introduction to Continuum Mechanics*. Butterworth-Heinmann, Woburn, MA, 1999.
- [95] GE Leclerc, F Charleux, C Rhein, JP Latrive, MC Ho Ba Tho, and SF Bensamoun. Viscoelastic Properties of Healthy and Fibrotic Liver With Magnetic Resonance Elastography (Mre). *Journal of Biomechanics*, 45(1):S577, July 2012.
- [96] WN Lee, CM Ingrassia, SD Fung-Kee-Fung, KD Costa, JW Holmes, and EE Konofagou. Theoretical quality assessment of myocardial elastography with in vivo validation. *IEEE Trans Ultras Ferroelec Freq Control*, 54(11):2233–2245, November 2007.
- [97] M Lemoine, S Katsahian, M Ziol, P Nahon, N Ganne-Carrie, F Kazemi, V Grando-Lemaire, JC Trinchet, and M Beaugrand. Liver stiffness measurement as a predictive tool of clinically significant portal hypertension in patients with compensated hepatitis C virus or alcohol-related cirrhosis. *Alimentary Pharmacology & Therapeutics*, 28(9):1102–10, November 2008.
- [98] C Levy, CO Zein, J Gomez, C Soldevilla-Pico, R Firpi, G Morelli, and D Nelson. Prevalence and predictors of esophageal varices in patients with primary biliary cirrhosis. *Clinical Gastroenterology and Hepatology*, 5(7):808, 2007.
- [99] RGP Lopata, MM Nillesen, HHG Hansen, IH Gerrits, JM Thijssen, and CL de Korte. Performance of two dimensional displacement and strain estimation techniques using a phased array transducer. *Ultrasound in Medicine & Biology*, 35(12):2031–41, December 2009.
- [100] T Loupas, R Peterson, and R Gill. Experimental evaluation of velocity and power estimation for ultrasound blood flow imaging, by means of a two-dimensional autocorrelation approach. *IEEE Trans Ultras Ferroelec Freq Control*, 42:689–699, 1995.
- [101] MA Lubinski, SY Emelianov, KR Raghavan, AE Yagle, AR Skovoroda, and MO Donnell. Lateral displacement estimation using tissue incompressibility. *IEEE Trans Ultras Ferroelec Freq Control*, 43(2), 1996.

- [102] Jianwen Luo, Wei-ning Lee, and Elisa Konofagou. Fundamental Performance Assessment of 2-D Myocardial Elastography in a Phased Array Configuration. pages 954–957, 2008.
- [103] S Marchesseau, T Heimann, S Chatelin, R Willinger, and H Delingette. Fast porous visco-hyperelastic soft tissue model for surgery simulation: Application to liver surgery. *Progress in Biophysics and Molecular Biology*, 103(2-3):185–196, 2010.
- [104] PA McCormick, D Patch, L Greenslade, J Chin, N McIntyre, and AK Burroughs. Clinical vs haemodynamic response to drugs in portal hypertension. *Journal of Hepatology*, 28(6):1015–9, June 1998.
- [105] J McLaughlin and D Renzi. Shear wave speed recovery in transient elastography and supersonic imaging using propagating fronts. *Inverse Problems*, 22:706, 2006.
- [106] C Merkel and S Montagnese. Hepatic venous pressure gradient measurement in clinical hepatology. *Digestive and Liver Disease*, In Press, 2011.
- [107] G Millonig, S Friedrich, S Adolf, H Fonouni, M Golriz, A Mehrabi, P Stiefel, G Pöschl, MW Büchler, HK Seitz, S Mueller, G Poschl, and M Buchler. Liver stiffness is directly influenced by central venous pressure. *Ultrasound in Medicine & Biology*, 52(2):206–210, 2010.
- [108] E Moitinho, A Escorsell, JC Bandi, JM Salmerón, JC García-Pagán, J Rodés, and J Bosch. Prognostic value of early measurements of portal pressure in acute variceal bleeding. *Gastroenterology*, 117(3):626–31, September 1999.
- [109] M Mooney. A theory of large elastic deformation. *Journal of Applied Physics*, 11:582–592, 1940.
- [110] M Muller, JL Gennisson, T Deffieux, M Tanter, and M Fink. Quantitative viscoelasticity mapping of human liver using Supersonic Shear Imaging: preliminary in vivo feasibility study. *Ultrasound in Medicine & Biology*, 35(2):229, 2008.
- [111] A Nava, E Mazza, M Furrer, P Villiger, and WH Reinhart. In vivo mechanical characterization of human liver. *Medical Image Analysis*, 12(2):203–216, 2008.
- [112] GI Nedredal, M Yin, T McKenzie, J Lillegard, J Luebke-Wheeler, J Talwalkar, R Ehman, and SL Nyberg. Portal hypertension correlates with splenic stiffness as measured with MR elastography. *Journal of Magnetic Resonance Imaging*, 34(1):79–87, July 2011.
- [113] A Nicoll. Surgical risk in patients with cirrhosis. *Journal of Gastroenterology and Hepatology*, 27(10):1569–75, October 2012.

- [114] S Nicolle, P Vezin, and J F Palierne. A strain-hardening bi-power law for the nonlinear behaviour of biological soft tissues. *Journal of Biomechanics*, 43(5):927–932, 2010.
- [115] K R Nightingale, M S Soo, R W Nightingale, R Bentley, D L Stutz, M L Palmeri, J D Dahl, and G E Trahey. Acoustic Radiation Force Impulse Imaging: Remote Palpation of the Mechanical Properties of Tissue. In *Proceedings of the 2002 IEEE Ultrasonics Symposium*, 2002.
- [116] KR Nightingale, SA McAleavey, and GE Trahey. Shear wave generation using acoustic radiation force: in vivo and ex vivo results. *Ultrasound in Medicine & Biology*, 29(12):1723, 2003.
- [117] KR Nightingale, RW Nightingale, ML Palmeri, and GE Trahey. Finite element analysis of radiation force induced tissue motion with experimental validation. In *Proceedings of the 2000 IEEE Ultrasonics Symposium*, volume 22, page 1323, 2000.
- [118] KR Nightingale, ML Palmeri, RR Bouchard, and GE Trahey. Acoustic radiation force impulse imaging: a parametric analysis of factors affecting image quality. In *Proceedings of the 2003 IEEE Ultrasonics Symposium*, 2003.
- [119] KR Nightingale, ML Palmeri, RW Nightingale, and GE Trahey. On the feasibility of remote palpation using acoustic radiation force. *The Journal of the Acoustical Society of America*, 110(1):625–634, 2001.
- [120] KR Nightingale, ML Palmeri, and GE Trahey. Analysis of contrast in images generated with transient acoustic radiation force. *Ultrasound in Medicine & Biology*, 32(1):61–72, 2006.
- [121] WLM Nyborg, T Litovitz, and C Davis. Acoustic Streaming. In W P Mason, editor, *Physical Acoustics*, volume IIA, chapter 11, pages 265–331. Academic Press Inc, New York, 1965.
- [122] R W Ogden. *Non-Linear Elastic Deformations*. Halsted Press, Dover, 1984.
- [123] J. Ophir, S. K. Alam, B. Garra, F. Kallel, E. Konofagou, T. Krouskop, and T. Varghese. Elastography: ultrasonic estimation and imaging of the elastic properties of tissues. *Proceedings of the Institution of Mechanical Engineers, Part H: Journal of Engineering in Medicine*, 213(3):203–233, March 1999.
- [124] J Ophir, I Céspedes, H Ponnekanti, Y Yazdi, and X Li. Elastography: a quantitative method for imaging the elasticity of biological tissues. *Ultrasonic Imaging*, 13:111–134, 1991.

- [125] M L Palmeri, S A McAleavey, G E Trahey, and K R Nightingale. Ultrasonic tracking of acoustic radiation force-induced displacements in homogeneous media. *IEEE Trans Ultras Ferroelec Freq Control*, 53(7):1313, 2006.
- [126] M L Palmeri, M H Wang, N C Rouze, M Abdelmalek, C Guy, B Moser, A M Diehl, and Nightingale K.R. Noninvasive Evaluation of Hepatic Fibrosis using Acoustic Radiation Force-Based Shear Stiffness in Patients with Nonalcoholic Fatty Liver Disease. *Journal of Hepatology*, 55(3):666–672, 2011.
- [127] Mark L Palmeri, Jeremy J Dahl, David B MacLeod, Stuart A Grant, and Kathryn R Nightingale. On the feasibility of imaging peripheral nerves using acoustic radiation force impulse imaging. *Ultrason Imaging*, 31(3):172–182, July 2009.
- [128] Mark L Palmeri, Michael H Wang, Ned C Rouze, Manal F Abdelmalek, Cynthia D Guy, Barry Moser, Anna Mae Diehl, and Kathryn R Nightingale. Non-invasive evaluation of hepatic fibrosis using acoustic radiation force-based shear stiffness in patients with nonalcoholic fatty liver disease. *Journal of hepatology*, 55(3):666–72, September 2011.
- [129] ML Palmeri, SA McAleavey, KL Fong, GE Trahey, and KR Nightingale. Dynamic mechanical response of elastic spherical inclusions to impulsive acoustic radiation force excitation. *IEEE Trans Ultras Ferroelec Freq Control*, 53(11):2065–2079, 2006.
- [130] ML Palmeri, SA McAleavey, GE Trahey, and KR Nightingale. Ultrasonic tracking of acoustic radiation force-induced displacements in homogeneous media. *IEEE Trans Ultras Ferroelec Freq Control*, 53(7):1313, 2006.
- [131] ML Palmeri, AC Sharma, RR Bouchard, RW Nightingale, and KR Nightingale. A finite element model of soft tissue response to impulsive acoustic radiation force. *IEEE Trans Ultras Ferroelec Freq Control*, 52(10):1712, 2005.
- [132] ML Palmeri, MH Wang, JJ Dahl, KD Frinkley, and KR Nightingale. Quantifying hepatic shear modulus in vivo using acoustic radiation force. *Ultrasound in Medicine & Biology*, 34(4):546–558, 2008.
- [133] KJ Parker. Ultrasonic attenuation and absorption in liver tissue. *Ultrasound in Medicine & Biology*, 9(4):363–369, 1983.
- [134] N Patel. Portal hypertension. *Seminars in Roentgenology*, 37(4):293–302, 2002.
- [135] Y Petrank, L Huang, and M O’Donnell. Reduced peak-hopping artifacts in ultrasonic strain estimation using the Viterbi algorithm. *IEEE Trans Ultras Ferroelec Freq Control*, 56(7):1359–1367, July 2009.

- [136] GF Pinton, JJ Dahl, and GE Trahey. Rapid tracking of small displacements with ultrasound. *IEEE Trans Ultras Ferroelec Freq Control*, 53(6):1103–1117, June 2006.
- [137] GF Pinton, SA McAleavey, JJ Dahl, KR Nightingale, and GE Trahey. Real-time acoustic radiation force impulse imaging. *Proceedings of the 2005 SPIE Conference on Medical Imaging*, 2005.
- [138] Gianmarco F Pinton, Jeremy J Dahl, and Gregg E Trahey. Rapid tracking of small displacements with ultrasound. *IEEE Trans. Ultrason., Ferroelec., Freq. Contr.*, 53(6):1103–1117, June 2006.
- [139] Gianmarco F Pinton and Gregg E Trahey. Continuous delay estimation with polynomial splines. *IEEE Trans Ultrason Ferroelectr Freq Control*, 53(11):2026–2035, November 2006.
- [140] B Ramamurthy. Potential and limitations of angle-independent flow detection algorithms using radio-frequency and detected echo signals. *Ultrasonic Imaging*, 13(3):252–268, July 1991.
- [141] T Reiberger, A Ferlitsch, BA Payer, M Pinter, P Schwabl, J Stift, M Trauner, and M Peck-Radosavljevic. Noninvasive screening for liver fibrosis and portal hypertension by transient elastography—a large single center experience. *The Central European Journal of Medicine*, 124(11-12):395–402, June 2012.
- [142] TB Reynolds, AG Redeker, and HM Geller. Wedged hepatic venous pressure: a clinical evaluation. *The American Journal of Medicine*, page 350, 1957.
- [143] K Rifai, J Cornberg, I Mederacke, M Bahr, H Wedemeyer, P Malinski, H Bantel, B Boozari, A Potthoff, M P Manns, and M Gebel. Clinical feasibility of liver elastography by acoustic radiation force impulse imaging (ARFI). *Digestive and Liver Disease*, 2011.
- [144] R Righetti, J Ophir, and P Ktonas. Axial Resolution in Elastography. *Ultrasound in Medicine & Biology*, 28(1):101–113, 2002.
- [145] R Righetti, S Srinivasan, and J Ophir. Lateral resolution in elastography. *Ultrasound in Medicine & Biology*, 29(5):695–704, May 2003.
- [146] C Ripoll, R Groszmann, G Garcia-Tsao, N Grace, A Burroughs, R Planas, A Escorsell, JC García-Pagán, R Makuch, D Patch, DS Matloff, and J Bosch. Hepatic venous pressure gradient predicts clinical decompensation in patients with compensated cirrhosis. *Gastroenterology*, 133(2):481–8, August 2007.
- [147] RS Rivlin and DW Saunders. Large elastic deformations of isotropic materials, VII: experiments on the deformation of rubber. *Philos Trans Soc London*, 243:251–288, 1951.

- [148] M A Robic, B Procopet, S Métivier, J M Péron, J Selves, J P Vinel, and C Bureau. Liver Stiffness Accurately Predicts Portal Hypertension Related Complications in Patients with Chronic Liver Disease: a prospective study. *Journal of Hepatology*, Article in, 2011.
- [149] MA Robic, B Procopet, S Metivier, JM Peron, J Selves, JP Vinel, and C Bureau. Liver Stiffness Accurately Predicts Portal Hypertension Related Complications in Patients with Chronic Liver Disease: a prospective study. *Journal of Hepatology*, 55:1017–1024, 2011.
- [150] D Rockey. The Cellular Pathogenesis of Portal Hypertension: Stellate Cell Contractility, Endothelin, and Nitric Oxide. *Hepatology*, 25(1):2–5, 1997.
- [151] V Rotemberg, M Palmeri, R Nightingale, N Rouze, and K Nightingale. The impact of hepatic pressurization on liver shear wave speed estimates in constrained versus unconstrained conditions. *Phys Med Biol*, 57(2):329–41, January 2012.
- [152] V Rotemberg, M Palmeri, S Rosenzweig, S Grant, and K Nightingale. Improved needle visualization using acoustic radiation force-based image mapping algorithms. In *American Society of Anesthesia*, New Orleans, LA, 2009.
- [153] D Roulot, S Czernichow, HL Clesiau, JL Costes, AC Vergnaud, and M Beaugrand. Liver stiffness values in apparently healthy subjects: Influence of gender and metabolic syndrome. *Journal of Hepatology*, 48:613, 2008.
- [154] C Sabba, G.G. Weltin, D.V. Ciocchetti, G. Ferraioli, K.J. Taylor, T. Nakamura, F. Moriyasu, and Roberto J Groszmann. Observer variability in echo-Doppler measurements of portal flow in cirrhotic patients and normal volunteers. *Gastroenterology*, 98(6):1603–1611, 1990.
- [155] M Sánchez-Conde, P Miralles, J María Bellón, D Rincón, M Ramírez, I Gutiérrez, C Ripoll, J C López, J Cosín, G Clemente, O Lo Iacono, R Bañares, and J Berenguer. Use of transient elastography (FibroScan) for the noninvasive assessment of portal hypertension in HIV/HCV-coinfected patients. *Journal of Viral Hepatitis*, 18(10):685–91, October 2011.
- [156] L Sandrin, M Tanter, S Catheline, and M Fink. Shear modulus imaging with 2-D transient elastography. *IEEE Trans Ultras Ferroelec Freq Control*, 49(4):426–435, April 2002.
- [157] L Sandrin, M Tanter, JL Gennisson, S Catheline, and M Fink. Shear elasticity probe for soft tissues with 1-D transient elastography. *IEEE Trans Ultras Ferroelec Freq Control*, 49(4):436–446, April 2002.
- [158] Laurent Sandrin, Bertrand Fourquet, Jean-Michel Hasquenoph, Sylvain Yon, Céline Fournier, Frédéric Mal, Christos Christidis, Marianne Ziol, Bruno

- Poulet, Farad Kazemi, Michel Beaugrand, and Robert Palau. Transient elastography: a new noninvasive method for assessment of hepatic fibrosis. *Ultrasound Med. Biol.*, 29(12):1705–1713, December 2003.
- [159] A Sarvazyan. Diversity of biomedical applications of acoustic radiation force. *Ultrasonics*, 50(2):230–234, 2010.
- [160] A Sarvazyan, O Rudenko, S Swanson, J Fowlkes, and S Emelianov. Shear wave elasticity imaging: a new ultrasonic technology of medical diagnostics. *Ultrasound in Medicine & Biology*, 24(9):1435, 1998.
- [161] B Schlosser, M Biermer, B Fulop, E Schott, P Asbach, I Sack, and T Berg. Evaluation of Magnetic Resonance Elastography (MRE) as a non-invasive method to assess the stage of liver fibrosis in patients with chronic liver diseases. *Hepatology*, 50(4):919, 2009.
- [162] JM Schwartz, M Denninger, D Rancourt, C Moisan, and D Laurendeau. Modelling liver tissue properties using a non-linear visco-elastic model for surgery simulation. *Medical image Analysis*, 9(2):103–12, April 2005.
- [163] M Shams, M Destrade, and RW Ogden. Initial stresses in elastic solids: constitutive laws and acoustoelasticity. *Wave Motion*, 48(7):552–567, 2011.
- [164] AI Sharara and DC Rockey. Gastroesophageal variceal hemorrhage. *New England Journal of Medicine*, 345(9):669–681, 2001.
- [165] R Sinkus, J Lorenzen, D Schrader, M Lorenzen, M Dargatz, and D Holz. High-resolution tensor MR elastography for breast tumour detection. *Phys. Med. Bio.*, 45(6):1649–1664, June 2000.
- [166] AR Skovoroda, MA Lubinski, SY Emelianov, and M O’Donnell. Nonlinear estimation of the lateral displacement using tissue incompressibility. *IEEE Trans Ultras Ferroelec Freq Control*, 45(2):491–503, January 1998.
- [167] S. Srinivasan, R. Righetti, and J. Ophir. Trade-offs between the axial resolution and the signal-to-noise ratio in elastography. *Ultrasound in Medicine & Biology*, 29(6):847–866, June 2003.
- [168] J Stebbing, L Farouk, G Panos, M Anderson, L R Jiao, S Mandalia, M Bower, B Gazzard, and M Nelson. A meta-analysis of Transient Elastography for the detection of hepatic fibrosis. *Journal of Clinical Gastroenterology*, 44(3):214–219, 2010.
- [169] H Stefanescu, M Grigorescu, M Lupsor, B Procopet, A Maniu, and R Badea. Spleen stiffness measurement using Fibroscan for the noninvasive assessment of esophageal varices in liver cirrhosis patients. *Journal of Gastroenterology and Hepatology*, 26(1):164–70, January 2011.

- [170] Y Takuma, K Nouse, Y Morimoto, J Tomokuni, A Sahara, N Toshikuni, Hi Takabatake, H Shimomura, A Doi, I Sakakibara, K Matsueda, and H Yamamoto. Measurement of spleen stiffness by acoustic radiation force impulse imaging identifies cirrhotic patients with esophageal varices. *Gastroenterology*, in press, September 2012.
- [171] JA Talwalkar, M Yin, S Venkatesh, PJ Rossman, RC Grimm, A Manduca, A Romano, PS Kamath, and RL Ehman. Feasibility of in vivo MR elastographic splenic stiffness measurements in the assessment of portal hypertension. *American Journal of Roentgenology*, 193(1):122–127, 2009.
- [172] H Tchelepi, P Ralls, R Radin, and E Grant. Sonography of Diffuse Liver Disease. *J Ultrasound Med*, 21:1023–1032, 2002.
- [173] U Thalheimer, L Bellis, C Puoti, and AK Burroughs. Should we routinely measure portal pressure in patients with cirrhosis, using hepatic venous pressure gradient (HVPG) as a guide for prophylaxis and therapy of bleeding and rebleeding? No. *European Journal of Internal Medicine*, 22(1):5–7, February 2011.
- [174] U Thalheimer, G Leandro, DN Samonakis, CK Triantos, D Patch, and AK Burroughs. Assessment of the agreement between wedge hepatic vein pressure and portal vein pressure in cirrhotic patients. *Digestive and Liver Disease*, 37(8):601–8, August 2005.
- [175] Arun Thitaikumar, Raffaella Righetti, Thomas A Krouskop, and Jonathan Ophir. Resolution of axial shear strain elastography. *Phys Med Biol*, 51(20):5245–5257, October 2006.
- [176] CK Triantos and AK Burroughs. Prevention of the development of varices and first portal hypertensive bleeding episode. *Best Practice & Research Clinical Gastroenterology*, 21(1):31–42, January 2007.
- [177] S Umale, C Deck, N Bourdet, P Dhumane, L Soler, J Marescaux, and R Willinger. Experimental mechanical characterization of abdominal organs: liver, kidney & spleen. *Journal of the Mechanical Behavior of Biomedical Materials*, August 2012.
- [178] R Vanderby and H Kobayashi. Non-invasive strain measurements of ligaments and tendons via acoustoelastic analysis of ultrasonic waves. *Journal of Biomechanics*, 39:S64–65, 2006.
- [179] T Varghese, E E Konofagou, J Ophir, S K Alam, and M Bilgen. Direct strain estimation in elastography using spectral cross-correlation. *Ultrasound Med Biol*, 26(9):1525–1537, November 2000.

- [180] T Varghese and J Ophir. A theoretical framework for performance characterization of elastography: the strain filter. *IEEE Trans Ultras Ferroelec Freq Control*, 44(1):164–72, January 1997.
- [181] C Villanueva, J Minana, J Ortiz, A Gallego, G Soriano, X Torras, S Sainz, J Boadas, X Cusso, C Guarner, and J Balanzo. Endoscopic ligation compared with combined treatment with nadolol and isosorbide mononitrate to prevent recurrent variceal bleeding. *New England Journal of Medicine*, 345(9):647–655, 2001.
- [182] F Viola and W F Walker. Radiation force imaging of viscoelastic properties with reduced artifacts. *IEEE Trans. Ultrason.,Ferroelec.,Freq. Contr.*, 50(6):736–742, June 2003.
- [183] F Viola and WF Walker. A comparison of the performance of time-delay estimators in medical ultrasound. *IEEE Trans Ultras Ferroelec Freq Control*, 50(4):401, 2003.
- [184] F Vizzutti, U Arena, L Rega, and M Pinzani. Non invasive diagnosis of portal hypertension in cirrhotic patients. *Gastroentérologie Clinique et Biologique*, 32(6 Suppl 1):80–7, September 2008.
- [185] F Vizzutti, U Arena, L Rega, and M Pinzani. Non invasive diagnosis of portal hypertension in cirrhotic patients. *Gastroenterol Clin Bio*, 32:87, 2008.
- [186] F Vizzutti, U Arena, RG Romanelli, L Rega, M Foschi, S Colagrande, A Petrarca, S Moscarella, G Belli, AL Zignego, F Marra, G Laffi, and M Pinzani. Liver stiffness measurement predicts severe portal hypertension in patients with HCV-related cirrhosis. *Hepatology*, 45(5):1290–7, May 2007.
- [187] J Vorobioff, R Groszmann, E Picabea, M Gamen, R Villavicencio, J Bordato, I Morel, M Audano, H Tanno, E Lerner, and M Passamonti. Prognostic value of hepatic venous pressure gradient measurements in alcoholic cirrhosis: a 10-Year prospective study. *Gastroenterology*, 111:709, 1996.
- [188] JD Vorobioff. Hepatic venous pressure in practice - how, when, and why. *Journal of Clinical Gastroenterology*, 41(10):S336–S343, 2007.
- [189] RF Wagner, SW Smith, JM Sandrik, and H Lopez. Statistics of speckle in ultrasound B-scans. *IEEE Transactions on Sonics and Ultrasonics*, 30(3):156–163, May 1983.
- [190] W Walker and G Trahey. A Fundamental Limit on Delay Estimation Using Partially Correlated Speckle Signals. *IEEE Trans. Ultrason.,Ferroelec.,Freq. Contr.*, 42(2):301–308, 1995.

- [191] WF Walker, FJ Fernandez, and LA Negron. A method of imaging viscoelastic parameters with acoustic radiation force. *Phys. Med. Bio.*, 45(6):1447, 2000.
- [192] MH Wang, ML Palmeri, VM Rotemberg, NC Rouze, and KR Nightingale. Improving the robustness of time-of-flight based shear wave speed reconstruction methods using RANSAC in human liver in vivo. *Ultrasound in Medicine & Biology*, 36(5):802–813, 2010.
- [193] Shougang Wang, Wei-Ning Lee, Jean Provost, Jianwen Luo, and Elisa E Konofagou. A composite high-frame-rate system for clinical cardiovascular imaging. *IEEE Trans Ultrason Ferroelectr Freq Control*, 55(10):2221–2233, October 2008.
- [194] KA Wear and RL Popp. Theoretical analysis of a technique for the characterization of myocardium contraction based upon temporal correlation of ultrasonic echoes. *IEEE Trans Ultrason Ferroelec Freq Control*, 34(3):368–75, January 1987.
- [195] PeterNT Wells and HD Liang. Medical ultrasound: imaging of soft tissue strain and elasticity. *Journal of the Royal Society*, 8(64):1521–49, November 2011.
- [196] B Winkfield, C Aubé, P Burtin, and P Calès. Inter-observer and intra-observer variability in hepatology. *European Journal of Gastroenterology & Hepatology*, 15(9):959–66, September 2003.
- [197] CC Wu. Ultrasonographic evaluation of portal hypertension and liver cirrhosis. *Journal of Medical Ultrasound*, 16(3):188–193, January 2008.
- [198] SS Yang. Duplex Doppler ultrasonography in portal hypertension. *Journal of Medical Ultrasound*, 15(2):103–111, 2007.
- [199] M Yoneda, H Mawatari, K Fujita, H Endo, H Lida, Y Nozaki, K Yonemitsu, T Higurashi, H Takahashi, N Kobayashi, H Kirikoshi, Y Abe, M Inamori, K Kubota, S Saito, M Tamano, H Hiraishi, S Maeyama, N Yamaguchi, S Togo, and A Nakajima. Noninvasive assessment of liver fibrosis by measurement of stiffness in patients with nonalcoholic fatty liver disease (NAFLD). *Digestive and Liver Disease*, 40(5):378, 2008.
- [200] EA Zabolotskaya, YA Ilinskii, and MF Hamilton. Nonlinear surface waves in soft, weakly compressible elastic media. *The Journal of the Acoustical Society of America*, 121(4):1873–1878, 2007.
- [201] L Zhai, J Madden, WC Foo, V Mouraviev, TJ Polascik, ML Palmeri, and KR Nightingale. Characterizing stiffness of human prostates using acoustic radiation force. *Ultrasonic Imaging*, 32(4):201–213, October 2010.

- [202] J Zhang and MB Fallon. Hepatopulmonary syndrome: update on pathogenesis and clinical features. *Nature Reviews. Gastroenterology & Hepatology*, 9(9):539–49, September 2012.
- [203] G Zironi, S Gaiani, A Rigamonti, L Bolondi, and L Barbara. Value of measurement of mean portal flow velocity by Doppler flowmetry in the diagnosis of portal hypertension. *Journal of Hepatology*, 16:298–303, 1992.

Biography

Name Veronica Rotemberg

Date and Place of Birth October 29, 1984 Boston, MA

Degrees Earned B.A. Chemistry and Physics, Harvard University

Awards and Fellowships

1. Gertrude B. Elion Mentored Medical Student Award (2010)
2. NIH Grant F30 DK095544

Publications

1. Donald JE, Hubner IA, Rotemberg VM, Shakhnovich EI, Mirny LA. CoC: a database of universally conserved residues in protein folds, *Bioinformatics* 21(10): 2539-2540 (2005)
2. Wang MH, Palmeri ML, Rotemberg VM, Rouze NC, Nightingale KR. Improving the robustness of time-of-flight based shear wave speed reconstruction methods using RANSAC in human liver in vivo, *Ultrasound Med. Biol.*, 36(5): 802-13 (2010)
3. Rotemberg VM, Palmeri ML, et al. Acoustic Radiation Force Impulse (ARFI) Imaging-Based Needle Visualization, *Ultrasonic Imaging*, 33 (2010)
4. Bing KF, Rouze, NC, Palmeri M, Rotemberg VM, Nightingale KR. Combined ultrasonic thermal ablation with interleaved ARFI image monitoring using a single diagnostic curvilinear array: a feasibility study, *Ultrasonic Imaging*, 33(4) (2011)
5. Rotemberg V, Palmeri M, Nightingale R, Rouze N, Nightingale, K. The impact of hepatic pressurization on Liver shear wave speed estimates in constrained vs. unconstrained conditions, *Physics in Medicine and Biology*, 57(2) (2012)
6. Rotemberg V, Byram, B, Palmeri M, Wang, M, Nightingale, K. Ultrasonic characterization of the nonlinear properties of canine livers by measuring shear wave speed and axial strain with increasing portal venous pressure, *Journal of Biomechanics*, in review